UC San Diego

UC San Diego Electronic Theses and Dissertations

Title

Variability in formation, properties, and transport of North Atlantic Deep Water

Permalink

https://escholarship.org/uc/item/30h7h4bk

Author

Koelling, Jannes

Publication Date

2020

Peer reviewed|Thesis/dissertation

eScholarship.org Powered by the California Digital Library
University of California

UNIVERSITY OF CALIFORNIA SAN DIEGO

Variability in formation, properties, and transport of North Atlantic Deep Water

A dissertation submitted in partial satisfaction of the
requirements for the degree
Doctor of Philosophy

in

Oceanography

by

Jannes Koelling

Committee in charge:

Professor Uwe Send, Chair
Professor Graham Elliott
Professor Sarah Gille
Professor Todd Martz
Professor Lynne Talley

2020

Copyright
Jannes Koelling, 2020
All rights reserved.

The dissertation of Jannes Koelling is approved, and it is acceptable in quality and form for publication on microfilm and electronically:

_____

_____

_____

_____

_____

Chair

University of California San Diego

2020

TABLE OF CONTENTS

Signature Page . . . iii

Table of Contents . . . iv

List of Figures . . . vi

List of Tables . . . viii

List of Common Abbreviations . . . ix

Acknowledgements . . . x

Vita . . . xii

Abstract of the Dissertation . . . xiii

Introduction . . . 1

Chapter 1 Intense oceanic uptake of oxygen during 2014–2015 winter convection in the Labrador Sea . . . 7
- 1.1 Introduction . . . 8
- 1.2 Data and Methods . . . 9
  - 1.2.1 Data . . . 9
  - 1.2.2 Oxygen budget . . . 10
  - 1.2.3 Air-Sea gas exchange parameterizations . . . 13
- 1.3 Results . . . 15
- 1.4 Discussion . . . 17
  - 1.4.1 Observed change . . . 17
  - 1.4.2 Gas exchange parameterizations . . . 19
- 1.5 Outlook . . . 21
- 1.6 Conclusion . . . 22
- 1.7 Acknowledgments . . . 23
- 1.8 Supporting information . . . 25

Chapter 2 Lateral flux of carbon, oxygen, and nitrate into the central Labrador Sea . . . 33
- 2.1 Introduction . . . 33
- 2.2 Data . . . 35
- 2.3 Methods . . . 37
  - 2.3.1 Error estimates . . . 38
  - 2.3.2 Limitations . . . 38
- 2.4 Determining the rate of lateral exchange . . . 39
- 2.5 Budgets of carbon, oxygen, and nitrate . . . 42

2.6 Summary . . . 47
2.7 Acknowledgments . . . 48

Chapter 3 Decadal strengthening of interior flow of North Atlantic Deep Water observed by GRACE satellites . . . 49
3.1 Introduction . . . 50
3.2 Methods and Data . . . 53
3.2.1 Data . . . 53
3.2.2 Sea Level Budget . . . 55
3.2.3 Geostrophic Transport . . . 57
3.2.4 Error Sources . . . 57
3.3 Ocean mass changes . . . 60
3.3.1 Validating decadal trends in GRACE . . . 60
3.3.2 Spatial pattern of the trend . . . 63
3.3.3 Deep ocean contribution to steric height . . . 64
3.4 Circulation changes . . . 66
3.4.1 GRACE as a measure of NADW transport change . . . 67
3.4.2 Changes in strength of NADW pathways . . . 69
3.4.3 Possible causes of variability . . . 72
3.4.4 Net circulation change west of the MAR . . . 76
3.5 Summary . . . 77
3.6 Acknowledgments . . . 78

Chapter 4 Multi-decadal variability of North Atlantic Deep Water transport . . . 80
4.1 Introduction . . . 80
4.2 Data and Methods . . . 83
4.2.1 Data . . . 83
4.2.2 Methods . . . 85
4.3 Variability at MOVE . . . 87
4.3.1 Transport . . . 87
4.3.2 Water mass changes . . . 90
4.3.3 Comparison to theory, models, and other observations . . . 97
4.4 MOVE and RAPID . . . 102
4.4.1 Transports referenced to GRACE . . . 105
4.4.2 RAPID compensation term . . . 108
4.4.3 Reconstructing RAPID transport using a shallow reference level 110
4.4.4 MOVE & RAPID: Discussion . . . 111
4.5 Summary . . . 115
4.6 Acknowledgments . . . 116

Summary and Outlook . . . 117

LIST OF FIGURES

Figure 0.1: Schematic of the Atlantic Meridional Overturning Circulation (AMOC). . . 2

Figure 1.1: Map of the Labrador Sea showing oxygen content and measurement locations 10
Figure 1.2: Oxygen concentrations and mixed layer depth 11
Figure 1.3: Measured oxygen uptake compared to estimates from different parameterizations with and without bubbles 16
Figure 1.4: Uncorrected oxygen concentration measured at 10m, 60m and 100m 27
Figure 1.5: Difference between corrected (see figure 1.4) mooring data and a CTD profile taken shortly before deployment at 10m, 60m and 100m. 28
Figure 1.6: Change in mixed layer heat content calculated from all 11 sensors that are within the mixed layer at each time, and calculated from near-surface temperature and z_{MLD} only, analogous to the method used for oxygen . . . 29
Figure 1.7: 10m wind speed from NARR, 6-hourly values and 5-day running mean, and 5-day running mean of CCMP winds 30
Figure 1.8: 100-1400m oxygen and heat content measured by Argo float #5904989. . . . 31
Figure 1.9: As in figure 1.3, but assuming no loss of oxygen through lateral transport or respiration, such that $F_{\mathrm{gasex}} = \Delta \int \mathrm{O}_2$ 32

Figure 2.1: Mean salinity at the surface, and location of data used for the calculations. . 36
Figure 2.2: Mean temperature and salinity for profiles taken in the boundary and interior 40
Figure 2.3: Cumulative fraction of water mixed into the interior from the boundary current. 41
Figure 2.4: Inventories of dissolved inorganic carbon (DIC), oxygen, and nitrate measured by the Seacycler mooring. 42
Figure 2.5: Cumulative lateral flux for carbon, oxygen, and nitrate from the boundary current region into the interior Labrador Sea. 44
Figure 2.6: Cumulative biological flux (Net Community Production) for carbon, oxygen, and nitrate. 45

Figure 3.1: Ocean mass change in the GRACE JPL RL05.1M product, calculated as the mean from 2010/04/01 to 2017/03/31 minus the mean from 2010/04/01 to 2017/03/31. 52
Figure 3.2: Ocean mass from GRACE compared to ocean mass calculated from altimetry and mooring and hydrography data. 62
Figure 3.3: Maximum layer thickness, or vertical distance between σ_4 isopycnals of water with with silicate below 40 μmol L^{-1}. 63
Figure 3.4: Ocean mass trend calculated using steric height data between the surface and each depth. 65
Figure 3.5: Circulation anomalies resulting from ocean mass changes, and schematic of major features of North Atlantic Deep Water (NADW) spreading in the North Atlantic. 68
Figure 3.6: Barotropic transport change from GRACE compared to baroclinic transport change from density measurements. 70

Figure 3.7: 2010-2017 minus 2002-2009 circulation and transport change from GRACE, calculated for two regions, DWBC and interior branch. 72
Figure 3.8: Annual cycle of barotropic transport in the interior branch from GRACE data. 74

Figure 4.1: Simplified schematic of NADW pathways, and position of MOVE and RAPID arrays. 81
Figure 4.2: Velocity profile along the MOVE section. 84
Figure 4.3: NADW transports anomalies from MOVE. 87
Figure 4.4: Contribution of deep density anomalies at the eastern and western boundary to MOVE transports. 91
Figure 4.5: Profile of mean σ_4 potential density at the MOVE 3 (western boundary) mooring for the 2002–2004 and 2014–2016 periods. 92
Figure 4.6: Temperature-salinity (T/S) plot for MOVE 3 data below 3000 dbar. 94
Figure 4.7: Time series of salinity and σ_4 potential density at the MOVE 3 (western boundary) mooring at 4500 dbar. 95
Figure 4.8: Profile of mean σ_4 potential density at the MOVE 1 (Mid-Atlantic Ridge) mooring for the 2000–2002 and 2014–2016 periods. 96
Figure 4.9: Temperature-salinity (T/S) plot for MOVE 1 data below 3000 dbar. 98
Figure 4.10: MOVE 3 mean T/S for the two periods, compared to climatological CTD data taken from the World Ocean Atlas. 101
Figure 4.11: NADW transports from RAPID and MOVE. 103
Figure 4.12: Salinity at 4500 dbar and T/S plot for RAPID western boundary moorings. 104
Figure 4.13: Western basin transport anomalies from 16°N and 26°N referenced to velocities from GRACE bottom pressure. 105
Figure 4.14: Vertical structure of decadal trend in transport, 2011-2015 mean minus 2004-2008 mean. 107
Figure 4.15: RAPID moorings, and reference levels implicitly used in the calculation. . 109
Figure 4.16: 2-year mean profiles of transport through the RAPID section. 111
Figure 4.17: Transports at RAPID and MOVE with shallow reference level. 112
Figure 4.18: Idealized schematic of two different explanations for how water mass changes at the western boundary affect transport. 114

LIST OF TABLES

Table 1.1: Components of the oxygen budget and gas exchange estimated from different parameterizations, integrated from November-April 15

Table 3.1: Access information for data used in this study 54
Table 3.2: Components of the sea level budget. 61

LIST OF COMMON ABBREVIATIONS

AABW	Antarctic Bottom Water
AMOC	Atlantic Meridional Overturning Circulation
BATS	Bermuda Atlantic Time Series
DWBC	Deep Western Boundary Current
CTD	Conductivity-Termperature-Depth
DIC	Dissolved Inorganic Carbon
DSOW	Denmark Strait Overflow Water
ISOW	Iceland Scotland Overflow Water
GRACE	Gravity Recovery and Climate Experiment
MAR	Mid-Atlantic Ridge
MLD	Mixed Layer Depth
MOVE	Meridional Overturning Experiment
LSW	Labrador Sea Water
NADW	North Atlantic Deep Water
NAO	North Atlantic Oscillation
NCP	Net Community Production
$\mathbf{NO_3}$	Nitrate
$\mathbf{O_2}$	Oxygen
$p\mathbf{CO_2}$	partial pressure of Carbon Dioxide
RAPID-MOCHA	RAPID-Meridional Overturning Circulation and Heatflux Array
RMSD	Root Mean Square Difference
SSH	Sea Surface Height
S	Salinity
T	Temperature

ACKNOWLEDGEMENTS

Like most dissertations, the work presented here would not have been possible without the help and support from many people, which I would like to acknowledge.

Uwe Send took me on as his student 6 years ago, and has helped me grow as a scientist through these years by allowing me to work fairly independently while also providing the impetus to keep me moving in the right direction. The members of my PhD committee, Sarah Gille, Lynne Talley, Todd Martz, and Graham Elliott, have helped with useful comments and suggestions during my annual committee meetings, and were always happy to dicuss my work with me and provide feedback. Matthias Lankhorst was a tremendous help for answering any questions I had both about the science I was doing (or trying to do), and about any minute details of the instrument setups and sensor calibration for our data. Douglas Wallace and Dariia Atamanchuk were great collaborators during the 10 months total that I spent at Dalhousie University, and managed to slowly turn me into more and more of a chemical oceanographer. I would like to thank Johannes Karstensen, Eleanor Frajka-Williams, Craig McNeil, and Felix Landerer for being co-authors and/or providing helpful comments and suggestions on some of the chapters. I appreciate the Send lab for all the work they did to collect the data I used, and for the good company on various research cruises (shoutout to The Specialists). My work has benefited from funding by the National Aeronautics and Space Administration and the Ocean Frontier Institute, and I am grateful for their support.

I would also like to thank the people that made the non-work part of my time at SIO so much more enjoyable, including the 2013 cohort, the Soft Loft, and all my other friends here. I'm particularly thankful for all the people I've played soccer with over the years, from SIO beach soccer to games at the water tower and pickup and intramurals on UCSD main campus. Finally, huge thanks to my parents for all the support they have given me, my brother Nils for always setting the bar so high that even in failing to clear it I still did pretty well, and to Caitlin for giving me the motivation and support to get over the finish line.

Chapter 1, in full, is a reprint with minor modifications of the material as it appears in Geophysical Research Letters, 2017. Koelling, J.; Wallace, D.W.R.; Send, U.; Karstensen, J. The dissertation author was the primary investigator and author of this paper.

Chapter 2, in full, is being prepared for submission for publication of the material. Koelling, J.; Atamanchuk, D.; Wallace D.W.R.; Send, U. The dissertation author was the primary investigator and author of this material.

Chapter 3, in full, has been submitted for publication of the material as it may appear in Journal of Geophysical Research: Oceans, 2020. Koelling, J.; Send, U.; Lankhorst, M. The dissertation author was the primary investigator and author of this paper.

Chapter 4, in part, is being prepared for submission for publication of the material. Koelling, J.; Send, U.; Lankhorst, M. The dissertation author was the primary investigator and author of this material.

VITA

2013	B. Sc. in Earth and Space Sciences Jacobs University, Bremen, Germany
2013-2020	Graduate Student Researcher Scripps Institution of Oceanography, University of California, San Diego
2016-2019	NASA Earth and Space Sciences Fellowship
2020	Ph. D. in Oceanography Scripps Institution of Oceanography, University of California, San Diego

PUBLICATIONS

Koelling, J., D.W.R. Wallace, U. Send, and J. Karstensen "Intense oceanic uptake of oxygen during 20142015 winter convection in the Labrador Sea", *Geophysical Research Letters*, 44, 2017.

Atamanchuk, D., **Koelling, J.**, Send, U. and Wallace, D.W.R.. "Rapid transfer of oxygen to the deep ocean mediated by bubbles", *Nature Geoscience*, pp.1-6, 2020

ABSTRACT OF THE DISSERTATION

Variability in formation, properties, and transport of North Atlantic Deep Water

by

Jannes Koelling

Doctor of Philosophy in Oceanography

University of California San Diego, 2020

Professor Uwe Send, Chair

North Atlantic Deep Water is found in much of the deep Atlantic Ocean, and its formation in the Labrador and Nordic Seas and subsequent southward export are a vital part of global ocean circulation and Earth's climate system. The overarching goal of this dissertation is to better understand the processes controlling variability of North Atlantic Deep Water formation, properties, and transport in the Atlantic Ocean.

Chapter 1 uses data from the central Labrador Sea during winter to estimate the uptake of oxygen associated with deep convection in 2014–15. The results show that intense air-sea exchange results in an uptake of 29.1 ± 3.8 mol m^{-2} during the convective season, with much of the flux being associated with injection of air bubbles. Chapter 2 looks at lateral fluxes of

carbon, oxygen, and nitrate from the Labrador Sea's boundary current into the center of the basin during the summertime productive season. Lateral fluxes are found to play an important role for the carbon and nitrate budgets immediately below the mixed layer, with respiration rates underestimated by up to 50% if they are ignored.

In Chapter 3, gravity measurements from satellites are used to investigate variability in ocean circulation. After trends in the data are validated using independent measurements, they are used to study decadal circulation changes of North Atlantic Deep Water in the North Atlantic Ocean. The analysis reveals a strengthening of the interior branch of North Atlantic Deep Water flow, with transport increasing by 13.9 ± 3.7 Sv (1 Sv = 10^6 m^3 s^{-1}), balanced by a weaker southward flow in the Deep Western Boundary Current.

A twenty-year record of mooring data is analyzed in Chapter 4 to investigate changes in North Atlantic Deep Water transport at 16°N. Multi-decadal variability is observed in the transport time series, and is largely associated with density changes in the lower half of the North Atlantic Deep Water layer, which in turn appear to be caused by changes in the source region. The data are also compared to another transport time series at 26°N, and similarities and differences are discussed.

Introduction

This dissertation is written in manuscript style, with several largely independent chapters addressing aspects of North Atlantic Deep Water (NADW) formation and circulation in the Atlantic Ocean. The structure mirrors the path of NADW from formation to its spreading throughout the basin, with Chapters 1 and 2 discussing processes in the Labrador Sea, Chapter 3 studying NADW circulation changes in the subtropics, and Chapter 4 looking at transport variability in the tropical Atlantic Ocean. The areas and features studied in the different chapters are highlighted in figure 0.1.

North Atlantic Deep Water is one of the most abundant water masses in the world ocean, making up about a third of the volume of deep waters globally and most of the volume in the Atlantic Ocean (*Johnson*, 2008). The water mass is a combination of several components formed by open-ocean convection in different parts of the subpolar North Atlantic: Labrador Sea Water (LSW), which is formed in the Labrador Sea (*Lazier*, 1973; *Clarke and Gascard*, 1983; *Yashayaev*, 2007), and Denmark Strait and Iceland-Scotland Overflow Water (DSOW/ISOW), formed in the Greenland and Iceland Seas and modified by entrainment upon flowing over sills from the Nordic Seas into the North Atlantic Ocean (*Aagaard et al.*, 1985).

In the Labrador Sea, deep convection occurs in the center of the basin during winter, as intense heat loss to the atmosphere cools surface waters, increasing their density. With sufficient heat loss, the density exceeds that of the underlying waters, and the water column becomes unstable. This instability leads to surface waters sinking to great depths in convective plumes

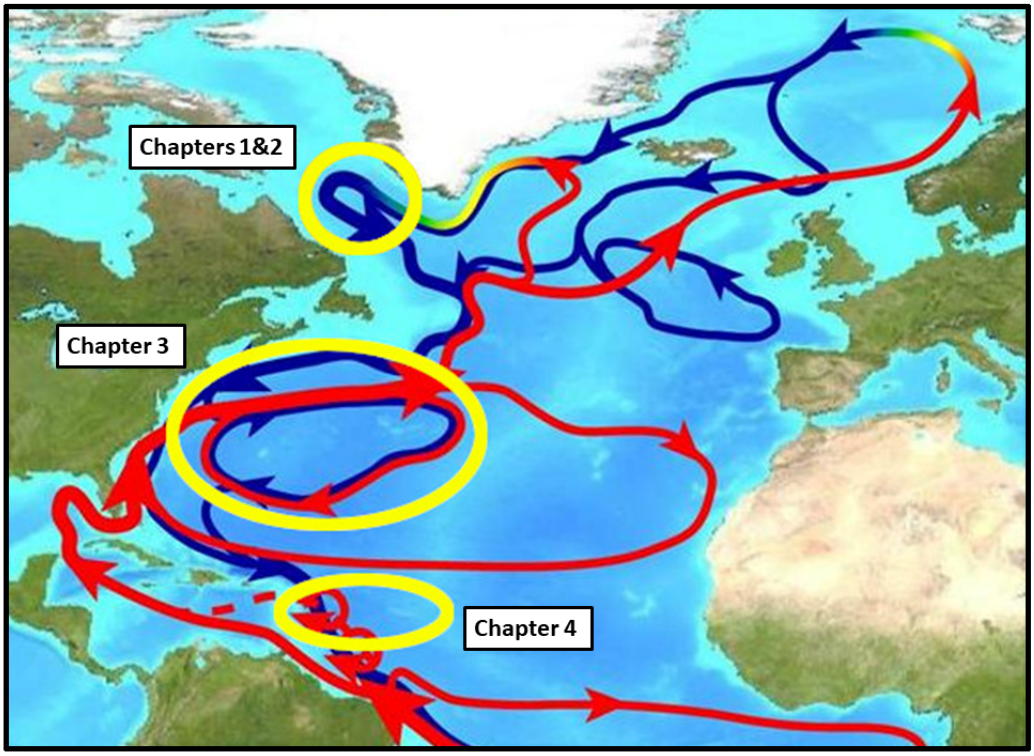

Figure 0.1: Schematic of the Atlantic Meridional Overturning Circulation (AMOC), original by R. Lumpkin[1]. Red lines show surface currents, blue lines show the deep flow of North Atlantic Deep Water that is the focus of this dissertation. Yellow ellipses highlight the areas and features discussed in the individual chapters of this dissertation. Chapters 1 and 2: Gas exchange in the deep water formation region in the central Labrador Sea. Chapter 3: Interior pathways of North Atlantic Deep Water. Chapter 4: Variability of North Atlantic Deep Water transport in the tropical Atlantic.

(*Marshall and Schott*, 1999), which is balanced by a broader upwelling of deep waters in between (*Send and Marshall*, 1995). Convection depth varies from year to year, but is generally at least 1000 m, and it exceeded 2000 m for several years during the early 1990s (*Yashayaev*, 2007). It reached the largest depths since then in 2014-2017 (*Yashayaev and Loder*, 2017). The Labrador Sea is one of the few places in the ocean where convection reaches the deep ocean, so that variability in surface forcing in this relatively small region profoundly affects the properties of much of the global deep ocean. LSW can be traced throughout the Atlantic Ocean by its temperature and salinity properties, and variability in this water mass downstream of the

[1]Downloaded from https://agupubs.onlinelibrary.wiley.com/hub/journal/19449186/call-for-papers.html.

subpolar North Atlantic is related to variability in the source region several years prior (*Talley and McCartney*, 1982; *van Sebille et al.*, 2011; *Le Bras et al.*, 2017).

Deep convection also affects the uptake of oxygen from the atmosphere, as the continuous mixing of the water column constantly brings up deep waters which are undersaturated in oxygen (*Clarke and Coote*, 1988; *Wolf et al.*, 2018). As a result, a strong air-sea oxygen disequilibrium is maintained during convection, driving some of the strongest uptake per unit area found anywhere in the ocean (*McKinley et al.*, 2000; *Rhein et al.*, 2017). This "trap-door" mechanism for oxygen uptake makes the Labrador Sea an important region for supplying oxygen to the global deep ocean (*Atamanchuk et al.*, 2020), and variability in its magnitude can affect oxygen levels at depth (*Schmidtko et al.*, 2017). The region is also a significant sink for carbon (*McKinley et al.*, 2003; *Takahashi et al.*, 2009). Unlike for oxygen, much of the uptake of carbon occurs during the summer months, following biological production during the spring bloom, which uses up inorganic carbon (*Körtzinger et al.*, 2008). As organisms sink below the mixed layer, this carbon is removed in organic form (*Martz et al.*, 2009), before it eventually decomposes and is remineralized into inorganic carbon. When Labrador Sea Water is formed during convection, the carbon from the spring bloom is incorporated into the water mass and exported from the region, removing it from contact with the atmosphere for decades or even centuries (*Matsumoto*, 2007). As a result, the Labrador Sea is considered an important region for storing anthropogenic carbon, i.e. carbon emitted by human activity, from the atmosphere (*Sabine et al.*, 2004; *Steinfeldt et al.*, 2009). Despite the Labrador Sea's importance for the cycling of both oxygen and carbon, there have only been a handful of studies attempting to directly observe the uptake of these gases, and the processes controlling the Labrador Sea oxygen and carbon budgets are not fully understood yet.

The first two chapters of this dissertation are aimed at improving our understanding of some of these processes: Chapter 1 looks at the oxygen uptake during convection in winter. The results highlight the importance of air bubble injection, which is not accounted for in common

parameterizations of air-sea gas exchange. Chapter 2 studies the lateral flux of oxygen, carbon, and nitrogen during the summertime productive season when most of the carbon uptake occurs. These lateral fluxes, which have not been resolved in most previous studies, are shown to be an important part of the budget immediately below the mixed layer, partially counteracting the effect of remineralization on the carbon and nitrogen inventories.

In addition to setting the properties of the deep ocean, the formation of NADW is also crucial for the large-scale circulation of the Atlantic Ocean and global climate. Water formed in the subpolar North Atlantic is exported southward at depth throughout the Atlantic Ocean (*Lozier*, 2010), eventually reaching the Southern Ocean near Antarctica where most of it upwells back to the surface (*Tamsitt et al.*, 2017). The most important conduit for the southward spreading of NADW is the Deep Western Boundary Current, or DWBC (*Toole et al.*, 2017), which hugs the continental shelf of America north of the equator. However, some southward flow of NADW also occurs in the interior of the basin west of the Mid-Atlantic Ridge between about 30°N and 45°N (*Getzlaff et al.*, 2006; *Lozier*, 2010; *Lozier et al.*, 2013). The existence of this interior branch has been hypothesized to be caused by interactions between the Gulf Stream and the DWBC, with eddies sweeping NADW into the Gulf Stream's counterclockwise recirculation gyres in the interior (*Spall*, 1996a; *Lozier*, 1997; *Gary et al.*, 2011). Observational studies of these interior NADW pathways have been limited to studies of property distributions (*Lozier*, 1997; *Smith et al.*, 2016) and from Lagrangian floats (*Bower et al.*, 2009). As a result, not much is known about the mean and variability of the transport in this interior branch.

Chapter 3 addresses this gap in our understanding by analyzing satellite-based measurements of near-bottom circulation changes. The first part of the chapter uses independent measurements to validate ocean mass trends in data from the GRACE (Gravity Recovery and Climate Experiment) satellite mission. These low-frequency changes in GRACE are then used to study changes in the ocean circulation, showing that the interior branch of NADW flow has strengthened relative to the DWBC in recent years.

As water is exported southward from the subpolar North Atlantic as NADW, it is replaced by warmer water in a near-surface branch, which in the northern part of the basin is principally comprised of the Gulf Stream and North Atlantic Current (*Schmitz and McCartney*, 1993; *Lozier*, 2010; *Bower et al.*, 2019). The result is a net northward transport of heat in the ocean, which at 26°N has a mean value of 1.33 PW (petawatts, 1 PW = 10^{15} W) (*Johns et al.*, 2011). Along its path towards the subpolar North Atlantic, the North Atlantic Current loses heat to the atmosphere, warming the air and resulting in relatively mild winters in Europe compared to other regions at the same latitude (*Sutton and Hodson*, 2005). Together, this upper branch and the lower branch carrying NADW make up the so-called Atlantic Meridional Overturning Circulation (AMOC). Given its connection to earth's climate (*Bryden et al.*, 2014), and the significant time-variability in both the AMOC and meridional heat transport (*Srokosz and Bryden*, 2015), there has been considerable effort to understand how and why the AMOC changes on interannual and longer time scales.

These efforts include several long-term observational arrays (*Send et al.*, 2011; *McCarthy et al.*, 2015; *Lozier et al.*, 2017), and a plethora of model studies (*Zhang*, 2010; *Buckley et al.*, 2012; *Marshall and Johnson*, 2013; *Jackson et al.*, 2016; *Johnson et al.*, 2019). Due to the long time scales of interest, much of the literature on the processes responsible for AMOC changes and the propagation of AMOC anomalies has been conducted in either idealized or realistic models. Of particular interest is the response of the AMOC to climate change, with several model and paleo-climate studies suggesting a substantial weakening or complete shutdown of convection and the associated overturning circulation as a result of increased ice melt near Greenland (*Clark et al.*, 2002; *Rahmstorf*, 2002; *Oltmanns et al.*, 2018). At the same time, climate models suggest there is also variability in AMOC strength on a range of time scales from decades to centuries, which is related to natural variability in the ocean-atmosphere system (*Buckley and Marshall*, 2016; *Danabasoglu et al.*, 2010; *Te Raa and Dijkstra*, 2002; *Wen et al.*, 2016). Understanding these natural low-frequency changes in the strength of the AMOC is important both for understanding

their relation to climate patterns, and for being able to differentiate between such natural variability and a possible trend related to climate change (*Smeed et al.*, 2014). Most model studies have found that changes to the AMOC occur initially in or near the deep water formation regions in the subpolar gyre, and these anomalies are subsequently propagated southward by boundary waves (*Zhang*, 2010; *Marshall and Johnson*, 2013; *Johnson et al.*, 2019), but some also show that transport changes can be caused by density anomalies propagating with the mean current along the boundary (*Marotzke and Klinger*, 2000; *Buckley et al.*, 2012; *Han et al.*, 2013).

Chapter 4 uses a 20-year observational time series from the Meridional Overturning Variability Experiment (MOVE) at 16°N to look at low-frequency variability in NADW transport and its causes. The data reveal multi-decadal variability with a time scale of about 15-20 years. This variability is associated largely with density changes in the lower NADW, which appear to be related to changes in the Nordic Seas. The transport changes are compared to data from the RAPID array at 26°N, showing a divergence in the low-frequency variability that seems to be related to how transports are calculated for the two projects.

Chapter 1

Intense oceanic uptake of oxygen during 2014–2015 winter convection in the Labrador Sea

This chapter was published in 2017 as Koelling, J., D. W. R. Wallace, U. Send, and J. Karstensen (2017), Intense oceanic uptake of oxygen during 20142015 winter convection in the Labrador Sea, *Geophysical Research Letters*, *44*(15), 7855–7864, doi: 10.1002/2017GL073933.

Abstract

Measurements of near-surface oxygen (O_2) concentrations and mixed layer depth from the K1 mooring in the central Labrador Sea are used to calculate the change in column-integrated (0–1700 m) O_2 content over the deep convection winter 2014/2015. During the mixed layer deepening period, November 2014 to April 2015, the oxygen content increased by 24.3 ± 3.4 mol m^{-2}, 40% higher than previous results from winters with weaker convection. By estimating the contribution of respiration and lateral transport on the oxygen budget, the cumulative air-sea gas exchange is derived. The O_2 uptake of 29.1 ± 3.8 mol m^{-2}, driven by persistent undersaturation ($\geq 5\%$)

and strong atmospheric forcing, is substantially higher than predicted by standard (nonbubble) gas exchange parameterizations, whereas most bubble-resolving parameterizations predict higher uptake, comparable to our results. Generally large, but varying mixed layer depths and strong heat and momentum fluxes make the Labrador Sea an ideal test bed for process studies aimed at improving gas exchange parameterizations.

1.1 Introduction

The Labrador Sea is one of the few regions where open-ocean deep convection occurs (*Marshall and Schott*, 1999), with Labrador Sea Water (LSW) forming in the interior of the basin (*Lazier*, 1973; *Clarke and Gascard*, 1983) and spreading throughout the Atlantic as part of North Atlantic Deep Water (NADW) (*Talley and McCartney*, 1982). In the LSW formation process, vertical mixing and temperature-driven solubility changes outpace the uptake of atmospheric oxygen by air-sea gas transfer (*Ito et al.*, 2004), resulting in newly formed LSW being about 6% undersaturated relative to equilibrium (*Clarke and Coote*, 1988). This marked air-sea disequilibrium, along with strong winds, makes the Labrador Sea one of the most intense sinks of atmospheric oxygen in the world ocean (*McKinley et al.*, 2003). NADW exports oxygen to the ocean interior, where it plays an important role in supporting respiration and biogeochemical cycling of nutrients and carbon (*Keeling et al.*, 2010). A recent study on changes in the global oxygen content since the 1960s (*Schmidtko et al.*, 2017) found that the amount of oxygen stored in the deep ocean decreased by 702.9 ± 244 Tmol per decade, and suggested that changes in ventilation at high latitudes may have contributed to this decline.

Considering the importance of LSW for the transfer of oxygen from the atmosphere to the global deep ocean, and given the climate sensitivity of its formation (*Curry et al.*, 1998), it is crucial to understand the processes governing variability of air-sea gas exchange in this region. While oxygen data have been collected regularly during hydrographic cruises in the region

(*Stendardo and Gruber*, 2012), there have been relatively few attempts to directly measure the uptake of oxygen during the convection season, including one study of oxygen content changes in 2003–2004 from Argo float data (*Körtzinger et al.*, 2004), and a previous mooring-based study focusing on seasonal cycles of carbon and oxygen in the mixed layer (*Körtzinger et al.*, 2008). The aim of this study is to quantify the total uptake of oxygen between November 2014 and April 2015, a period featuring the deepest convection since 1994 (*Yashayaev and Loder*, 2016), and compare it to these earlier estimates, and to the uptake predicted by several widely-used air-sea gas exchange parameterizations.

1.2 Data and Methods

1.2.1 Data

Observational data used in this study come from the K1 mooring, which is located in the LSW formation region (figure 1.1) and has been continuously measuring temperature and salinity throughout the water column since the early 1990s (*Avsic et al.*, 2006). The three uppermost instruments additionally collected oxygen data for the K1 deployment KPO 1117 analyzed here, using a Seabird Microcat model 43 (*Carlson*, 2002) at depths of 10 m and 100 m, and an Aanderaa Optode model 4835 (*Tengberg et al.*, 2006) at 60 m. The mooring was deployed from August 2014 to May 2016; however, none of the oxygen sensors returned data after May 2015, as all three instruments were either lost or ran out of battery power, limiting our study to the 2014–2015 winter. All instruments were new and calibrated by their respective manufacturers prior to deployment, but a postcalibration of the oxygen sensors was impossible due to the sensor failures outlined above. While both types of sensors have been shown to be susceptible to drift (*D'Asaro and McNeil*, 2013), we find good agreement between the instruments after December 2014, differing only by a constant offset (Figure 1.4 in the supporting information), with no signs of a trend in the differences which would be expected in the case of instrument

drift. We adjust for this offset by matching their values when all three sensors were in the mixed layer, and additionally correct for sensor drift that can occur during storage between the factory calibration and deployment (*Bittig et al.*, 2012) by comparing data collected during the first 15 days of measurements to a conductivity-temperature-depth (CTD) profile taken at the site prior to deployment, adding an offset of 11.25 ± 2 μmol L^{-1} to the mooring data to agree with CTD measurements (Figure 1.5).

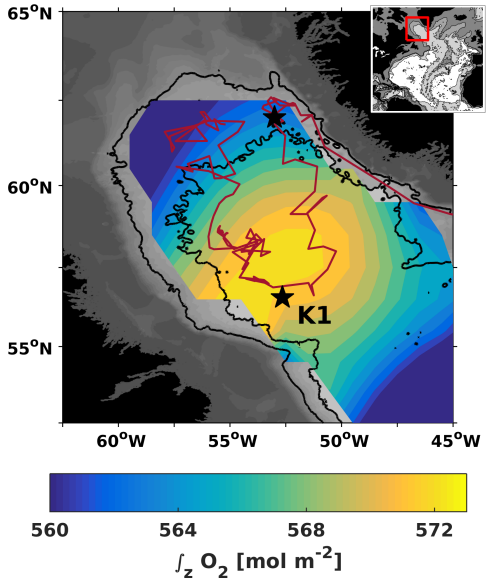

Figure 1.1: Map of the Labrador Sea, with topography as gray background shading, and 2000 m and 3000 m isobaths as black lines; colors show 100–2000m O_2 content from the World Ocean Database (*Levitus et al.*, 2013), red line shows track of Argo float used to estimate F_{lat} (section 1.2.2), and locations of K1 and the eddy formation region are shown as black symbols. Inset shows the location of the study area within the North Atlantic

1.2.2 Oxygen budget

To calculate the change in column-integrated 0–1700 m O_2 content, we combine time series of surface oxygen concentration and mixed layer depth (MLD). For surface data, we use 6-hourly telemetered data from the 10 m instrument, interpolated onto a 1-hour time grid, until December 2014, and 1-hourly measurements from the 60 m instrument afterwards, when

the mixed layer was generally at least several hundred meters deep. Surface concentration and saturation, as well as MLD, estimated using a criterion of $\Delta\sigma_\theta \leq 0.01$ kg m^{-3}, and contours of $O_2(z,t_n)$ (see below), are shown in figure 1.2.

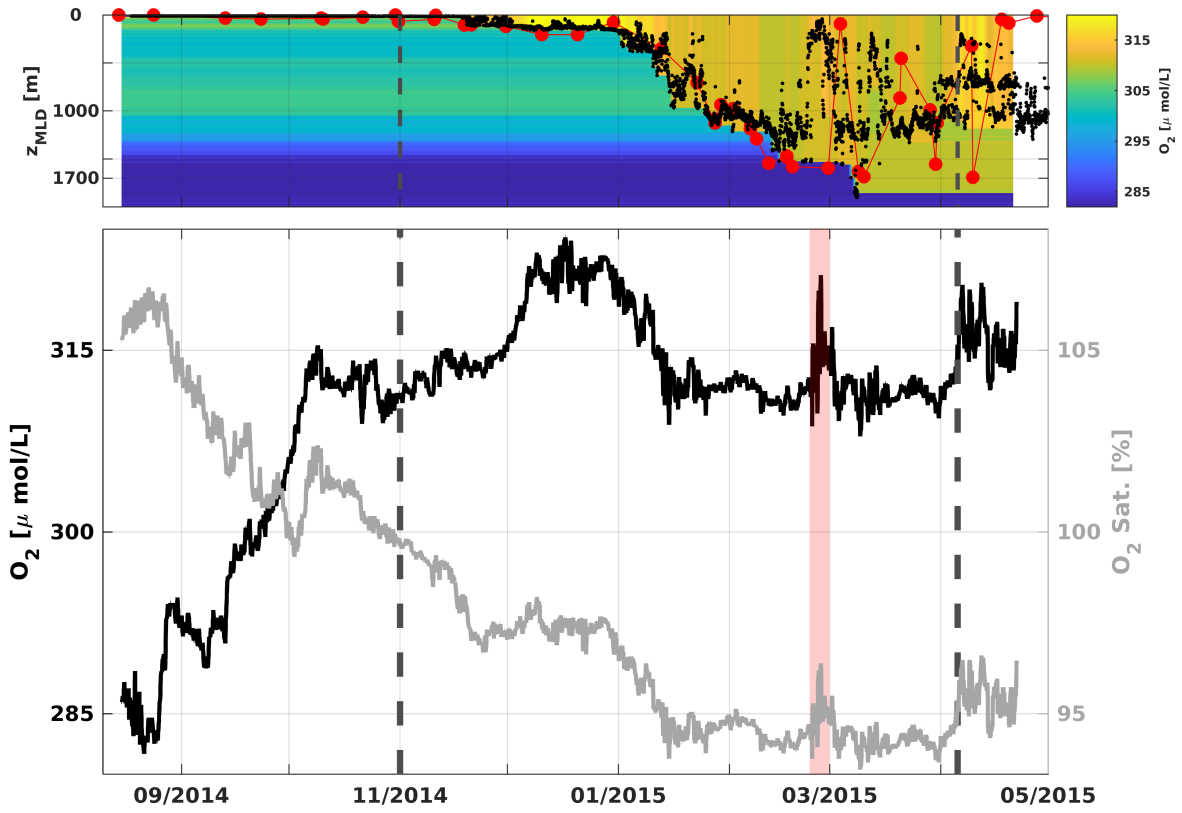

Figure 1.2: (top): Daily mean mixed layer depth, z_{MLD} from mooring data (black dots), instantaneous z_{MLD} from Argo profiles within 100 km of the K1 site (red circles), and contours of $O_2(z,t)$, calculated from equation 1.1. (bottom): Surface oxygen concentration (black) and saturation (gray). Red shading marks the passing of an eddy, and dashed vertical lines show the start and end times for the analysis of gas exchange (figure 1.3)

Oxygen concentrations throughout the water column are estimated by an iterative procedure, starting with a profile $O_2(z,t_0)$, taken from a nearby CTD cast, as the initial condition, and

setting O_2 within the mixed layer to surface values for each time step, such that

$$\begin{aligned} O_2(z,t_n) &= O_{2_{\text{surf}}} && z \leq z_{\text{mld}}(t_n) \\ O_2(z,t_n) &= O_2(z,t_{n-1}) && z > z_{\text{mld}}(t_n), \end{aligned} \tag{1.1}$$

where $O_{2_{\text{surf}}}$ is the surface oxygen concentration, $z_{\text{mld}}(t_n)$ is the mixed layer depth at time t_n, and the oxygen content is calculated as the vertical integral of $O_2(z,t_n)$. This method assumes that oxygen concentrations are constant throughout the mixed layer during convection, which has been shown to be the case with Argo float data (*Körtzinger et al.*, 2004). We further tested this approach with temperature data, comparing heat content estimated from surface temperature and MLD to that calculated using all mixed layer temperature data, and found good agreement (Figure 1.6).

The change in oxygen content is the sum of the fluxes due to gas exchange (F_{gasex}), biological activity (F_{bio}), and lateral exchange through transport processes from outside the convection region (F_{lat}):

$$\int_z O_2(z,t_n) - \int_z O_2(z,t_{n-1}) = \Big(F_{\text{gasex}} + F_{\text{bio}} + F_{\text{lat}}\Big)\Delta t \tag{1.2}$$

F_{gasex} can thus be calculated from the measured oxygen content changes, along with estimates of F_{bio} and F_{lat}. Previous studies have shown that there is heat transport from the boundary current west of Greenland into the central basin, caused by southward propagation of Irminger Current eddies (*Straneo*, 2006; *Yashayaev and Loder*, 2009; *de Jong et al.*, 2016). This can be used to estimate an associated eddy-driven flux of oxygen:

$$F_{\text{lat}} = F_{\text{lat}}^{H} \frac{\Delta \int_z O_2}{\Delta \int_z T c_p \rho}, \tag{1.3}$$

where F_{lat}^{H} is the lateral heat flux inferred from mooring and North American Regional Reanalysis

(NARR) data, and $\frac{\Delta \int_z O_2}{\Delta \int_z T c_p \rho}$ is the ratio of the mean oxygen to heat content gradients between K1 and the eddy formation region at the spreading point of the 2000 m and 3000 m isobaths (*Lilly et al.*, 2003), calculated to be -2.84 ± 0.59 mol $(\mathrm{GJ})^{-1}$ from Argo data. With $F_{\mathrm{lat}}^{H} = 1.01 \pm 0.5$ GJ m^{-2}, equation 1.3 yields $F_{\mathrm{lat}} = -2.9 \pm 1.5$ mol m^{-2}; see Text S1 (section 1.8) for details on the calculation of F_{lat}^{H} and $\frac{\Delta \int_z O_2}{\Delta \int_z T c_p \rho}$.

We assume a net heterotrophic ocean due to light limitation in winter inhibiting production (*Harrison and Li*, 2007). A previous study at the K1 site by *Körtzinger et al.* (2008) used measurements of dissolved inorganic carbon to estimate that 40% of summertime net community production (NCP), amounting to 1.4 ± 0.5 mol C m^{-2}, is remineralized above the base of the winter mixed layer, while the remaining 60% is exported below the depth of convection. Using a stoichiometric ratio of -1.34 O_2:C (*Körtzinger et al.*, 2001), this corresponds to an integrated wintertime flux of -1.9 ± 0.7 mol O_2 m^{-2}, which we use as an estimate of F_{bio} in this study.

1.2.3 Air-Sea gas exchange parameterizations

Several parameterizations for air-sea gas exchange are used to estimate the time-varying gas transfer from the measured surface data, along with wind speed from satellite and atmospheric reanalysis data. All parameterizations involve some measure of the piston velocity k_{660} that is dependent on wind speed:

$$k_{660} = a(U_{10})^n, \tag{1.4}$$

where U_{10} is the wind speed measured at 10 m in the atmosphere, the exponent n is typically chosen as either 2 (*Wanninkhof*, 1992, 2014) or 3 (*Wanninkhof and McGillis*, 1999; *Kihm and Körtzinger*, 2010), and a is an empirically derived constant. k_{660} refers to the piston velocity at a Schmidt number of 660 (*Wanninkhof*, 2014), which corresponds to CO_2 at 20°C, with the piston velocity for any other gas given by $k = k_{660}(\frac{Sc}{660})^{-0.5}$. The diffusive air-sea flux for oxygen is proportional to the difference in the surface concentration, O_2^{sea}, from the equilibrium

concentration, O_2^{sat}, and is given by

$$F_s = k_{\text{O}_2}(\text{O}_2^{\text{sat}} - \text{O}_2^{\text{sea}}), \tag{1.5}$$

with positive values denoting oceanic oxygen uptake. Many commonly used gas exchange parameterizations (*Wanninkhof*, 1992, 2014; *Kihm and Körtzinger*, 2010) assume that the total flux of a gas can be described by equations 1.4 and 1.5, with $F_{\text{gasex}} = F_s$, and use an a priori choice of n and measurements or estimates of all other parameters to find a best fit for a.

However, particularly for less soluble gases and at high wind speeds, there is also an important contribution from air injection, and the flux is more accurately represented by $F_{\text{gasex}} = F_s + F_p + F_c$ (*Liang et al.*, 2013), with F_p and F_c referring to the flux from partially and completely dissolving bubbles, respectively. F_p, like F_s, depends on wind speed and concentration difference, but has an additional term accounting for the hydrostatic pressure in large bubbles; F_c depends only on the wind speed and the atmospheric mole fraction of the respective gas, χ (*Emerson and Bushinsky*, 2016). The gas exchange parameterizations with bubble terms used in this study are those of *Woolf and Thorpe* (1991), *Woolf* (1997), *Stanley et al.* (2009), *Vagle et al.* (2010), and *Liang et al.* (2013). The inverse method used in *Vagle et al.* (2010) to parameterize gas exchange only includes data for $U_{10} > 12$ m s^{-1}, and is therefore poorly constrained below this threshold; we complement their parameterization by using the relationship of *Woolf and Thorpe* (1991) for $U_{10} \leq 12$ m s^{-1}.

Oxygen solubility is calculated from the equations of *Garcia and Gordon* (1992), and corrected for pressure effects following *Benson and Krause* (1984), using barometric pressure from the Fleet Numerical Meteorology and Oceanography Center (FNMOC) product. For wind speed, we use data from the cross-calibrated multiplatform (CCMP) product (*Atlas et al.*, 2011), European Centre for Medium-Range Weather Forecasts ERA-interim (ERAI, *Dee et al.*, 2011), the National Centers for Environmental Prediction (NCEP) North American Regional Reanalysis

Table 1.1: Components of the oxygen budget (equation 1.2), and gas exchange estimated from different parameterizations using NARR wind speed data, integrated from November-April. The terms included in the parameterizations are given in the left column; F_s: diffusive gas exchange; F_p: partially dissolving bubbles; F_c: completely dissolving bubbles

Parameter	Reference	O_2 (mol m^{-2})	Diff. (%)
0–1700 m inv. change ($\Delta \int_z O_2$)	This study	24.3 ± 3.4	
Lateral transport (F_{lat})	This study	-2.9 ± 1.5	
Biological activity (F_{bio})	*Körtzinger et al.* (2008)	-1.9 ± 0.7	
Total gas exchange	This study	29.1 ± 3.8	
F_s	*Wanninkhof* (2014) (W14)	9.2 ± 2.1	-69
F_s	*Wanninkhof* (1992) (W92)	11.4 ± 2.6	-61
F_s	*Kihm and Körtzinger* (2010) (KK10)	14.9 ± 3.6	-49
$F_s + F_p$	*Woolf and Thorpe* (1991) (WT91)	10.6 ± 1.2	-64
$F_s + F_p + F_c$	*Liang et al.* (2013) (L13)	19.8 ± 2.4	-32
$F_s + F_p$	*Woolf* (1997) (W97)	28.8 ± 3.1	-1
$F_s + F_p + F_c$	*Stanley et al.* (2009) (S09)	31.5 ± 2.6	$+8$
$F_s + F_c$	*Vagle et al.* (2010) (V10)	38.2 ± 3.2	$+31$

(NARR, *Mesinger et al.*, 2006), and CMC GDPS reforecasts (CGRF, *Smith et al.*, 2014). Wind speed data from NARR compare most favorably with observations in the Irminger Sea and off Cape Farewell (*Moore et al.*, 2008; *Renfrew et al.*, 2009), with a slope of 0.99 between observational and reanalysis data, and a bias of $-1.5\, m\, s^{-1}$, reported by *Renfrew et al.* (2009). NARR data are corrected for this bias and used to calculate the gas exchange estimates shown in Table 1.1, and results based on data from all products are compared in Figure 1.3. The data were interpolated from their native 6-hourly (FNMOC, CCMP, and ERAI), 3-hourly (NARR), or 1-hourly (CGRF) resolution onto the 1-hourly time grid used in this study.

1.3 Results

Surface concentration and saturation of oxygen, along with MLD, are shown in figure 1.2; the concentration rapidly increased in early December to peak values of $\sim$320 μmol L^{-1} ($\sim$97% saturation), as the mixed layer was still relatively shallow and some of the strongest winds in our records (Figure 1.7) drove increased uptake, then dropped to around 310 μ mol L^{-1} at 95% saturation in early January, when the mixed layer started deepening at a higher rate, and continued

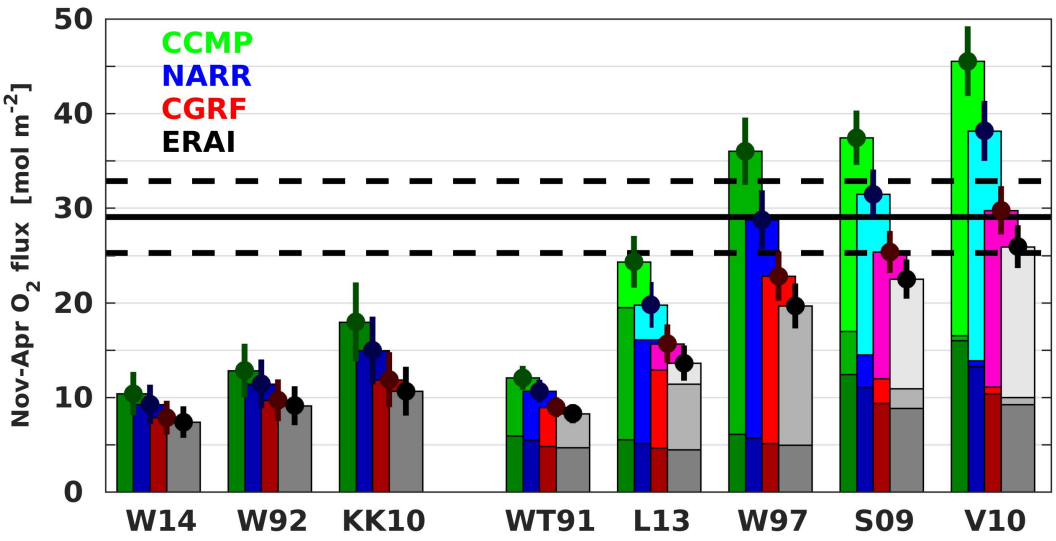

Figure 1.3: Horizontal lines show cumulative (November–April) uptake of oxygen at K1, calculated from equation 1.2, with confidence interval. Bars and symbols show the analogous November–April O_2 uptake calculated from different parameterizations. Colors correspond to different wind speed products, and the shading of the bars shows contributions of F_s (darkest), F_p (intermediate), and F_c (lightest). Abbreviations are defined in table 1.1; a gap separates parameterizations with and without bubbles

to decrease slightly throughout the rest of winter. MLD calculated from the mooring data agrees well with individual Argo profiles taken within 100 km of the mooring before early April, after which the mixed layer shoaled to a depth shallower than the uppermost available measurements, resulting in mooring data overestimating z_{MLD}. We therefore limit our analysis of gas exchange to the period from 1 November, when oxygen saturation dropped below 100%, to 5 April, marking the last time step for which the shallowest measurement is within the mixed layer.

The difference in oxygen content between 1 November and 5 April, calculated from equation 1.1, is 24.3 ± 3.4 mol m^{-2}. For the same time period, F_{lat} is calculated to be -2.9 ± 1.5 mol m^{-2} using equation 1.3, and F_{bio} is estimated as -1.9 ± 0.7 mol m^{-2} (see section 1.2.2). The resulting estimate for air-sea gas exchange in the Labrador Sea during the 2014–2015 winter,

calculated from equation 1.2, is 29.1 ± 3.8 mol m^{-2}, and is compared with the cumulative gas exchange estimates predicted by different parameterizations in figure 1.3; the results are also summarized in Table 1.1.

All gas exchange parameterizations including only an F_s term (equation 1.5) underestimate the uptake of oxygen over the convection season by 49% or more using NARR winds; additional such parameterizations not shown here (e.g. *Liss and Merlivat* (1986); *Nightingale et al.* (2000); *Sweeney et al.* (2007); *Wanninkhof et al.* (2009)) generally fall below that of *Wanninkhof* (1992) at high wind speeds (*Körtzinger et al.*, 2008) and will therefore similarly predict a lower flux than observed. With the exception of *Woolf and Thorpe* (1991), the bubble-resolving parameterizations predict a greater uptake than the purely diffusive ones, but there is considerable variability between them, with estimates ranging from 19.8 ± 2.4 mol m^{-2} (*Liang et al.*, 2013) to 38.2 ± 3.2 mol m^{-2} (*Vagle et al.*, 2010). Two parameterizations, *Woolf* (1997) and *Stanley et al.* (2009), agree within the error with the observed gas exchange, at 28.8 ± 3.1 mol m^{-2} and 31.5 ± 2.6 mol m^{-2}.

1.4 Discussion

1.4.1 Observed change

The 0–1700m depth range used to calculate the oxygen content is chosen to reflect conditions typical of the entire central Labrador Sea, as *Yashayaev and Loder* (2016) determined 1700 m to be the aggregate depth of convection during that winter. Our data show that the water column at the mooring site was homogenized to more than 1800 m during an event in March lasting several days, reaching a maximum of 1850 m on 8 March (Figure 1.2). However, Argo profiles taken within 100 km of the mooring show no evidence of convection reaching below 1700 m, suggesting that this was a small-scale feature, such as a convective plume (*Marshall and Schott*, 1999) or passing cold-core eddy (*Avsic et al.*, 2006), and we do not expect these deeper mixed layers to be representative of the whole region.

The change in 0–1700m oxygen content observed between 1 November and 5 April is 24.3 ± 3.4 mol m^{-2}, 40% higher than the increase of 17 mol m^{-2} observed by *Körtzinger et al.* (2004) over a comparable time period in the 2003/2004 winter, when convection reached about 1400 m. *Stendardo and Gruber* (2012) found evidence for a connection between oxygen content in the deep North Atlantic and variability related to the North Atlantic Oscillation (NAO), and data from biogeochemical models suggest that Labrador Sea oxygen uptake is strongest during the positive phase of the NAO (*McKinley et al.*, 2003), which is associated with both higher wind speeds and stronger surface heat loss in the Labrador Sea (*Hurrell et al.*, 2013), resulting in generally deeper convection (*Curry et al.*, 1998; *Yashayaev and Loder*, 2016). The NAO was positive in 2014–2015, and weakly negative during the 2003–2004 period of *Körtzinger et al.* (2004), consistent with these earlier results. The oxygen content change we observe in the upper 1400 m is 16.3 ± 2.8 mol m^{-2}, in good agreement with *Körtzinger et al.* (2004)'s estimate, which could suggest that the higher uptake of oxygen in 2014–2015 is caused by convection penetrating to greater depth, enhancing upward mixing of low-saturation deep waters. However, the increased wind forcing and solubility pump during positive NAO years would also be expected to increase the flux of O_2, and more sustained observations will be necessary to better understand the mechanisms responsible for the link between the NAO and oxygen uptake.

Assuming that our results are representative of the whole convection region, with an approximate area of 100,000 km^2, the difference in oxygen content change between a positive (2014–2015) and neutral (2003–2004) NAO winter, 7.3 ± 3.4 mol m^{-2}, corresponds to about 0.73 ± 0.34 Tmol (yr)$^{-1}$, only 1% of the global loss of 702.9 ± 244 Tmol (decade)$^{-1}$ ($= 70.3 \pm 24.4$ Tmol (yr)$^{-1}$) reported by *Schmidtko et al.* (2017), suggesting that changes in air-sea gas exchange in the Labrador Sea alone are unlikely to have played a major role in the decline of the oceanic oxygen content in recent decades. However, the effect of LSW on the global circulation (*Jackson et al.*, 2016) and interannual variability in its export (*Yashayaev and Loder*, 2016) also plays a role in controlling ventilation of the deep ocean, and will need to be more thoroughly

studied to fully understand its impact on the global oxygen budget.

1.4.2 Gas exchange parameterizations

While the importance of bubbles in air-sea gas exchange has been emphasized for some time (*Thorpe*, 1982; *Woolf and Thorpe*, 1991; *Wallace and Wirick*, 1992; *Keeling*, 1993), parameterizations that do not account for their effect are still widely used. Many such parameterizations were derived for CO_2, which is more soluble than oxygen and therefore less affected by bubble processes (*Woolf and Thorpe*, 1991; *Liang et al.*, 2013), but are assumed to hold for other gases if scaled by the Schmidt number. As shown in Figure 1.3, neglecting bubble process is not appropriate for oxygen in the Labrador Sea, with the parameterizations of *Wanninkhof* (1992, 2014) and *Kihm and Körtzinger* (2010) underestimating the observed uptake by 49-69% when calculated with NARR wind data. In addition to being used in observational studies, many of the models included in the Climate Model Intercomparison Project (CMIP5, *Taylor et al.* (2012)) also utilize the parameterization of *Wanninkhof* (1992), or a slight variation thereof, to compute air-sea gas exchange of O_2, CO_2, and other gases (*Weaver et al.*, 2001; *Tjiputra et al.*, 2010; *Dufresne et al.*, 2013; *Dunne et al.*, 2013; *Ilyina et al.*, 2013). Considering the large discrepancy between our results and the flux predicted from the *Wanninkhof* (1992) parameterization, we expect these global models to underestimate the strength of oxygen sinks at high latitudes, where strong winds and bubble injection are most prevalent.

Despite accounting for bubbles, both the *Woolf and Thorpe* (1991) and *Liang et al.* (2013) parameterizations underestimate the uptake, by around 60% and 30%, respectively. In contrast, recent studies on noble gas supersaturation (*Emerson and Bushinsky*, 2016) and on O_2 uptake in relation to net community production (*Plant et al.*, 2016) in the Pacific Ocean found that *Liang et al.* (2013) provided the best fit to their data. The poorer performance of *Liang et al.* (2013) in the present study is likely related to the lower surface saturation and stronger physical forcing in the form of winds, wave breaking, and convection, and could reflect either real regional variability

in bubble processes, or shortcomings of the parameterization in accurately predicting them in conditions typical of the Labrador Sea.

All other bubble-resolving parameterizations predict considerably higher uptake, closer to the observed gas exchange. While the parameterizations of *Woolf* (1997) and *Stanley et al.* (2009) agree within uncertainty bounds with the observed cumulative gas exchange, the estimate from the parameterization of *Vagle et al.* (2010) is 30% higher than the observed uptake when calculated with NARR wind speed data. However, *Vagle et al.* (2010)'s relationships between wind speed, bubble penetration depth, and gas exchange were derived using wind data from the NCEP/NCAR (National Center for Atmospheric Research) reanalysis (*Kalnay et al.*, 1996), which are biased low relative to NARR (*Renfrew et al.*, 2009); recalculating the gas exchange with the NCEP product yields an estimate of 30.5 ± 2.6 mol m^{-2}, matching the observed uptake. This difference of almost 30% illustrates the high sensitivity to the choice of wind speed product (see also Figure 1.3), with discrepancies between products resulting in biases that need to be accounted for when using parameterizations to estimate gas exchange in budget calculations. Our assessment that bubble terms are necessary to accurately determine the flux of oxygen at high latitudes is not dependent on which of the common wind speed products we use, and possible biases are too small to alter our conclusion: some of the products used here have been shown to have biases up to 3 m s^{-1} at high (>20 m s^{-1}) wind speeds (*Renfrew et al.*, 2009; *Li et al.*, 2013), but only 2.5% of the NARR data at K1 are above this threshold. Even if a bias underestimating the winds was present for a broader wind speed range (e.g., $U_{10} > 15$ m s^{-1}), it would have to exceed 13 m s^{-1} (*Wanninkhof*, 1992), 19 m s^{-1} (*Wanninkhof*, 2014) or 5 m s^{-1} (*Kihm and Körtzinger*, 2010) for these nonbubble parameterizations to agree within the error with the observed cumulative oxygen uptake.

An additional source of uncertainty are the assumptions underlying our estimates of F_{bio} and F_{lat}, which are difficult to validate given the sparsity of relevant data from the region. For F_{bio}, previous studies have shown that there is almost no primary production during winter

in the Labrador basin (*Harrison and Li*, 2007; *Harrison et al.*, 2013; *Körtzinger et al.*, 2008), suggesting net heterotrophic conditions with $F_{\text{bio}} \leq 0$. Since K1 is situated within the region of maximum oxygen content (figure 1.1), there cannot be a positive flux from mixing with waters from outside the central LS, such that $F_{\text{lat}} \leq 0$. This allows us to establish a lower bound for the estimated gas exchange, with $F_{\text{bio}} = F_{\text{lat}} = 0$. In this scenario, where $\Delta \int_z \text{O}_2 = F_{\text{gasex}}$, the nonbubble parameterizations still predict a lower gas exchange than we observe (Figure 1.9), showing that their low bias persists regardless of these assumptions. However, there is likely to be additional variability for both processes that cannot be resolved here; the amount of wintertime respiration is expected to vary with the strength of the preceding spring bloom, and seasonal or interannual variability may exist in the boundary-interior gradients of heat and O_2, affecting the magnitude of F_{lat}.

The parameterizations of *Stanley et al.* (2009), *Vagle et al.* (2010) and *Liang et al.* (2013) agree well in the relative strength of the diffusive and bubble flux, with 26% to 35% of the total flux coming from F_s, but the importance of the two bubble terms differs between the different models: F_p and F_c are responsible for 55% and 19% in *Liang et al.* (2013), 11% and 54% in *Stanley et al.* (2009), and 1.5% and 64% in *Vagle et al.* (2010). These differences show that there is still considerable uncertainty not only regarding the strength of bubble-induced gas exchange, but also about the underlying dynamics.

1.5 Outlook

Our results show that *in situ* measurements from moorings can be used to estimate the seasonal change in oxygen content, even with relatively sparse instrumentation. Measuring oxygen in locations like the Labrador Sea may prove to be an important tool for future gas exchange studies, with severe undersaturation throughout the winter months resulting in a strong and persistent signal, which mitigates the effect of measurement uncertainty on estimates of

transfer velocity. As an example, using flux measurements at 95% saturation to infer the transfer velocity, the range of estimates resulting from a ± 2 μmol L^{-1} offset in the sensor calibration is reduced by a factor of 7.7 compared to the same calculation at 99% saturation (see Text S2 in section 1.8 for details).

Recent advances in the in situ calibration and correction of oxygen sensors on Argo floats (*Takeshita et al.*, 2013; *Uchida et al.*, 2008; *Bittig et al.*, 2014), along with the extension of the Argo-Oxygen program (*Gruber et al.*, 2010), will enable studies of the spatial and interannual variability of the Labrador Sea's oxygen content, and help put our findings into a broader context. However, the poor temporal resolution of float data will be insufficient to resolve the intense fluxes of oxygen on short time scales that have been observed in moored measurements (*Wallace and Wirick*, 1992; *Vagle et al.*, 2010). An ideal observing system of oxygen transfer in the Labrador Sea should include high-frequency measurements of inventory changes from moorings to provide information on fluxes occurring on these shorter time scales, complemented by the more extensive, but lower-frequency data from the Argo program.

1.6 Conclusion

The change in Labrador Sea oxygen content of 24.3 ± 3.4 mol m^{-2} during the 2014–2015 winter is more than 40% higher than the 17 mol m^{-2} observed in the 2003–2004 winter by *Körtzinger et al.* (2004). We attribute this to more intense air-sea gas exchange caused by unusually deep convection (1700 m, *Yashayaev and Loder* (2016)), and increased atmospheric forcing during the positive NAO phase, in agreement with earlier studies from hydrography and models (*Stendardo and Gruber*, 2012; *McKinley et al.*, 2003). Wintertime oxygen uptake is calculated as 29.1 ± 3.8 mol m^{-2} from the measured O_2 content change and an estimated 4.8 ± 1.7 mol m^{-2} loss through lateral transport and respiration.

Gas exchange parameterizations including only an F_s term invariably predict a lower

November - April integrated oxygen uptake than we observe, even in the lower limit of zero biological and lateral transport fluxes. The cumulative air-sea flux calculated from bubble-resolving models is generally higher, with three of the five parameterizations considered in this study predicting an uptake of oxygen similar to our estimate, showing that resolving the impact of bubbles is essential for accurate estimation of net air-sea gas fluxes, even when the ocean is strongly ($\geq 5\%$) undersaturated relative to the atmosphere. However, there is substantial variation between parameterizations both in magnitude, and in the partitioning of the flux between the different bubble processes.

Studying wintertime gas transfer in the Labrador Sea can help uncover the processes controlling gas exchange under the extreme atmospheric forcing and strong undersaturation of mixed layer oxygen characteristic of high latitudes, and elucidate similarities and differences to the typically milder conditions in the subtropical and tropical oceans.

1.7 Acknowledgments

The authors would like to thank Dariia Atamanchuk, Craig McNeil, Mitchell Wolf, and Roberta Hamme for their helpful discussions and advice. Canadian support was via the Canada Excellence Research Chair in Ocean Science and Technology and the NSERC-supported VITALS (Ventilation, Interactions and Transport Across the Labrador Sea) project. K1 is part of the OceanSITES mooring network. Analysis was supported by the BMBF RACE II project, by the European Union's Horizon 2020 research and innovation programme under grant agreement No 633211 (AtlantOS), and by European Union's Seventh Framework Program (FP7/2007-2013) under grant agreement 308299 (NACLIM). Mooring and hydrography data used in this study are available from the authors on request, and will also be made available online by GEOMAR. CCMP version 2.0 vector wind analyses are produced by Remote Sensing Systems. Data are available at www.remss.com. NCEP Reanalysis data were provided by the NOAA/OAR/ESRL

PSD, Boulder, Colorado, USA, from their Web site at http://www.esrl.noaa.gov/psd/. CGRF forcing fields made available by Environment and Climate Change Canada. Argo data were collected and made freely available by the International Argo Program and the national programs that contribute to it (http://www.argo.ucsd.edu, http://argo.jcommops.org). The Argo Program is part of the Global Ocean Observing System.

Chapter 1, in full, is a reprint with minor modifications of the material as it appears in Geophysical Research Letters, 2017. Koelling, J.; Wallace, D.W.R.; Send, U.; Karstensen, J. The dissertation author was the primary investigator and author of this paper.

1.8 Supporting information

Text S1.

We use data from an Argo float crossing from the boundary into the interior in 2016 to infer a ratio between the gradients of heat and oxygen content, shown in Figure 1.8, using 7 data points from the eddy formation region, and 8 data points at K1 to estimate $\frac{\Delta \int_z O_2}{\Delta \int_z T c_p \rho} = \frac{\int_z \overline{O_2}(K1) - \int_z \overline{O_2}(IC)}{\int_z \overline{T c_p \rho}(K1) - \int_z \overline{T c_p \rho}(IC)}$. The depth range used for the calculation is 100-1400 m, as the deepest available measurement for each profile is between 1400 m and 1500 m, with the upper limit of integration chosen to avoid seasonal bias due to biology in the upper ocean. The resulting estimate of $\frac{\Delta \int_z O_2}{\Delta \int_z T c_p \rho}$ is -2.84±0.59 mol (GJ)$^{-1}$ (mean and standard deviation).

The lateral heat flux is calculated as the difference between measured heat content from all available mooring data between the surface and 1700m and cumulative surface heat flux from NARR data. An error of 38 W m^{-2}, or 0.5 GJ m^{-2} over the whole study period, is used for the air-sea flux (*Renfrew et al.*, 2009). The change in heat content between November 1st and April 5th is -2.9 GJ m^{-2}, with a cumulative surface flux of -3.91 ± 0.5 GJ m^{-2} from NARR, yielding a lateral heat flux of 1.01 ± 0.5 GJ m^{-2}.

Text S2.

Assuming that bubble fluxes are negligible and the flux is calculated as purely diffusive, the piston velocity k_{O_2} is given by

$$k_{\mathrm{O_2}} = \frac{F_{\mathrm{O_2}}}{\mathrm{O_2^{sat}} - \mathrm{O_2^{sea}}} \tag{1.6}$$

At a saturation of 99%, $\mathrm{O_2^{sat}}$ - $\mathrm{O_2^{sea}} \sim 3.3 \mu$mol L^{-1}, and an uncertainty of $\pm 2 \mu$mol L^{-1} for the oxygen measurements will lead to a range for the estimate of $k_{\mathrm{O_2}}$ of $\frac{3.3}{5.3}$ - $\frac{3.3}{1.3}\hat{k_{\mathrm{O_2}}}$, = 0.62 - 2.54$\hat{k_{\mathrm{O_2}}}$, where $\hat{k_{\mathrm{O_2}}}$ is $k_{\mathrm{O_2}}$ calculated assuming no calibration error. In contrast, with a typical winter

surface saturation for oxygen of 95% in the Labrador Sea, O_2^{sat} - $O_2^{sea} \sim 16.5 \mu$mol L^{-1}, and the range of k_{O_2} is $0.89 - 1.14\hat{k_{O_2}}$, reducing the uncertainty in k_{O_2} by a factor of 7.7.

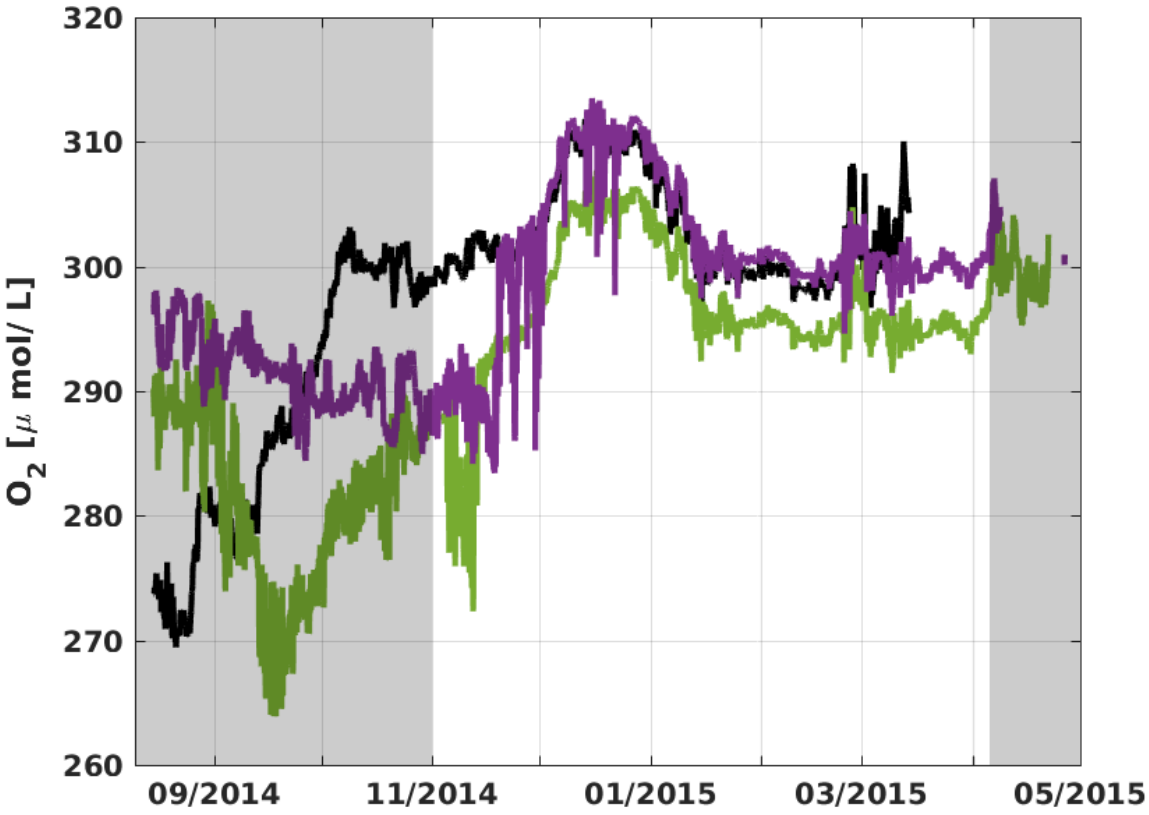

Figure 1.4: Uncorrected oxygen concentration measured at 10m (black), 60m (green) and 100m (purple). When the mixed layer encompasses all three sensors (after mid-December), short-term variability between sensors agrees well, but there are constant offsets of 4 μmol/L, 1 μmol/L, and 5.18 μmol/L, respectively, between 10m and 60m, 10m and 100m and 60m and 100m, with no significant trend, indicative of instrument drift, in either of those differences. We add a constant value to the 10m and 60m sensors to match the mean value of the 100m sensor. (Note that there is no significance to the choice of 100m as the "true" value, as the O_2 data are further corrected using CTD data, see figure 1.5).

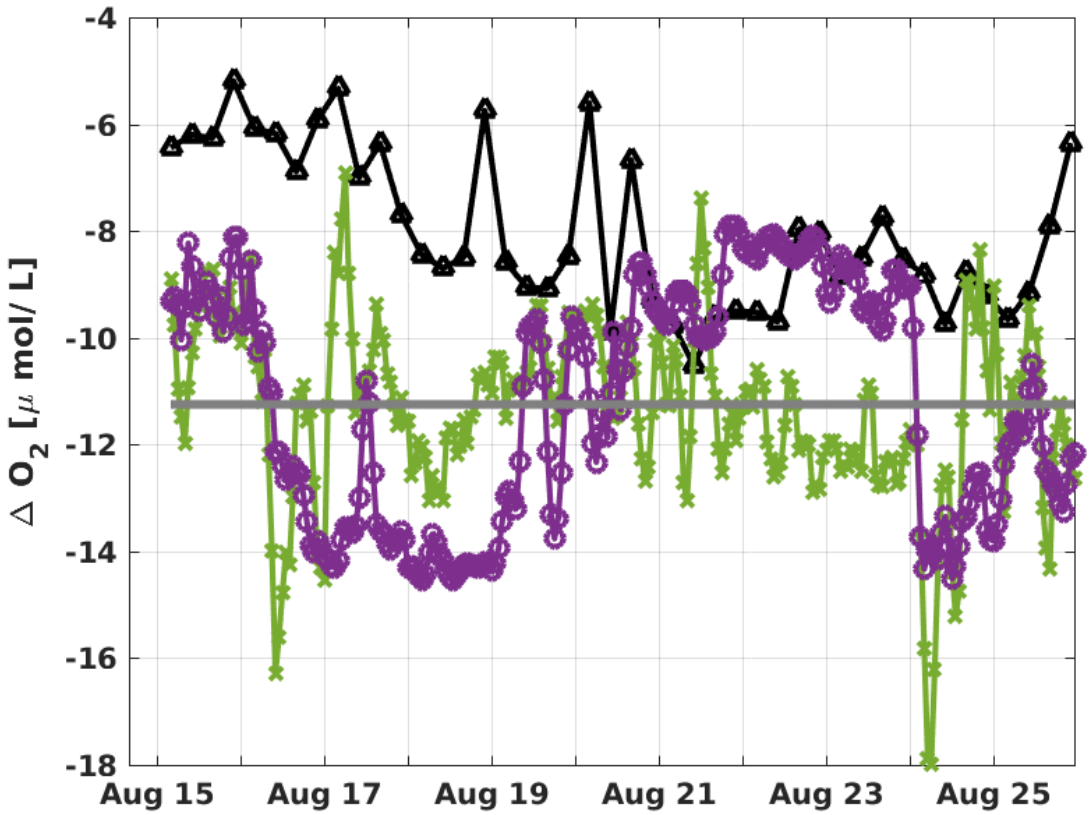

Figure 1.5: Difference between corrected (see figure 1.4) mooring data and a CTD profile taken shortly before deployment at 10m (black), 60m (green) and 100m (purple). CTD data were collected during cruise MSM40 onboard RV Thalassa, and were corrected by comparison with water samples analyzed by Winkler titration. The offset O_2(K1) - O_2(CTD) is -8.1, -11.2, -11.3 μmol L^{-1} at 10, 60 and 100m, respectively. We subtract the mean of the offsets from the two instruments at 60m and 100m, which are well below the mixed layer, from the mooring data to correct for pre-deployment instrument drift. The mean offset is -11.25 μmol L^{-1}, with a standard deviation of 2 μmol L^{-1}, which we use as an estimate of the measurement uncertainty.

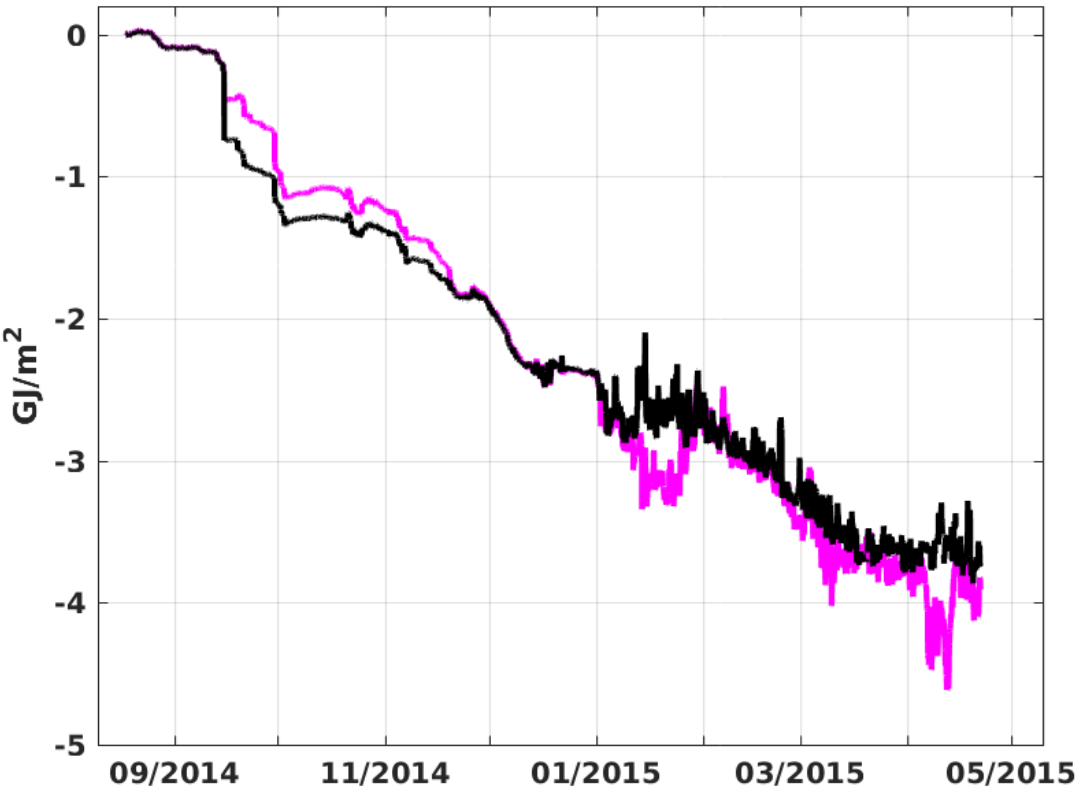

Figure 1.6: Change in mixed layer heat content calculated from all 11 sensors that are within the mixed layer at each time (black), and calculated from near-surface temperature and z_{MLD} only, analogous to the method used for oxygen (magenta)

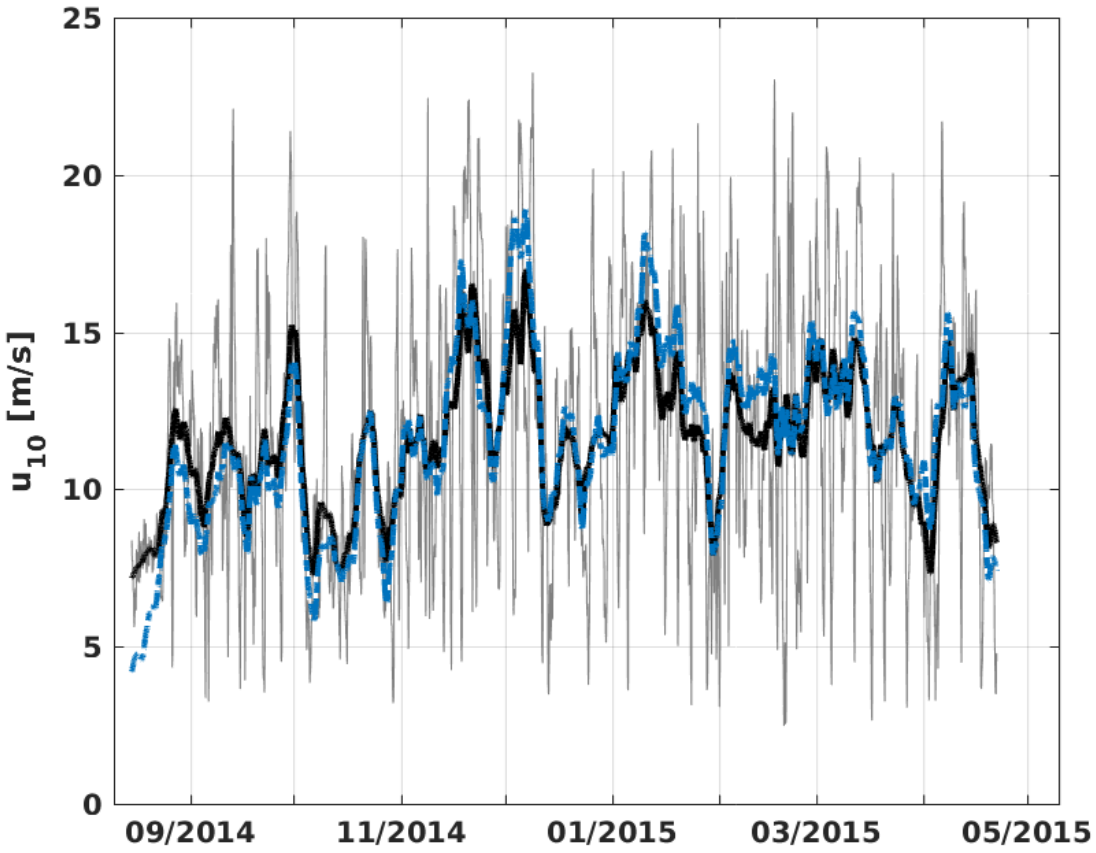

Figure 1.7: 10m wind speed from NARR, 6-hourly values and 5-day running mean, and 5-day running mean of CCMP winds

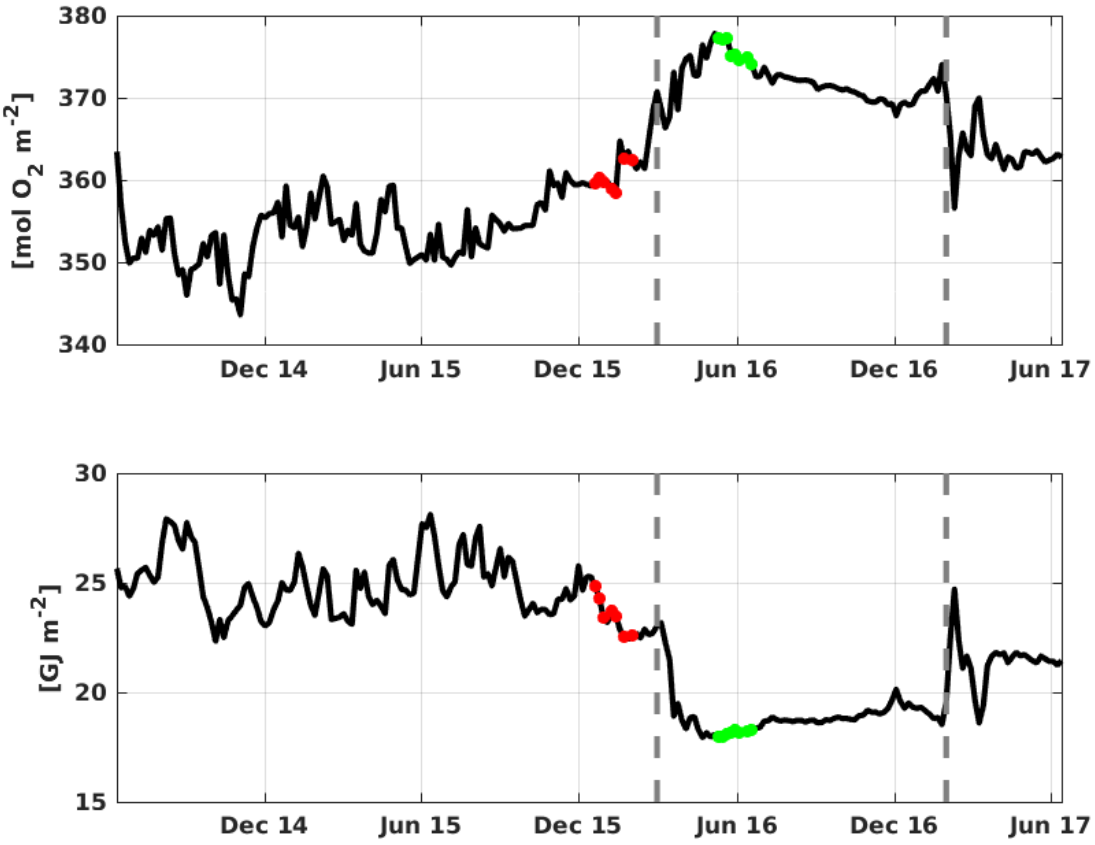

Figure 1.8: 100-1400m oxygen (top) and heat (bottom) content measured by Argo float #5904989. Gray bars show times when the float entered and subsequently exited the central basin, and symbols show the points used to derive the O_2/heat ratio in F_{adv} for the IC eddy formation region (red) and central Labrador Sea close to K1 (green)

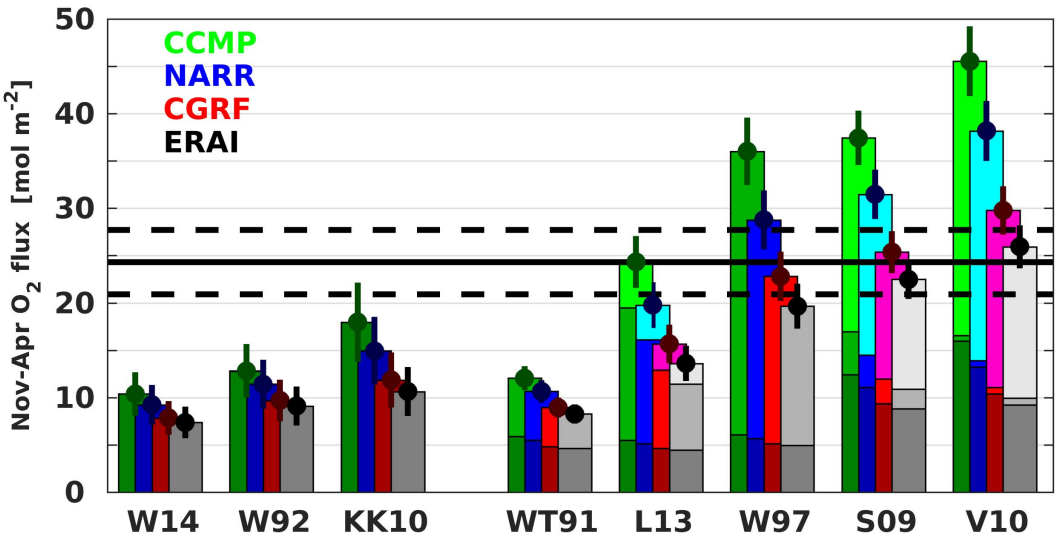

Figure 1.9: As in figure 1.3, but assuming no loss of oxygen through lateral transport or respiration, such that $F_{\text{gasex}} = \Delta \int O_2$

Chapter 2

Lateral flux of carbon, oxygen, and nitrate into the central Labrador Sea

2.1 Introduction

The Labrador Sea is one of the few regions in the world where surface water is exported to depth. During winter, water at the surface becomes dense enough to sink to depths of up to 2000m, becoming part of North Atlantic Deep Water, NADW (*Yashayaev*, 2007). As a result, conditions at the surface in the Labrador Sea set the properties of much of the deep ocean globally. This is true not only for physical properties, but also for dissolved gases such as oxygen (O_2) (*McKinley et al.*, 2003) and carbon dioxide (CO_2) (*Takahashi et al.*, 2009). The Labrador Sea is a net sink for both oxygen and carbon over an annual cycle (*Atamanchuk et al.*, 2020), so that there is a net flux of both of these gases into the deep ocean. The bulk of the oxygen gas exchange occurs during the winter, when deep convection mixes undersaturated water up to the surface, and the resulting air-sea disequilibrium drives an uptake of almost 30 mol m^{-2} (*Koelling et al.*, 2017). For CO_2, the uptake during deep convection in winter is small, and much of the gas exchange occurs during summer. The driving mechanism is the spring bloom, during which organisms use

up dissolved carbon, leading to a strong undersaturation in the mixed layer (*Körtzinger et al.*, 2008). As a result, the sea surface is undersaturated compared to the atmosphere, driving uptake of carbon. Organisms formed as a result of the spring bloom sink out of the mixed layer, exporting carbon (*Martz et al.*, 2009). At the same time, oxygen is produced during the bloom, which together with solubility changes due to surface heating causes an outgassing that partially offsets the wintertime uptake.

In addition to the biological forcing and air-sea gas exchange, the inventory of these gases is also affected by physical processes, such as entrainment during mixed layer deepening, and lateral fluxes. The mean flow in the interior Labrador Sea is weak (*Avsic et al.*, 2006), but properties are affected by an influx of eddies resulting from instabilities in the boundary current, the majority of which are formed to the southwest of Greenland (*Eden and Böning*, 2002; *Lilly et al.*, 2003). This has been shown to be an important part of the heat and freshwater budgets (*Straneo*, 2006), and indeed is important for maintaining convective activity in the interior of the basin (*Johnson et al.*, 2019).

Relatively little is known on the effect of this lateral flux for biogeochemical properties, mostly due to a lack of data. Both *Wolf et al.* (2018) and *Koelling et al.* (2017) (Chapter 1) estimated the effect of the influx of boundary current water for the 0-2000m oxygen budget based on time-mean values, finding that it leads to a loss of about 6 mol m^{-2} of oxygen in the interior annually. The aim of this chapter is to quantify the time-varying flux due to this lateral exchange with the boundary current, F_{lat}, for oxygen, carbon, and nitrate, in the upper ocean for the spring bloom period from May to the end of September 2016. This work will be part of a study aimed at estimating the effect of biological production, F_{bio} on these properties.

2.2 Data

Data used in this study come from the Seacycler mooring in the central Labrador Sea, Argo floats, North Atlantic Regional Reanalysis atmospheric data (*Mesinger et al.*, 2006), ship-based bottle data, and underway pCO_2 measurements. The Seacycler mooring includes a profiling component, which provides data with high vertical resolution approximately every 20 hours (*Send et al.*, 2013). The sensor float was equipped with an array of sensors, including pressure, temperature, salinity, carbon, oxygen, and nitrate measurements, described in more detail in *Atamanchuk et al.* (2020). In this study, pCO_2 measurements were converted to dissolved inorganic carbon (DIC) using the CO2SYS toolbox (*Lewis et al.*, 1998; *Van Heuven et al.*, 2011) and alkalinity calculated from temperature and salinity values using a climatological relationship. All Argo float data were downloaded from http://www.coriolis.eu.org/. For data from the core program (temperature and salinity), profiles for the entire Labrador Sea were used, totaling 67638 profiles from 272 floats. These temperature and salinity data were used to construct time-mean fields on a $0.25^\circ \times 0.25^\circ$ grid (see Figure 2.1), and time series in the central Labrador Sea and the boundary current. The central Labrador Sea was defined as profiles within 150 km of the Seacycler mooring. For the boundary current, profiles are used from the region between 60°N and 64.5°N where the mean salinity at the surface is less than 34, corresponding to the main eddy formation region (*Eden and Böning*, 2002). The location of the profiles is shown in Figure 2.1. Data from five floats were used for oxygen measurements in the boundary current, with profiles taken from the region between 60°N and 64.5°N with mean surface salinity between 33 and 34.25. This includes a slightly broader area than the temperature and salinity measurements (see Figure 2.1), which was necessary to obtain a sufficient number of profiles. Only one float equipped with a nitrate sensor spent a significant amount of time in the boundary current, which was used for the nitrate time series.

High-frequency data of pCO_2 made from a commercial vessel along shipping routes

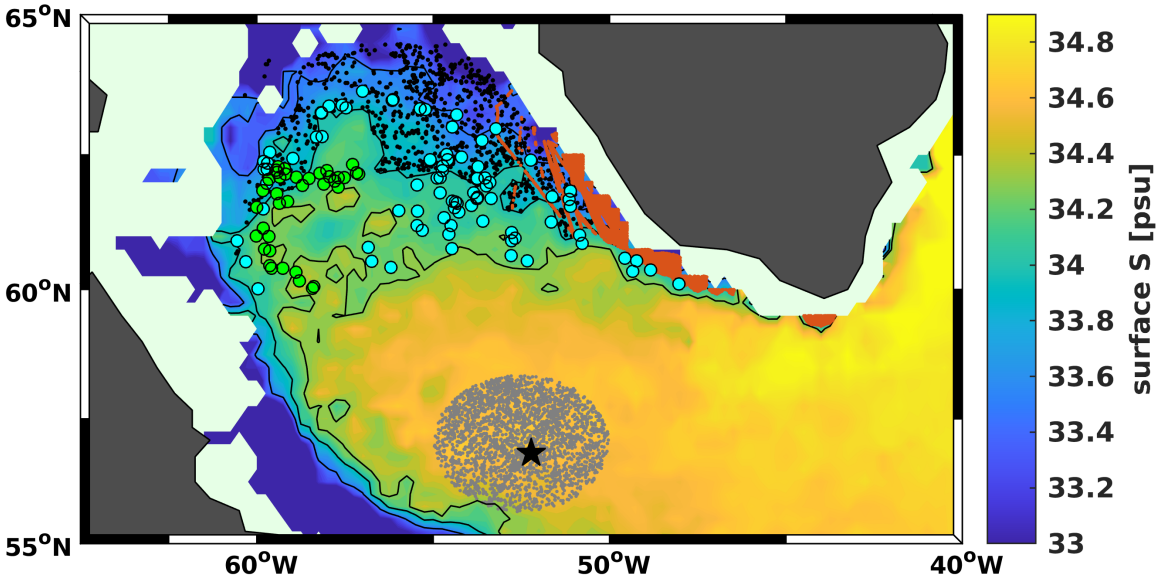

Figure 2.1: Mean salinity at the surface, and location of data used for the calculations. Gray and black dots show Argo T/S data used for the central Labrador Sea and boundary current, respectively. The Seacycler mooring is shown as a black star. Boundary current measurements from biogeochemical Argo floats are shown in green for nitrate, and in light blue for oxygen. Red dots show the locations of surface pCO_2 measurements.

between Denmark and western Greenland, the Nuka Arctica (*Olsen et al.*, 2008), were downloaded from http://nuka.uib.no/. The data are corrected to 2016 values of $p\mathrm{CO}_2$ using a linear fit to atmospheric values collected in Iceland, downloaded from https://www.esrl.noaa.gov/. After applying this correction, the data are used to construct a mean annual cycle at the surface, which is combined with the mean annual cycle of T and S from Argo floats and a climatological relationship for alkalinity to calculate DIC using the CO2SYS toolbox (*Lewis et al.*, 1998; *Van Heuven et al.*, 2011). Since no depth-resolved time series of carbon are available in this region, the data below the surface are estimated based on salinity data: First, a climatological salinity-DIC relationship is established by a linear fit to bottle measurements taken on the AR7W line in the boundary current region, which were downloaded from http://cchdo.ucsd.edu. This relationship is used along with float salinity data to calculate a time series of DIC at a depth of 150 dbar. For each time step, the surface DIC data from Nuka Arctica and this deep endpoint are used to fit another

linear relationship between DIC and salinity. The depth-varying salinity data are then used with this relationship to calculate the full vertical profile of DIC data.

2.3 Methods

The calculation of fluxes in this study is based on a budget approach, where changes in the inventory of a specific quantity are measured, and other fluxes are estimated, in order to solve for one of the terms. Budgets are constructed for the central Labrador Sea, based on data from the Seacycler mooring and Argo floats. The budget for any property studied here can be written as

$$\int_{z_1}^{z_2} \Pi(z,t_n) - \int_{z_1}^{z_2} \Pi(z,t_{n-1}) = \big(F(\Pi)_{\text{atm}} + F(\Pi)_{\text{lat}} + F(\Pi)_{\text{ent}} + F(\Pi)_{\text{bio}}\big)\Delta t, \tag{2.1}$$

where Π is the quantity of interest, z_1 and z_2 are the upper and lower bounds of integration, and t_1 and t_2 are consecutive time steps. F_{atm}, F_{lat}, F_{ent}, and F_{bio} refer to atmospheric flux, lateral flux, (vertical) entrainment flux and biological flux, respectively. Entrainment occurs primarily due to mixed layer deepening (*Martz et al.*, 2009). The budgets in this chapter are calculated for depth ranges that either always include the mixed layer, or are entirely below the deepest mixed layer in the study period, and F_{ent} is assumed to be zero. Salinity and temperature are not affected by biology, so $F(S)_{\text{bio}} = F(T)_{\text{bio}} = 0$, and nitrate is not affected by exchange with the atmosphere, $F(\text{NO}_3)_{\text{atm}} = 0$. F_{atm} for all other quantities is either measured or derived from NARR reanalysis data: For salinity, F_{atm} is calculated from the salinity change resulting from net precipation. For temperature, F_{atm} corresponds to the surface heat flux, and the budget is constructed for heat content Q, given by $Q = \rho c_p T$, where ρ is density, and c_p is the specific heat capacity of seawater, 3850 $J\ (kg\ ^\circ C)^{-1}$. For carbon and oxygen, gas exchange is calculated from the *Stanley et al.* (2009) parameterization; see Chapter 1 for details and a discussion of different parameterizations that are commonly used. Thus, all quantities in the budget except for

F_{bio} and F_{lat} can be resolved by the available measurements. F_{lat} is estimated as

$$F_{\text{lat}}(t_n) = \alpha\Big(\int_{z_1}^{z_2} \Pi_{\text{bnd}}(z, t_{n-1}) - \int_{z_1}^{z_2} \Pi_{\text{int}}(z, t_{n-1})\Big) \tag{2.2}$$

i.e. a fraction α of boundary current water being mixed into the interior. For temperature and salinity, where F_{bio} is zero, equations 2.1 and 2.2 can be used together to solve for α. This fraction is then used to estimate F_{lat} for the biogeochemical quantitites, and subsequently solve equation 2.1 for F_{bio}.

2.3.1 Error estimates

To obtain the most robust estimate of the fraction α of boundary current water mixed into the interior, α is calculated based on the mean annual cycle of temperature and salinity from all available data. The error is taken as the standard error for the fraction calculated from individual years. The error for biogeochemical measurements is based on the instrumental error, and for DIC also includes the error associated with the conversion from $p\text{CO}_2$ to DIC. The error for boundary current measurements of DIC is assumed to be twice that of the Seacycler mooring due to the uncertainty associated with estimating the profile of DIC based on salinity. The errors for the lateral fluxes are then given by error propagation of the error in α and in the gradients of each property.

2.3.2 Limitations

Due to the paucity of data in the region, particularly for nitrate and carbon, the data used for the region near Greenland come from different parts of the boundary current (see Figure 2.1), and for the most part were collected downstream of the location of maximum eddy kinetic energy (*Eden and Böning*, 2002), which may result in some errors in the estimated gradients. For example, oxygen data come from a region with statistically significant different salinity from that

used for calculating α. Furthermore, the data are averaged over several years in order to obtain a complete record of seasonal variability during the summer months. As a result, the estimate of the lateral flux of these properties can only be thought of as a mean seasonal cycle, assuming negligible interannual variability. Recently, the OSNAP array (*Lozier et al.*, 2017) has started to add oxygen and carbon sensors to their moorings in the boundary current near Greenland, so that a more accurate estimation of these fluxes may become possible in the future.

Another possible issue is the assumption that F_{ent} is zero. This simplifying assumption is necessary so that there is only one unknown in the budget equation, allowing us to solve for F_{lat}. However, there may still be a non-zero flux through the bottom of the mixed layer, and this will likely introduce an error, particularly for the budget including the mixed layer.

2.4 Determining the rate of lateral exchange

The fraction of boundary current water mixed into the interior Labrador Sea, α, is calculated for two different depth ranges from temperature and salinity, resulting in a total of four estimates: For 0-100 dbar, using NARR surface fluxes for F_{atm}, and for 200-1500 dbar, where $F_{\text{atm}} = 0$. The depth ranges are chosen because the transition between cold and fresh water from the West Greenland Current and warm and salty Irminger Current water typically occurs between 100m and 200m for eddies shed in this region (*Hátún et al.*, 2007). This is also supported by the mean profiles of the data used in this study, shown in Figure 2.2. The gradient of temperature switches sign at about 100 dbar, and again at 1500 dbar. For salinity, the boundary current is fresher than the interior at depths shallower than 200 dbar. Despite being calculated for different layers, the estimates for α are assumed to be representative of the whole water column, as eddies shed in the boundary current typically reach down to about 1500 m (*de Jong et al.*, 2014).

The estimates of α, expressed as a cumulative fraction, are shown in Figure 2.3. The estimate from mixed layer temperature (not shown) results in unrealistic values, giving a cu-

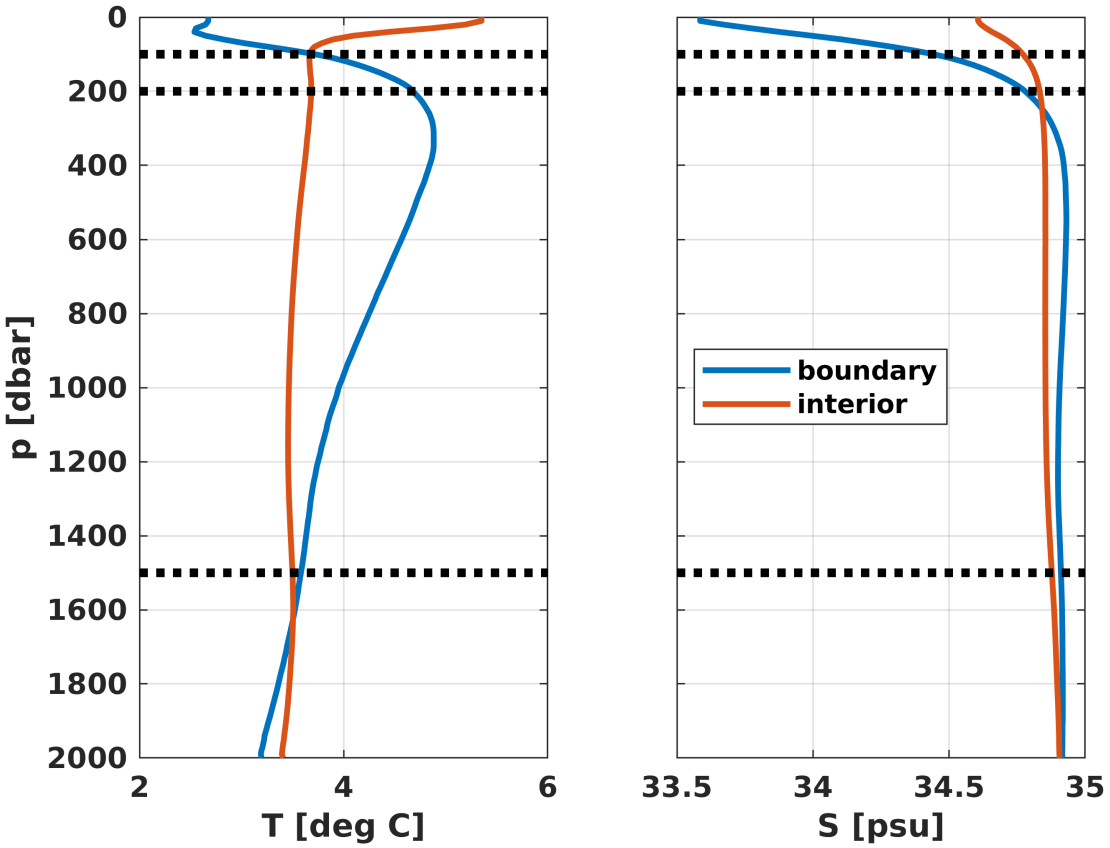

Figure 2.2: Mean temperature and salinity for all Argo profiles taken in the boundary (blue) and interior (red). See Figure 2.1 for positions of profiles.

mulative fraction of more than 1 for the summer, implying that the entire volume of water in the interior Labrador Sea would be replaced. This is likely due to the uncertainty in surface heat fluxes in the region, which has been noted previously (*Yashayaev and Loder*, 2009). The three other methods give comparable results, with a mean cumulative fraction of 0.13 between mid-May and the end of September. Using an area of 1.96×10^{11} m^2 for the central Labrador Sea, equivalent to a circle with 250 km radius, and a depth of 1500 m, this corresponds to a transport of about 3.3 Sv into the interior. This is comparable to estimates of Labrador Sea Water export based on a "disappearance volume" of 3.2 Sv to 8.9 Sv depending on the strength of convection (*Yashayaev and Loder*, 2016). Most of the mixing happens in June and July, consistent with

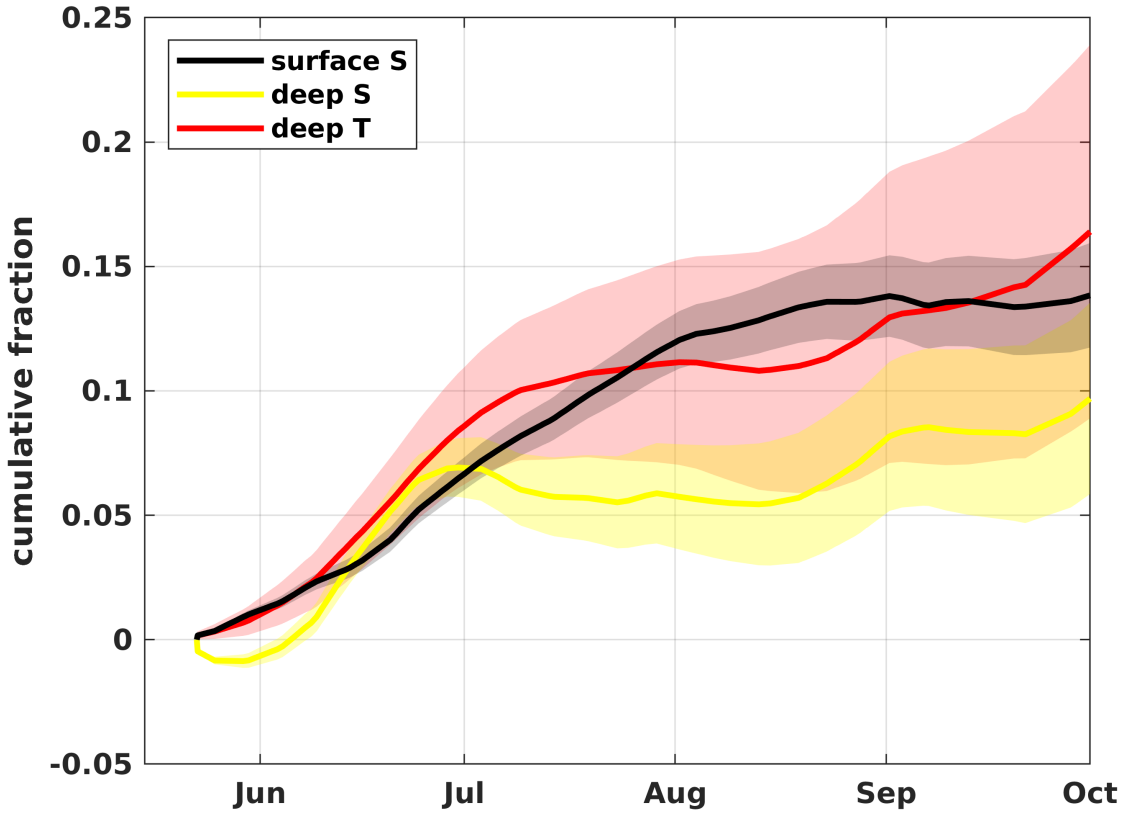

Figure 2.3: Cumulative fraction of water mixed into the interior from the boundary current for temperature and salinity for 0-100m and 100-1500m. Error bars are based on the standard error of the fraction estimated for individual years, as discussed in section 2.3.1.

results from *Schmidt and Send* (2007), who found that the main input of freshwater into the central Labrador Sea from the boundary current occurs in these months. The good agreement between budgets for the surface and deep ocean supports the assumption that the lateral exchange is largely achieved by exchange of eddies with a fresh near-surface layer originating from the West Greenland Current, and warmer, saltier Irminger Current water below (*Hátún et al.*, 2007; *de Jong et al.*, 2014), as opposed to a mostly wind-driven exchange of surface waters (*Schulze Chretien and Frajka-Williams*, 2018).

2.5 Budgets of carbon, oxygen, and nitrate

Below, we calculate the budgets for two layers: 0–55 dbar, and 55–145 dbar. The layers are chosen so that the deeper layer is entirely below the deepest mixed layers found during this time, and air-sea exchange can be assumed to affect only the surface layer. The focus of this study is on the productive season in summer, so budgets are calculated from mid-May to the end of September, which marks the onset of rapid mixed layer deepening.

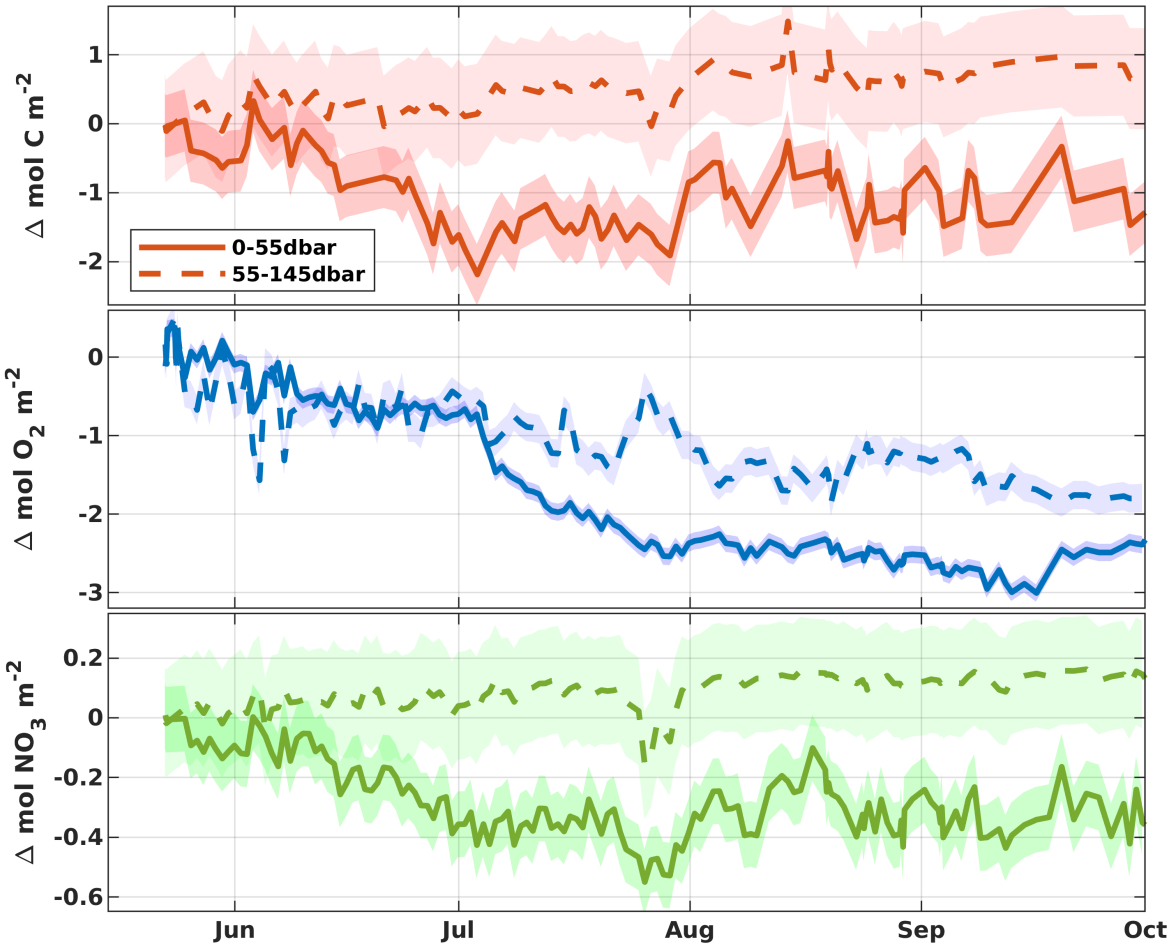

Figure 2.4: Inventories of dissolved inorganic carbon (DIC), oxygen, and nitrate for the 0–55 dbar and 55–145 dbar layers measured by the Seacycler mooring. Shading represents the measurement error.

The inventories for the three properties are shown in Figure 2.4 for both layers. During this time, nitrate, oxygen, and DIC concentrations in the upper ocean are all decreasing. The decrease of nitrate and DIC is likely related to biological activity, as phytoplankton production uses up nutrients and carbon. For oxygen, production from the blooms and solubility changes due to surface warming maintain supersaturation in the mixed layer throughout the study period (not shown). This results in strong gas exchange, which offsets the biological production and dominates the budget in the mixed layer. Below the mixed layer, carbon and nitrate increase, and oxygen decreases, consistent with a budget controlled mostly by biologically mediated changes.

F_{lat} for the two layers is calculated from equation 2.2, using α determined from surface salinities in section 2.4. The property gradient is calculated from Seacycler data (see Figure 2.4) and the boundary current data described in section 2.2. The resulting cumulative fluxes are shown in Figure 2.5 for the two layers. The lateral flux is lowest for oxygen, where it is almost zero below the mixed layer, and about 9% of the inventory change over the same time period near the surface. For carbon and nitrate, fluxes in the mixed layer are somewhat larger, but still only make up 10% and 7.5%, respectively, of the inventory change. The change in the deeper layer is much more significant for the budget, with a magnitude of 40% of the inventory change for carbon, and 33% for nitrate (compare Figure 2.4).

Using the lateral flux calculated for the three biogeochemical properties, equation 2.1 can be solved for the flux due to biological activity, F_{bio}. The results are shown in Figure 2.6, expressed as moles of carbon, with nitrate and oxygen values converted using ratios of 106:16 for C:N (*Redfield*, 1934) and -1.34 for O_2:C (*Körtzinger et al.*, 2001). In the surface layer, all three measurements show a biological carbon drawdown between the beginning of the record and early July, indicating intense biological activity. The peak cumulative biological flux occurs on July 3^{rd}, and is measured from the three different instruments as -2.45 ± 0.49 mol C m^{-2}, -0.40 ± 0.11 mol N m^{-2} ($= -2.63 \pm 0.76$ mol C m^{-2}), and $+2.24 \pm 0.11$ mol O_2 m^{-2} ($= -1.67 \pm 0.08$ mol C m^{-2}). The large errors for the nitrate and carbon measurements reflect

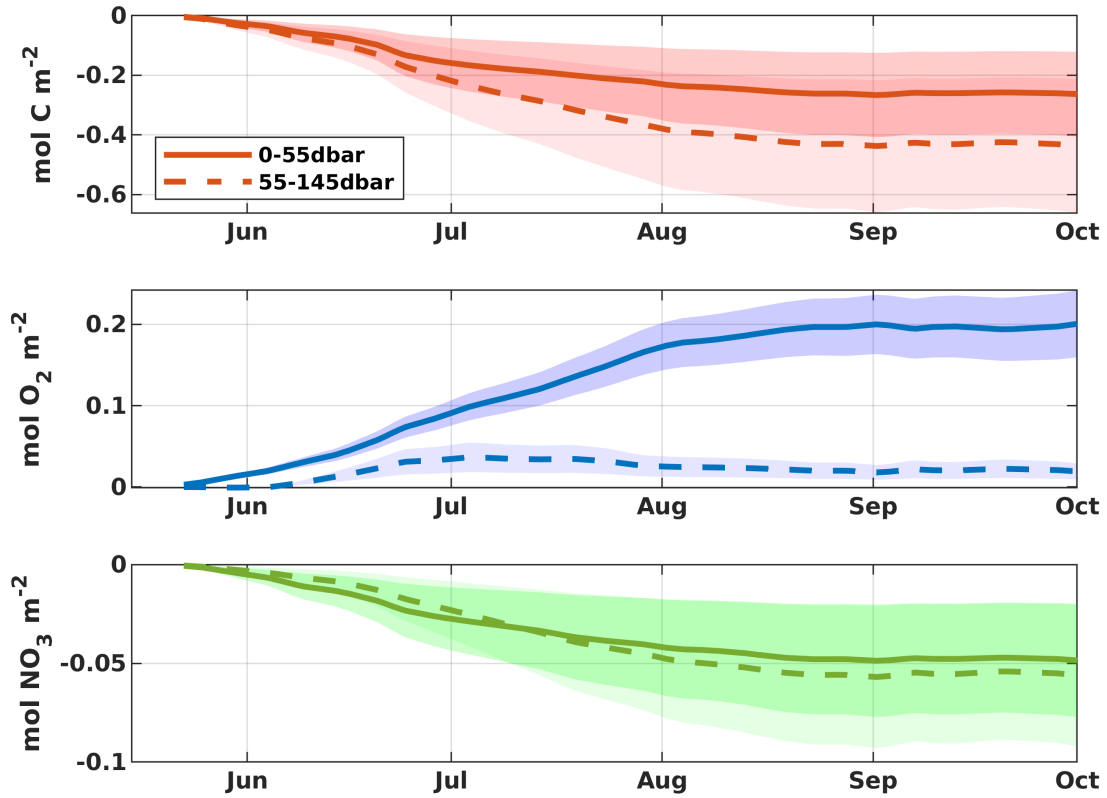

Figure 2.5: Cumulative lateral flux for carbon, oxygen, and nitrate from the boundary current region into the interior Labrador Sea. Errors are estimated based on the measurement error, and the error in the volume flux shown in figure 2.3.

largely the measurement error associated with the less developed sensor technology, highlighting the utility of measuring multiple parameters for more robust estimates. While the nominal error is smaller for oxygen, the flux is sensitive to the parameterization used for air-sea gas exchange (not shown; see *Koelling et al.* (2017) and *Atamanchuk et al.* (2020) for a discussion), which may explain the lower peak values. The Seacycler mooring was deployed after the average start date of the phytoplankton bloom, which usually occurs some time in April (*Frajka-Williams and Rhines*, 2010). As a result, the flux of about -2.5 mol C m^{-2} calculated here is likely an underestimate of the total biologically mediated flux. A simple estimate is made for the biological flux before this time by comparing the last measurements in March 2017 to the first mooring

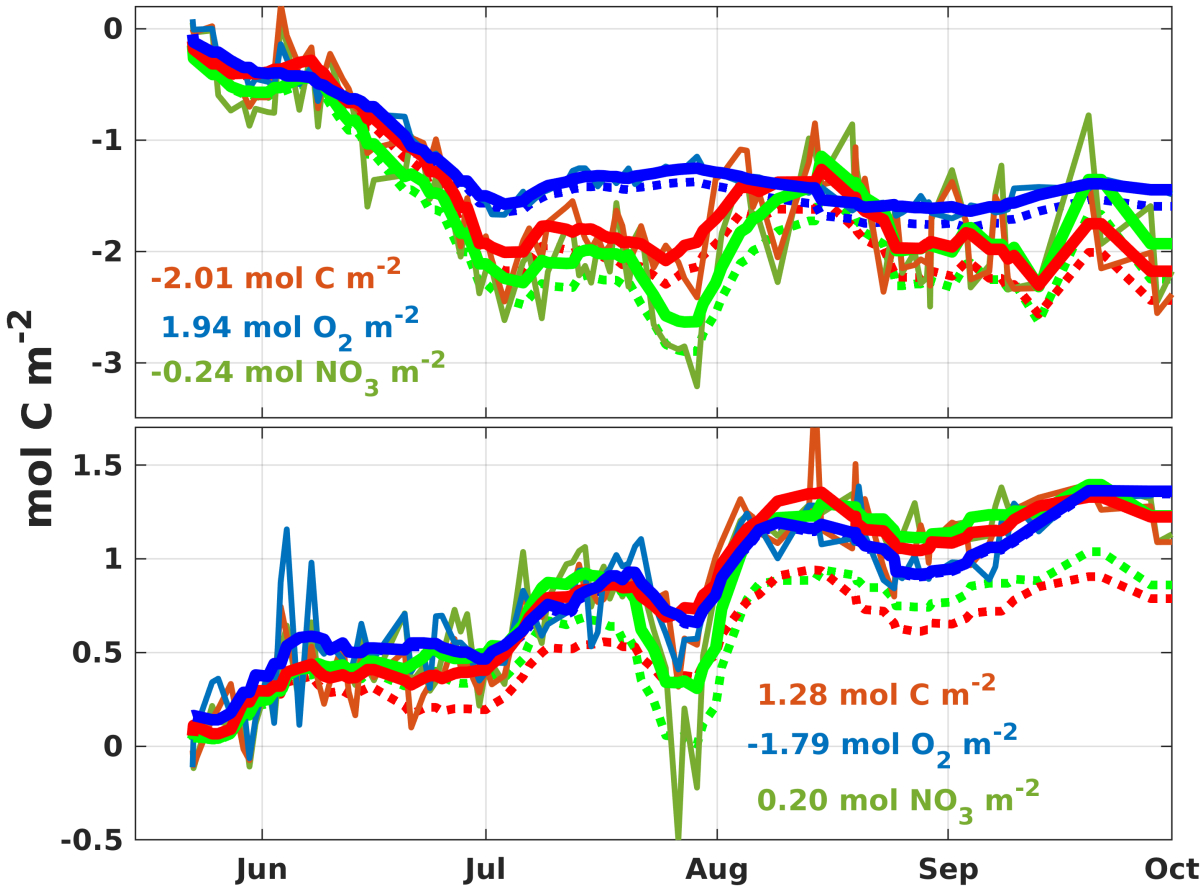

Figure 2.6: Cumulative biological flux for carbon, oxygen, and nitrate; 0–55 dbar (top), and 55–145 dbar (bottom). Thick lines are 10-day running means, and dotted lines show estimates without correction for the lateral flux. Values are expressed as moles of carbon using climatological values for conversion (see text for details). Error estimates are ommitted from the figure for clarity, but are reported in the text.

profile, assuming mean air-sea and lateral fluxes and neglecting interannual variability. This gives a range of estimates of -1.19 mol C m^{-2} to -2.02 mol C m^{-2} from the oxygen, carbon and nitrate measurements for the flux prior to the start of the mooring deployment. Using this crude estimate along with the values from nitrate and carbon measurements shown in Figure 2.6, the total Net Community Production (NCP) flux is between -3.64 mol C m^{-2} and -4.65 mol C m^{-2}, comparable to a value of 4.0 mol C m^{-2} reported by *Körtzinger et al.* (2008) for an earlier mooring data set in the same location. After the peak in July, values stay relatively constant, suggesting that there is little remineralization occuring within the mixed layer, as was also observed in earlier

studies (*Körtzinger et al.*, 2008; *Martz et al.*, 2009). There is another minimum in late July, but this appears to be related to an eddy, which can also be seen by dips in inventories in Figure 2.4. As discussed above, the lateral flux in this layer is much smaller than the inventory change, so ommitting it only leads to a small overestimation of the peak biological flux associated with the spring bloom, on the order of 5%.

Below the mixed layer, the lateral flux contributes more strongly to the budget for nitrate and carbon, while it is almost zero for oxygen (Figure 2.5). The cumulative flux until September 28^{th}, the time of the last profile with a mixed layer shallower than 55 dbar, is 1.28 ± 0.76 mol C m^{-2} for carbon, 1.34 ± 0.13 mol C m^{-2} calculated from oxygen, and 1.33 ± 1.22 mol C m^{-2} calculated from nitrate. Without the correction for F_{lat}, the C and N fluxes are still similar, but would only be 0.85 ± 0.73 mol C m^{-2} from carbon, and 0.96 ± 1.19 mol C m^{-2} from nitrate, while the flux calculated from oxygen remains almost unchanged at 1.32 ± 0.13 mol C m^{-2}. The inclusion of the lateral flux therefore makes the results more consistent with Redfield stoichiometry. This is an indication that the estimate of lateral exchange used in this study, despite the limitations outlined in section 2.3.2, is realistic.

With the exception of a dip in late July, which is associated with the aforementioned eddy passing through, the low-pass filtered cumulative flux is continuously increasing, which is indicative of respiration of organic matter. Periods of stronger respiration seem to alternate with periods of relatively little change, with the strongest increase in the cumulative flux between the beginning of the record and early June, and early July and mid-August. The second of these periods occurs immediately after the bloom seen in the surface layer ends, and may thus be related to the respiration of organic material sinking out of the mixed layer after the bloom. Likewise, the initial increase starting in mid-May could represent respiration of organic matter from the earlier bloom that occurred prior to the start of the record.

The remineralization of carbon below the mixed layer before July is equivalent to about 27%-35% of the carbon produced in the mixed layer during the bloom, using the estimate of

activity prior to the start of the mooring deployment. This is similar to a previous estimate for the entire water column above the depth of the winter mixed layer ($>$ 1000 m) for a full annual cycle (*Körtzinger et al.*, 2008), which they attributed to the remaining carbon being exported below the depth of convection. Our results suggest that the respiration rate for the time span and depth range used by *Körtzinger et al.* (2008) is likely higher than they reported, and was underestimated because they neglected the lateral flux. Consequently, the real export of carbon below the winter mixed layer would be lower than reported in their study.

2.6 Summary

In this chapter, I derived the lateral flux of water from the boundary current into the interior of the Labrador Sea. Rates of exchange calculated from temperature and salinity for the 0-100 dbar and 200-1500 dbar depth ranges were consistent, with the exception of those from surface temperature. The good agreement between the methods suggets that the transport of boundary current water into the interior is associated with deep-reaching eddies. The cumulative exchange between mid-May and the end of September corresponds to a fraction of 0.13 of boundary current water entering the interior, equivalent to a transport of about 3.3 Sv.

The rate of exchange was used to infer lateral fluxes for carbon, oxygen, and nitrate, with the goal of improving estimates of biological activity, F_{bio}. Accounting for F_{lat} increases the estimates of respiration rates below the mixed layer by 39% for nitrate and 51% for carbon, as the associated loss of carbon and nitrate would otherwise be erroneously attributed to weaker respiration. The correction for lateral fluxes substantially improves the agreement between estimates from carbon and nitrate with the estimate from oxygen when using Redfield stoichiometry. The results suggest that a previous study looking at carbon and oxygen budgets in the Labrador Sea may have overestimated the export of carbon below the winter mixed layer due to ignoring the effect of F_{lat}. This shows that lateral fluxes can still be important for biogeochemical budgets

even in regions like the Labrador Sea with relatively weak mean flow, and need to be accounted for to accurately represent the carbon, oxygen, and nitrate cycles.

2.7 Acknowledgments

JK was supported by NASA Headquarters under the NASA Earth and Space Science Fellowship Program (Grant NNX16AO39H), and by an Ocean Frontier Institute Visiting International Research Fellowship. Canadian support was via the Canada Excellence Research Chair in Ocean Science and Technology and the NSERC-supported VITALS (Ventilation, Interactions and Transport Across the Labrador Sea) project. Argo data were collected and made freely available by the International Argo Program and the national programs that contribute to it (http://www.argo.ucsd.edu, http://argo.jcommops.org). The Argo Program is part of the Global Ocean Observing System.

Chapter 2, in full, is being prepared for submission for publication of the material. Koelling, J.; Atamanchuk, D.; Wallace D.W.R.; Send, U. The dissertation author was the primary investigator and author of this material.

Chapter 3

Decadal strengthening of interior flow of North Atlantic Deep Water observed by GRACE satellites

This chapter has been submitted as Koelling, J., U. Send, and M. Lankhorst (2020), Decadal strengthening of interior flow of North Atlantic Deep Water observed by GRACE satellites, *submitted to Journal of Geophysical Research: Oceans*.

Abstract

The Gravity Recovery and Climate Experiment (GRACE) satellite mission provides information on changes to the Earth's gravity field, including ocean mass. Long-term trends in GRACE ocean mass data are often considered unreliable due to uncertainties in the corrections made to calculate ocean mass from the raw measurements. Here, we use an independent estimate of ocean mass from satellite altimetry and *in situ* density data from five mooring sites and repeat hydrography to validate trends in GRACE over the North Atlantic, finding substantial agreement between the methods. The root mean square difference between ocean mass changes calculated

with this method from the mooring data and those measured by GRACE is 3.5 mm/decade, much lower than the mean signal of 15.6 ± 1.8 mm/decade for GRACE and 17.8 ± 4.0 mm/decade for the altimetry-mooring estimate.zz The GRACE ocean mass data are then used to study the change in the deep circulation of the North Atlantic between the 2002/04/01-2009/03/31 and 2010/04/01-2017/03/31 periods, revealing a large-scale anticyclonic circulation anomaly off the North American coast. The change is associated with an increase of 13.9 ± 3.7 Sv ($1\text{Sv} = 10^6$ m^3 s^{-1}) of southward North Atlantic Deep Water flow in the interior between 30°N and 40°N, largely balanced by a northward anomaly of 10.7 ± 3.7 Sv for the Deep Western Boundary Current. This implies an increased importance of interior pathways compared to the Deep Western Boundary Current for the spreading of North Atlantic Deep Water, which constitutes the lower limb of the Atlantic Meridional Overturning Circulation.

3.1 Introduction

The Gravity Recovery and Climate Experiment, or GRACE, satellite mission was launched in 2002 (*Tapley et al.*, 2004), and collected an approximately 15-year long record of variability in the Earth's gravity field before it was decomissioned in late 2017. The follow-on mission, GRACE-FO, was launched in May 2018. The GRACE setup consists of twin satellites orbiting the Earth in sequence and measuring the distance between one another using radar. Changes in the Earth's gravity field accelerate or slow down each of the satellites as they pass above them, so that gravity anomalies can be inferred from the distance measurements. Gravity changes over the ocean provide information on ocean mass variability, which is used for studies of the global sea level budget (*Leuliette and Miller*, 2009; *Chambers et al.*, 2017) and deep ocean circulation (*Landerer et al.*, 2015; *Mazloff and Boening*, 2016). Early GRACE products suffered from spurious "leakage" of the much larger terrestrial signal into the ocean, particularly near the coasts (*Guo et al.*, 2010). Several gridded products developed since then address this issue by separating

the global grid into spherical cap mass concentrations, or mascons, which better differentiate between land and ocean. Nonetheless, uncertainties remain as large signals unrelated to oceanic variability, such as glacial isostatic adjustment or the Earth's pole tide, need to be corrected to obtain the final GRACE solution, and errors in estimating these quantities can propagate into the gridded GRACE data. These geological processes occur on time scales far exceeding the length of the GRACE record, such that they would manifest themselves as a trend in the ocean mass data. As a result, a linear trend is often removed from GRACE data before using them in transport calculations (*Landerer et al.*, 2015; *Worthington et al.*, 2019). However, since changes in ocean mass or, equivalently, bottom pressure, are related to geostrophic flow, the signal on these time scales is of great interest for studies of the deep circulation. This is true particularly in the Atlantic Ocean, where they are associated with variability in the lower branch of the Atlantic Meridional Overturning Circulation (AMOC), which plays an important role in the Earth's climate (*Srokosz and Bryden*, 2015). Decadal variability and long-term trends in AMOC strength have been shown to exist in both observations and climate models (*Send et al.*, 2011; *Smeed et al.*, 2014; *Danabasoglu*, 2008; *Muir and Fedorov*, 2017), and the much better spatial coverage of GRACE compared to traditional measurements in the deep ocean could provide new insights into variability of the deep circulation. In the North Atlantic Ocean, the decadal signal in GRACE appears to exhibit large-scale patterns of ocean mass increase which are intensified in the interior western basin (Figure 3.1), resembling patterns associated with the distribution of North Atlantic Deep Water (*Rhein et al.*, 2015). This study is motivated by the question of whether or not these changes reflect real oceanic variability.

Although continuous time series of *in situ* ocean bottom pressure for comparison to GRACE do exist, bottom pressure recorders suffer from a drift that cannot be separated from real variability on time scales longer than a few years (*Watts and Kontoyiannis*, 1990), rendering them unsuitable for validating trends in GRACE. An alternative method of inferring variability in ocean mass is to calculate it as the difference between sea level anomalies and changes in steric

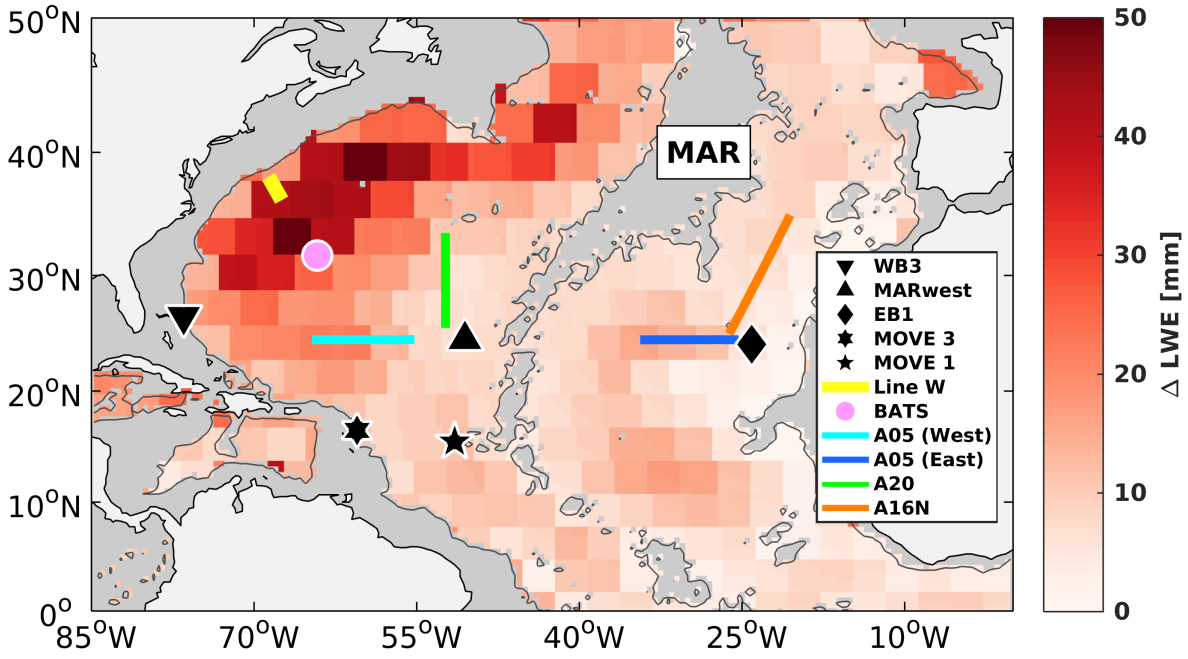

Figure 3.1: Ocean mass change in the GRACE JPL RL05.1M product, calculated as the mean from 2010/04/01 to 2017/03/31 minus the mean from 2010/04/01 to 2017/03/31. Data are only shown at grid points with depth exceeding 3500 m, and expressed as liquid water equivalent (LWE). Black symbols denote mooring sites, and other symbols/lines show repeat hydrography stations and sections used in this study. Shading shows the 3500 m isobath. MAR = Mid-Atlantic Ridge

height, the latter being caused by the expansion or contraction of the water column due to density changes. An analysis of hydrographic data by *Purkey et al.* (2014) showed that global ocean mass trends calculated with this method agreed well with an earlier release of GRACE data, and regional trends averaged over entire ocean basins were generally consistent with GRACE, too. To date, this method has not been employed on smaller spatial scales due to the temporal and spatial sparsity of ocean density data, which results in small-scale noise being aliased into the larger-scale signal of interest. However, a model simulation by *Williams et al.* (2015) showed that, using thorough calibration procedures for mooring data, sufficient accuracy can be achieved to detect decadal trends from moorings and satellite altimetry. Carefully calibrated mooring arrays have been deployed as part of the MOVE project at 16°N since 2000 (*Send et al.*, 2011),

and the RAPID project at 26.5°N since 2004 (*McCarthy et al.*, 2015). Here, we use data from these moorings, along with hydrographic time series and transects, to validate decadal trends in GRACE (Figure 3.1), and subsequently use these GRACE data to investigate the corresponding changes to the deep circulation of the Atlantic Ocean.

3.2 Methods and Data

3.2.1 Data

Both MOVE and RAPID moored Conductivity-Temperature-Depth (CTD) data are calibrated before and after each deployment by attaching each sensor to a ship-based rosette with CTD sensor and comparing measurements during a number of subsurface stops to data from the rosette CTD, which in turn is calibrated against bottle samples. The resulting accuracy of the practical salinity, temperature, and pressure measurements is 0.002, 0.001°C, and 2 dbar relative to the rosette CTD (*Kanzow et al.*, 2006). For the MOVE moorings, anomalies of temperature and salinity from climatology are interpolated vertically between sensors, and constant anomalies are extrapolated to 80 m from the next deepest instrument. This produces a dataset on a consistent vertical grid. The depth of 80 m was chosen because it represents the approximate maximum depth of the mixed layer in winter, and sensor coverage above this depth varied between deployments. MOVE 1 was deployed in a different configuration between 2007 and 2011, with no instruments in the upper 1000 m of the water column, resulting in a data gap of approximately 4 years in the steric height data used here. Data from the RAPID *EB1* mooring are processed the same way, with data from each instrument obtained from https://www.bodc.ac.uk/. For the RAPID *WB3* and *MARwest* moorings, temperature (T) and salinity (S) data used are taken from the pressure-gridded fields available on the project website, http://www.rapid.ac.uk/ (*Smeed et al.*, 2019). These extend from the seafloor to about 150 m throughout the deployments. The procedure for interpolation between instruments is similar to that used at MOVE, and is described in more

Table 3.1: Access information for data used in this study

Site	website	data version
RAPID WB3, MARwest	http://rapid.ac.uk	
RAPID EB1	http://bodc.ac.uk	
MOVE 3, MOVE 1	ftp://data.ndbc.noaa.gov/data/oceansites/DATA/	
A05, A20, A16N, BATS	http://cchdo.ucsd.edu	
Line W	http://scienceweb.whoi.edu/linew	
GRACE	http://grace.jpl.nasa.gov	JPL RL05.1M
Altimetry	http://aviso.altimetry.fr [1]	dt_global_twosat_madt

detail by *McCarthy et al.* (2015).

For all mooring data, the steric height measurements used in this study are extrapolated above the shallowest measurement by a linear fit to steric height anomalies over the 75 m below for each time step, based on the method described by *McCarthy et al.* (2015). Shipboard data from the Bermuda Atlantic Time Series (BATS), Line W, and hydrographic transects A05, A20, and 16N are also used. The data sources for all data used in this study are listed in Table 3.1, and the times and locations of measurements used are given in Table 3.2.

For altimetry data, a daily gridded product is used, linearly interpolated to the location of the respective density measurements, and 10-day averages are used for shipboard data. GRACE data come from the JPL RL05.1M product, the development of which was motivated in part by a desire to improve the representation of gravity anomalies over the ocean (*Watkins et al.*, 2015). The method involves separating the Earth into 4551 equal-area mass concentration cells, called mascons, with an area equivalent to $3^\circ \times 3^\circ$ at the equator, and integrating the gravitational potential over the surface of each mascon. Thus, while the grid spacing of the data product is $0.5^\circ \times 0.5^\circ$, the effective resolution is about $3^\circ \times 3^\circ$. The usage of the mascons eliminates much of the spurious north-south "stripe" signal found in earlier spherical harmonic solutions (*Watkins et al.*, 2015; *Save et al.*, 2016) and improves the separation between gravity signals in the ocean and on land. For details on the mascon method, and its advantages over previous GRACE products, the reader is referred to *Watkins et al.* (2015). The GRACE data are corrected for errors

[0](now available at marine.copernicus.eu)

in the pole tide model following *Wahr et al.* (2015). Data used for each site are taken from the nearest gridpoint. BATS lies on the boundary between two GRACE mascons, one encompassing much of the shallow ocean around Bermuda, and one situated largely in the deep ocean, with the latter chosen for the analysis here.

3.2.2 Sea Level Budget

Sea level anomaly relative to a reference time measured by satellite altimetry, SL'_{alt}, can be expressed as the sum of two components, one due to expansion or contraction of the water column as a result of density changes, SL'_{steric}, and one due to addition or subtraction of mass, SL'_{mass}. In this study, we use mooring- and hydrography-based measurements of T and S to calculate SL'_{steric} for the full water column and combine them with SL'_{alt} to obtain an estimate of SL'_{mass}:

$$SL'_{\text{mass}}(t) = SL'_{\text{alt}}(t) - SL'_{\text{steric}}(t), \tag{3.1}$$

where t is time. Steric height is computed as the vertical integral of the specific volume anomaly relative to seawater at a salinity of 35 and temperature of 0° C, δ, divided by the gravitational constant g (*Talley et al.*, 2011), $SL_{\text{steric}} = g^{-1} \int \delta dp$. Studies of global sea level rise have compared total sea level anomalies, SL'_{alt}, calculated from SL'_{steric} for the 0-2000 m depth range from Argo floats, and SL'_{mass} from GRACE, to sea level records from tide gauges or altimetry in an attempt to close the global sea level budget (e.g. *Leuliette and Miller*, 2009; *Chambers et al.*, 2017). Here, SL'_{steric} is computed for the majority of the water column, with the deepest measurement available throughout the record chosen as the reference depth at each site.

We calculate the ocean mass trend in mm/decade as the difference between the average of SL'_{mass} (in mm) over two multiyear periods, T_1 and T_2, scaled by the time difference between the central time in each period, ΔT, in years:

$$\Delta SL_{\text{mass}} = \left(\overline{SL'_{\text{mass}}}^{T_2} - \overline{SL'_{\text{mass}}}^{T_1}\right)\frac{10}{\Delta T} \tag{3.2}$$

where overbars denote the time average. This is done for both ocean mass calculated from altimetry (A) and steric height from density data (S) using equation 3.1, SL'_{mass}(A&S), and the ocean mass data from GRACE, SL'_{mass}(G), and the resulting trends are compared in section 3.3.1.

For moorings and BATS hydrography data, the averages are taken over the first and second half of the record, calculated for an integer number of years. E.g. for the 13-year RAPID record, changes are calculated as the difference between the 2004/04/01-2010/03/31 and 2011/04/01-2017/03/31 periods. Line W was only occupied once or twice per year. To achieve a more robust estimate here, the trends between the first and second half of the record are averaged over eight stations, listed in Table 3.2 in section 3.3, and the mean of these stations is used in section 3.3.1. For other hydrographic transects, data come from only two occupations, and therefore short-term and small-scale variability can alias the long-term difference sought here. To mitigate this, the hydrography data are averaged over a relatively broad longitude or latitude range to reduce noise associated with variability on small spatial scales. The averaging for each transect includes about 10 to 20 stations, and the ranges are given in Table 3.2. For consistency, trends from GRACE are averaged over the same regions. In addition, $\overline{SL'_{\text{mass}}}^{T_n}$ is calculated as

$$\overline{SL'_{\text{mass}}}^{T_n}(\text{A\&S}) = SL'_{\text{mass}}(\text{A\&S})(t_n) - \left(SL_{\text{mass}}(\text{G})(t_n) - \overline{SL'_{\text{mass}}}^{T_n}(\text{G})\right), \tag{3.3}$$

where t_n denotes the time of the CTD occupation (see Table 3.2), and T_n is a multi-year period as in equation 3.2. $SL_{\text{mass}}(\text{G})(t_n)$ is averaged over 3 months centered on t_n, and $\overline{SL'_{\text{mass}}}^{T_n}(\text{G})$ is calculated for 2002/04/01-2009/03/31 and 2010/04/01-2017/03/31, for T_1 and T_2, respectively. This removes some of the high-frequency variability in $SL'_{\text{mass}}(\text{A\&S})(t_n)$ based on GRACE data, so that the resulting estimate $\Delta SL_{\text{mass}}(\text{A\&S})$ is more representative of the long term trend.

3.2.3 Geostrophic Transport

The change in horizontally averaged geostrophic flow between any two points at the same depth, z_1 as a function of pressure p, is given by

$$u'(z_1) = -\frac{1}{f\rho_0}\frac{\Delta p'(z_1)}{\Delta y}, v'(z_1) = \frac{1}{f\rho_0}\frac{\Delta p'(z_1)}{\Delta x}, \tag{3.4}$$

with ρ_0 and f being a typical seawater density and the Coriolis parameter, respectively, and primes denoting fluctuations relative to the time mean. Pressure at the sea floor can be inferred from GRACE ocean mass, which can thus be used to calculate the geostrophic flow at this depth. A vertical profile of geostrophic flow between two points can be inferred by combining this so-called reference level velocity with the vertical velocity shear, which is proportional to the horizontal density gradient. Changes in ocean transport can be separated into a barotropic, or depth-independent, component T'_{BT}, which is equal to the velocity from equation 3.4 multiplied by the horizontal distance and layer thickness, and a baroclinic component, T'_{BC} calculated from the velocity shear, with the total transport variability given by the sum of the two.

3.2.4 Error Sources

Instrumental Error

The accuracy of individual altimetry measurements of sea surface height is about 2.5 cm for modern altimeters (*Chelton et al.*, 2001), so the error for SSH averaged over a certain time period or region is given by

$$\sigma_{\mathrm{SSH}} = \frac{2.5\text{ cm}}{\sqrt{DOF_{\mathrm{SSH}}}}, \tag{3.5}$$

with DOF_{SSH} representing the degrees of freedom of the average. A typical repeat time of ground tracks is 10 days, and we consider consecutive measurements to be independent. While there may be biases in the mean geoid that lead to correlated errors between measurements, we

consider only the difference between two time periods here, which is not sensitive to accurate representation of the mean. The degrees of freedom for each averaging period at the mooring sites are thus given by the length of the period L, in days, divided by 10, $DOF_{\mathrm{SSH}} = L/10$. For CTD data from hydrographic transects used in Figure 3.2, we assume that SSH data at each station are independent, such that DOF_{SSH} is equal to the number of stations used in the averaging.

For mooring-based steric height estimates, the error comes principally from two sources: the calibration error of each instrument relative to the reference CTD in the calibration procedures described in *Kanzow et al.* (2006), σ_{inst}, and the accuracy of the reference CTD itself in measuring temperature, salinity, and pressure, σ_{CTD}. For σ_{inst}, we use a value of 4 mm, which was determined by *Williams et al.* (2015) to be the uncertainty in steric height due to uncorrelated calibration errors for individual instruments. The CTD error is calculated by considering separately the contributions of the measurement accuracy of 0.002 and 0.002° C on salinity and temperature (*IOCCP-ICPO*, 2010), and an error of 0.0015% of full scale, or about 1.02 dbar, for a typical pressure sensor (*Houston and Paros*, 1998). The combined error σ_{CTD} amounts to about 8.2 mm for a typical depth of 5000 m, and scales approximately linearly with depth. The error for the steric height in each of the two time periods T is then given by

$$\sigma_{\mathrm{steric}}(\mathrm{T}) = \sqrt{\frac{\sigma_{\mathrm{inst}}^2 + \sigma_{\mathrm{CTD}}^2}{DOF_{\mathrm{steric}}(\mathrm{T})}} \tag{3.6}$$

Measurements from the same mooring deployment cruise cannot be considered to be independent as they are calibrated against the same CTD data, such that the degrees of freedom $DOF_{\mathrm{steric}}(T)$ for each time period T are equal to the number of mooring deployments during this time. For estimates from single CTD sections, $\sigma_{\mathrm{inst}} = 0$, but the overall error is larger because they come from only one cruise, so that $DOF_{\mathrm{steric}}(T) = 1$. For moorings, there is also an error associated with the discrete sampling in the vertical (*Kanzow et al.*, 2006). This is typically about 1 cm for instantaneous steric height measurements (*Williams et al.*, 2015), but unlike σ_{inst} and σ_{CTD}, the error is not constant for each deployment. The degrees of freedom are therefore given by the

autocorrelation time scale of the measurement (*Leith*, 1973), with resulting errors in the trend on the order of 1 mm, which is negligible compared to σ_{inst} and σ_{CTD}.

Assuming errors are uncorrelated, the total error for the altimetry-steric estimate of ocean mass change, ΔSL_{mass}(A&S), is then

$$\sigma_{\Delta SL_{\text{mass}}(\text{A\&S})} = \sqrt{\sigma^2_{\text{steric}}(T_1) + \sigma^2_{\text{steric}}(T_2) + \sigma^2_{\text{SSH}}(T_1) + \sigma^2_{\text{SSH}}(T_2)} \tag{3.7}$$

The uncertainty in GRACE is calculated from a measurement error of 1 cm (*Watkins et al.*, 2015; *Landerer et al.*, 2015), and the degrees of freedom calculated from the length of the time series and the autocorrelation time scale following *Leith* (1973). Error bars in Figure 3.2 and uncertainties in Table 3.2 reflect the instrumental error discussed in this section.

Other Errors

In addition to the measurement error, biases in regional trends from satellite altimetry can be on the order of 2-3 mm/year due mostly to orbit errors (*Ablain et al.*, 2015), which is of comparable magnitude to the ocean mass trends shown in Figure 3.1. For GRACE, uncertainties in the removal of low-frequency signals that are not related to oceanic variability are also of the same order as the signal of interest (*Landerer et al.*, 2015), and the large averaging area of the GRACE mascons smoothes out some of the signal compared to the point measurements from moorings and higher-resolution data from altimetry. The magnitude of all of these errors will depend on the location, making them difficult to quantify, so they are not shown as part of the uncertainty in Figure 3.2 and Table 3.2. We note that the bias from corrections to altimetry or GRACE alone could feasibly be responsible for the entire trend at most sites. However, the good agreement between the two methods of calculating SL_{mass} and the spatial patterns in the trend (see below) suggests that this is not the case.

3.3 Ocean mass changes

Spatially variable decadal ocean mass changes are evident in the GRACE data in Figure 3.1, but previous studies have typically assumed the trends to be caused by uncertainties in the GRACE correction (*Landerer et al.*, 2015). In this section, we evaluate whether these changes are real signals in the ocean, or caused by errors in the GRACE product. We also compare spatial patterns of the trend to water mass properties, and investigate the contribution of different parts of the water column to steric height changes.

3.3.1 Validating decadal trends in GRACE

To validate the decadal ocean mass change seen in Figure 3.1, $\Delta SL'_{\text{mass}}$(A&S) is calculated as the difference between ΔSL_{alt} from altimetry and $\Delta SL_{\text{steric}}$ from moorings (equations 3.1 and 3.2). This estimate of the ocean mass trend is plotted against the trend over the same time period from the GRACE JPL RL05.1M product, ΔSL_{mass}(G), in black symbols in Figure 3.2, and both estimates are listed for all moorings in Table 3.2. SL'_{mass}(A&S) increased at all sites, with values ranging from 12.6 ± 8.2 mm/decade to 32.3 ± 8.1 mm/decade. The range of GRACE ocean mass changes calculated over the same periods is 8.4 ± 1.9 mm/decade to 28.9 ± 2.2 mm/decade. The mean increase in ocean mass at all mooring sites is comparable for the altimetry-mooring and GRACE estimates at 17.8 ± 4.0 mm/decade for ΔSL_{mass}(A&S) and 15.6 ± 1.8 mm/decade for ΔSL_{mass}(G). The root mean square difference, or RMSD, between ocean mass changes for the five moorings calculated from equation 3.1 and those measured by GRACE at the respective sites is 3.5 mm/decade. The RMSD is less than a quarter of the mean trend, and lower than the smallest observed change of 8.4 ± 1.9 mm/decade, demonstrating that the two methods yield consistent results. The agreement is also much better than the accuracies typically given for trends in both the altimetry and GRACE ocean mass measurements (section 3.2.4), suggesting that errors in the trend may be smaller than previously thought.

Table 3.2: Components of the sea level budget (in millimeters per decade). Uncertainties represent the instrumental error (section 3.2.4).
Δ**SL$_{alt}$**: Sea surface height change from satellite altimetry
Δ**SL$_{steric}$**: Steric height change from *in situ* density data
Δ**SL$_{mass}$(A&S)**: ocean mass change calculated as the difference between ΔSL_{alt} and $\Delta SL_{\text{steric}}$
Δ**SL$_{mass}$(G)**: ocean mass change from GRACE over the same time period
*: no data for MOVE 1 between 08/2006 and 12/2010

Mooring site	time period	ΔSL_{alt}	$\Delta SL_{\text{steric}}$	ΔSL_{mass}(A&S)	ΔSL_{mass}(G)	
RAPID WB3	2004/04-2017/04	98.0 $\pm$ 3.4	71.7 $\pm$ 7.4	**32.3** $\pm$ 8.1	**28.9** $\pm$ 2.2	
RAPID MARwest	2004/04-2017/04	37.3 $\pm$ 3.4	25.2 $\pm$ 7.4	**12.6** $\pm$ 8.2	**12.2** $\pm$ 1.6	
RAPID EB1	2005/04-2017/04	41.0 $\pm$ 4.0	21.6 $\pm$ 8.1	**15.2** $\pm$ 9.0	**8.4** $\pm$ 1.9	
MOVE 3	2002/04-2015/01	0.2 $\pm$ 3.6	-9.4 $\pm$ 8.7	**13.2** $\pm$ 9.4	**13.9** $\pm$ 2.2	
MOVE 1	2002/04-2015/01*	24.6 $\pm$ 2.7	12.0 $\pm$ 9.1	**15.7** $\pm$ 9.7	**14.7** $\pm$ 1.2	
Mean				**17.8** $\pm$ 4.0	**15.6** $\pm$ 1.8	**RMSD: 3.5**

Transect/station	time period	Lat/Lon range or station	ΔSL_{mass}(A&S)	ΔSL_{mass}(G)	
A05	2004/04, 2015/01	65°W-55°W, 24.5°N	21.6 $\pm$ 17.1	21.8 $\pm$ 5.9	
A05	2004/04, 2015/01	35°W-25°W, 24.5°N	22.9 $\pm$ 19.2	14.7 $\pm$ 5.9	
A20	2003/10, 2012/05	52°W, 25°N-35°N	10.9 $\pm$ 18.7	9.2 $\pm$ 5.9	
A16N	2003/07, 2013/08	26.2°W-20.6°W, 25°N-35°N	9.2 $\pm$ 15.7	7.9 $\pm$ 5.9	
Line W	2003/09-2013/06	station # 9014-9021	48.9 $\pm$ 11.6	57.4 $\pm$ 10.3	
BATS	2002/01-2017/01	64.4-63.9°W, 31.4-31.9°N	22.6 $\pm$ 3.2	31.5 $\pm$ 1.6	
Mean			**22.7** $\pm$ 5.8	**23.8** $\pm$ 2.4	**RMSD: 6.1**

Repeating the same analysis with different data products of GRACE yields larger RMS differences with ΔSL_{mass}(A&S) of about 14 mm/decade for the earlier JPL RL05.1 (non-mascon) solution and the CSR RL05.1 mascons (*Save et al.*, 2016). Their mean differences are over 10 mm/decade, compared to 2.2 mm/decade for JPL RL05.1M, suggesting possible biases. The recently released JPL RL06M solution is comparable to the RL05.1M version, with an RMSD to the mooring ΔSL_{mass}(A&S) estimate of 3.6 mm/decade. A detailed analysis of the advantages and disadvantages of the different GRACE products is beyond the scope of this study, but decadal ocean mass variability in the North Atlantic seems to be represented best in the JPL mascons compared to other gridded data. The JPL RL05.1M data are used for the remainder of this study, but the results presented here would not qualitatively change if RL06M data were used instead.

For additional validation of GRACE ocean mass trends, ΔSL_{mass}(A&S) is also calculated using ship-based hydrography data at six locations in the Atlantic (see section 3.2.1). The resulting estimate of ocean mass changes is again compared to ΔSL_{mass}(G) from the GRACE JPL RL05.1M product, shown in Figure 3.2 and Table 3.2 along with the mooring-based estimates. The hydrography data have a larger sampling error, and although they were corrected for short-

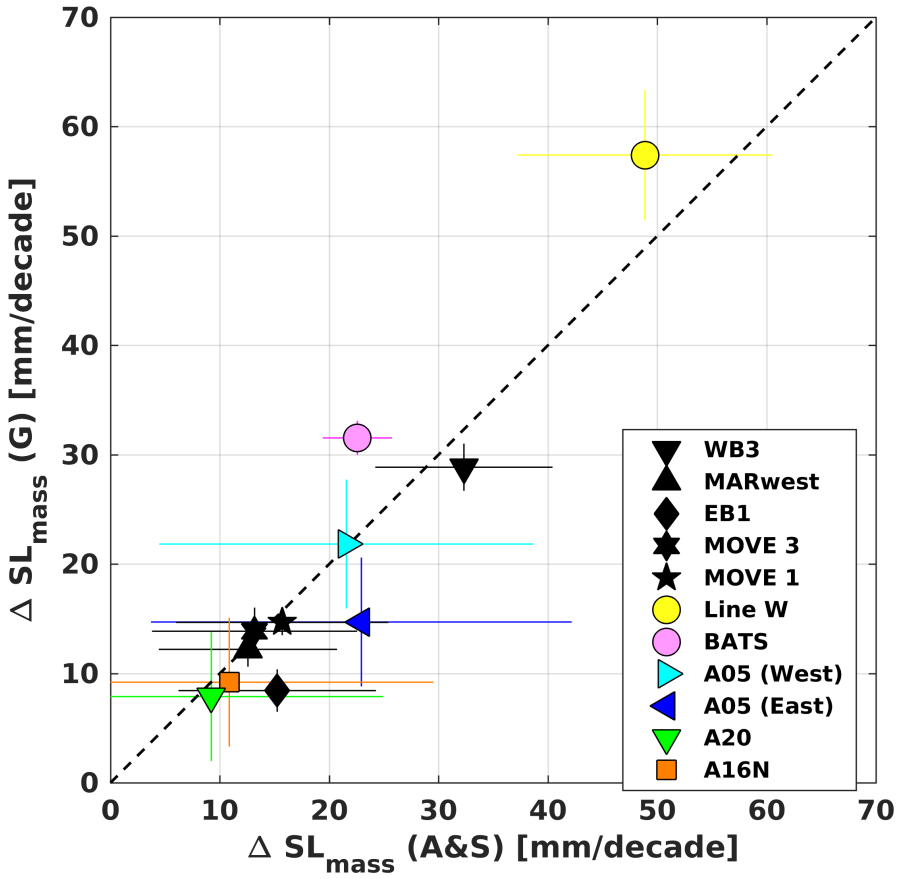

Figure 3.2: ΔSL_{mass}(G) from GRACE compared to ΔSL_{mass}(A&S) calculated as the difference between ΔSL_{alt} from altimetry and $\Delta SL_{\text{steric}}$ from moorings (black symbols) or hydrography data (other colors). Error bars show instrumental error (section 3.2.4). Symbols and colors correspond to those in Figure 3.1. The black dashed line shows a 1:1 slope.

term variability (equation 3.3), some of the associated noise will remain in the data. Nonetheless, ΔSL_{mass} calculated from altimetry and hydropgraphy data still agrees well with GRACE, with an RMS difference of 6.1 mm/decade. The combined RMSD between moorings & hydrography and GRACE is 5.1 mm/decade, with a correlation between ΔSL_{mass}(A&S) and ΔSL_{mass}(G) of 0.95. The mean difference is 0.4 mm/decade, suggesting that the mismatch is largely due to random variability, rather than a bias in one method relative to the other.

Thus, despite the potential additional error sources discussed in section 3.2.4, we find good agreement between ocean mass changes from the altimetry-steric height estimates and

GRACE in the North Atlantic, supporting the veracity of GRACE trends in this region. Due to the smaller sampling error in the method, the RMSD of 3.5 mm/decade between GRACE and ocean mass calculated from mooring data is likely more indicative of the real mismatch than the RMSD between GRACE and hydrography-based ocean mass. We use this value as an estimate of the error in the GRACE trend for the remainder of this study.

3.3.2 Spatial pattern of the trend

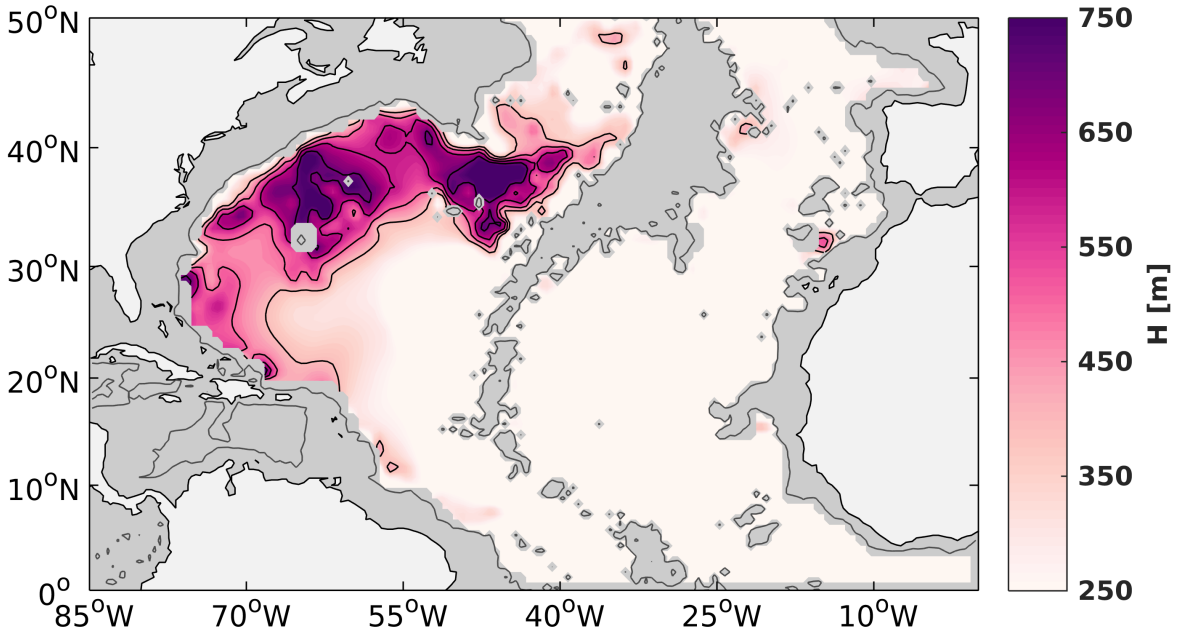

Figure 3.3: Maximum layer thickness, or vertical distance between σ_4 isopycnals of water with with silicate below 40 μmol L^{-1}, from World Ocean Atlas 2013 data (*Levitus et al.*, 2013). This highlights the Denmark Strait Overflow Water (DSOW), the lowest layer of NADW.

Although ocean mass increased throughout the North Atlantic ocean, the magnitude of the trend differs between the sites studied here. A distinct spatial pattern of the trend is evident in Figure 3.1, with the most pronounced feature being a ridge of strong ocean mass increases extending southwestward in the interior south of the Grand Banks. The pattern resembles maps of modeled float trajectory distributions and tracers associated with Denmark Strait Overflow

Water (DSOW), which comprises the lower part of NADW (*Lozier*, 2010; *Xu et al.*, 2015), as well as observed distributions of hydrographic properties in this water mass. Figure 3.3 shows the climatological maximum layer thickness for waters with a silicate content below 40 μmol L^{-1}, which is associated with the core of DSOW. The strongest signal is found west of the Mid-Atlantic Ridge (MAR) in the same interior regions where the largest trends in GRACE ocean mass occur. The resemblance between the spatial pattern of ocean mass trends and maps of NADW properties is another indication that the trend in GRACE is a real signal, as errors resulting from corrections such as those for Glacial Isostatic Adjustment (*Peltier*, 2009) and the pole tide (*Wahr et al.*, 2015) have larger spatial footprints and would not be expected to align with oceanographic features. Moreover, it indicates that the decadal signal measured by GRACE is related to changes in NADW, with implications for its circulation discussed in section 3.4.

Both the comparison with an independent estimate of ocean mass changes (Figure 3.2, section 3.3.1) and the spatial pattern of the trends (Figure 3.1) suggest that decadal GRACE ocean mass trends in the North Atlantic reflect real variability in the ocean. To our knowledge, this marks the first validation of decadal GRACE trends on sub-basin scales. At present, the tropical/subtropical North Atlantic is the only region with a sufficient number of long-term, well-calibrated, full-depth density moorings to carry out this comparison. As a result, we cannot validate ocean mass trends in different ocean basins, but similar analyses may become possible on a global scale in the future as instrument coverage in the ocean continues to improve.

3.3.3 Deep ocean contribution to steric height

Many studies of the global sea level budget have used steric changes only in the upper 1000 m or 2000 m (*Ivchenko et al.*, 2007; *Cazenave et al.*, 2008; *Leuliette and Miller*, 2009), ignoring changes below, mostly because of the better data availability in the upper ocean. *Purkey et al.* (2014) showed that this leads to a bias when calculating ocean mass trends as in equation 3.1 of 38%, 13%, 8% and 4% when only using data above 1000 m, 2000 m, 3000 m, or 4000 m for

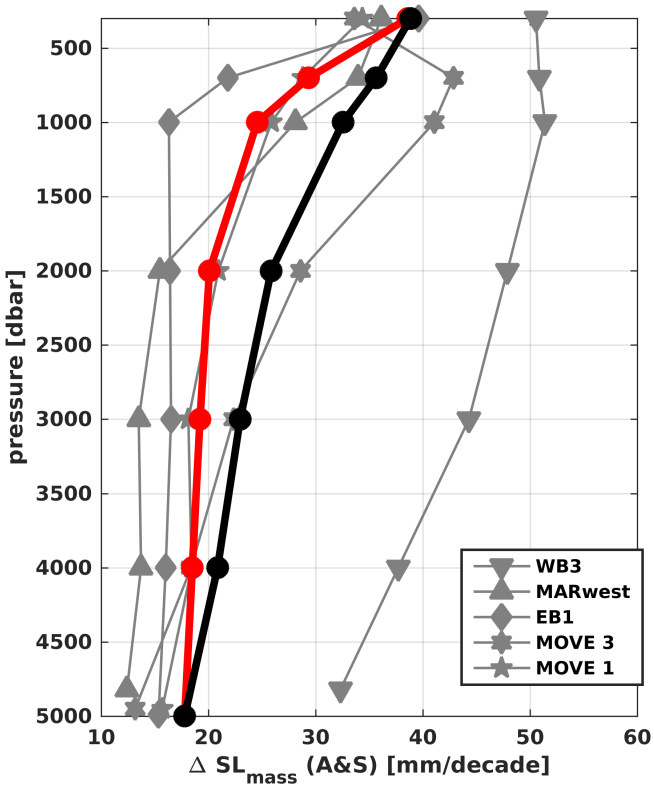

Figure 3.4: Ocean mass trend calculated using steric height data between the surface and each depth. The bottom-most data points correspond to the full-depth estimate of ocean mass trends used in Figure 3.2. The thick black line shows the average of all five mooring sites. The red line shows the profile that would be expected based on the global mean bias for each integration depth from *Purkey et al.* (2014)

the global ocean. Figure 3.4 shows the ocean mass trends calculated with steric height integrated from the surface to each depth, compared to the profile using *Purkey et al.* (2014)'s global estimate of the bias relative to the full-depth measurement. With the exception of EB1, where the ocean below 1000 dbar barely contributes to the budget, the positive bias introduced by ignoring the deep ocean is larger at all sites compared to *Purkey et al.* (2014). This is particularly true for the two moorings adjacent to the western boundary, WB3 and MOVE 3, where the density of North Atlantic Deep Water has been decreasing (*Frajka-Williams et al.*, 2018), leading to a bias of 48% and 117% in the ocean mass trend when using only steric height from 0-2000 dbar. At the MARwest and MOVE 1 moorings, the change below 2000 dbar is still larger than the global

average, but neglecting it only leads to a bias of 25% and 33%, respectively, compared to the global average of 13%. The average trend from the five mooring sites increases by 46% (94%) when using only 0-2000 dbar (0-1000 dbar) steric height, much larger than the 13% (38%) in *Purkey et al.* (2014). This analysis shows that while measuring the deep ocean is vital for resolving the global sea level budget, its importance is also spatially variable, and these differences need to be considered in studies on more regional scales. Our data thus underline the importance of a network of sustained deep ocean density measurements from moorings, CTD transects, and the Deep Argo program (*Johnson et al.*, 2015) for accurately monitoring long-term changes to the sea level and ocean mass budgets, particularly in the Atlantic Ocean.

3.4 Circulation changes

The increase in ocean mass measured by GRACE provides information on deep ocean current changes with unprecedented spatial coverage, revealing variability along the pathways of the deep circulation. The ocean mass difference between the 2002-2009 and 2010-2017 periods in the GRACE data (Figure 3.1) can be used to infer circulation changes, shown as vectors in Figure 3.5a. In this study, the term *circulation* is used to refer to the near-bottom velocity calculated using equation 3.4 multiplied by the horizontal distance Δx. The decadal circulation change is dominated by a large-scale anticyclonic pattern, with northeastward flow near the coast and southwestward flow in the interior. The pattern extends from 30°N to the subpolar-subtropical gyre transition zone at about 45°N (*Buckley and Marshall*, 2016) and is most pronounced near the two main southward spreading paths of NADW, which are described in the following and shown schematically in Figure 3.5b.

The most prominent pathway is the Deep Western Boundary Current (DWBC), which flows southward from the source region in the subpolar North Atlantic, following the continental slope, with a mean transport of about 20 Sv (1 Sv $= 10^6$ m^{3}s^{-1}) (*Toole et al.*, 2017). South

of 45°N, southward flow of NADW also occurs in an interior branch (IB), which rejoins the boundary current near 30°N. Between the two branches, NADW recirculates in a clockwise, or anticyclonic, fashion in a series of eddy-driven recirculation gyres (*Lozier*, 1997; *Gary et al.*, 2011). Model studies in both idealized and realistic settings (*Spall*, 1996a; *Gary et al.*, 2011; *Lozier et al.*, 2013) have suggested that the interior branch is fed by these recirculation gyres, containing water swept away from the DWBC by eddies, which form at points where the DWBC crosses under the Gulf Stream as a result of interaction between the two currents (*Spall*, 1996a). The existence of an interior branch of NADW is well-established, with evidence of southward interior flow observed in hydrography (*Lozier*, 1997), Lagrangian float trajectories (*Bower et al.*, 2009) and tracer distributions (*Rhein et al.*, 2015; *Smith et al.*, 2016). However, relatively little is known about either the mean transport in this branch or its variability. An overview of the North Atlantic circulation compiled from different hydrographic studies (*Schmitz and McCartney*, 1993) lists the interior transport as 5 Sv, but relies on an assumed level of no motion for the estimate. More recent studies have largely focused on a Lagrangian assessment of particles entering the interior pathway, rather than quantitative transport estimates (*Bower et al.*, 2009; *Gary et al.*, 2011; *Lozier*, 2010; *Lozier et al.*, 2013).

The GRACE data can help fill part of this gap in our understanding, providing information on changes in the NADW circulation, although they cannot be used to study the mean flow. We first determine whether GRACE data can be used to study not only circulation, i.e. bottom current, changes, but also changes in overall transport of NADW. This is followed by a quantitative analysis of the changes seen in Figure 3.5a, a discussion of the possible causes for the observed change, and an analysis of the net circulation change.

3.4.1 GRACE as a measure of NADW transport change

The ocean mass data from GRACE can only provide information on the velocity change near the ocean bottom, and consequently the barotropic component of the transport (section 3.2.3).

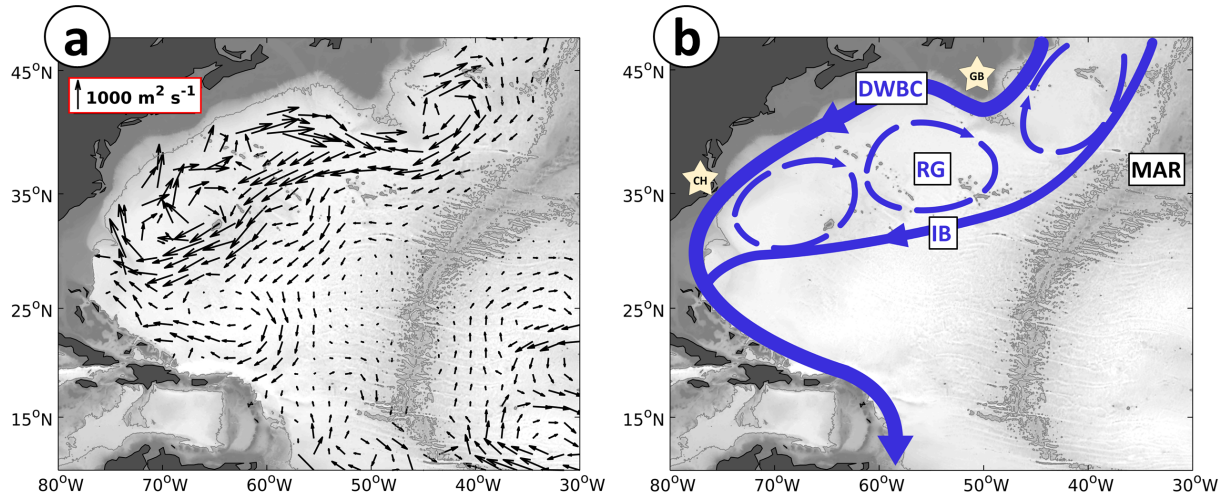

Figure 3.5: **a)** Circulation anomalies resulting from ocean mass changes (Figure 3.1), expressed as volume transport per unit depth. Current vectors are calculated from GRACE data interpolated from the centers of the mascons to a regular grid spaced $1.5° \times 1.5°$. Shading shows bathymetry from *Smith and Sandwell* (1997).
b) Schematic of major features of North Atlantic Deep Water (NADW) spreading in the North Atlantic. Pathways of NADW, based on *Gary et al.* (2011), are shown in blue, with solid lines showing the Deep Western Boundary Current (DWBC) and interior branch (IB), and dashed lines showing the anticyclonic recirculation gyres (RG). Geographic features mentioned in the text are also marked: Grand Banks (GB), Cape Hatteras (CH), and the Mid-Atlantic Ridge (MAR)

If the baroclinic (sheared) transport in the NADW layer were small, the NADW transport anomaly could then be inferred from GRACE alone by multiplying the circulation anomaly with the layer thickness of about 3000m. However, this need not be the case, as the baroclinic component, which can be inferred from density gradients, can often dominate the transport variability (*Send et al.*, 2011). Although density data are available at the sites used in this study (Figure 3.1), their distribution is insufficient to investigate the change in transport associated with circulation changes in Figure 3.5a. In this section, we evaluate to what extent transport changes derived from GRACE alone are representative of the change in NADW transport and can thus be used to study the transport change without the use of co-located density measurements.

We calculate the contribution of the bottom pressure from GRACE and of density variations in the water column to the $1000 - 4000$ dbar transport change of the single mooring

and hydrography locations used in this study (Figure 3.6). This is equivalent to the barotropic and baroclinic transport change between the site in question and a point with constant ocean mass and density. Baroclinic changes are largest at the western boundary locations, where steric height changes contribute the most to the ocean mass budget (section 3.3.3), but the barotropic change is the dominant component at all sites. This is particularly true for the two sites in the region of the strongest ocean mass changes between 30°N and 40°N, Line W and BATS, suggesting that GRACE alone is sufficient to approximately measure the NADW transport change in this region. The average absolute value of the baroclinic change is 2.4 Sv, so we take $2.4 \text{ Sv} \times \sqrt{2} = 3.4 \text{ Sv}$ as an estimate of the error in transport between two points that is incurred by ignoring the baroclinic transport change. The error in the ocean mass gradient is taken to be $3.5 \text{ mm/decade} \times \sqrt{2} = 4.9 \text{ mm/decade}$, based on the RMS difference in section 3.3.1. The associated error in circulation and transport depends on the latitude, and increases towards the equator. At 30°N, it is 536 $\text{m}^2 \text{ s}^{-1}$, or 1.6 Sv. In the following sections, we use the barotropic transport change from GRACE as a measure of the total transport change. Both the error in the ocean mass gradient and the error due to not resolving baroclinic changes contribute to the uncertainty in the transport change. When discussing circulation changes near the bottom, the uncertainty comes only from the error in measuring the ocean mass gradient.

3.4.2 Changes in strength of NADW pathways

After verifying that the decadal trends in GRACE are representative of variability in the real ocean (section 3.3), and can be used as an approximate estimate for the total NADW transport change (section 3.4.1), we now use the data to quantitively investigate changes in the NADW layer. We focus on the region west of the Mid-Atlantic Ridge, where the bulk of the mean flow of NADW occurs (*Lozier*, 2010), and the ocean mass trends observed by GRACE are strongest (Figure 3.1). As discussed above, the decadal change observed by GRACE is most pronounced close to the main pathways of NADW. To quantify the circulation and transport change between the

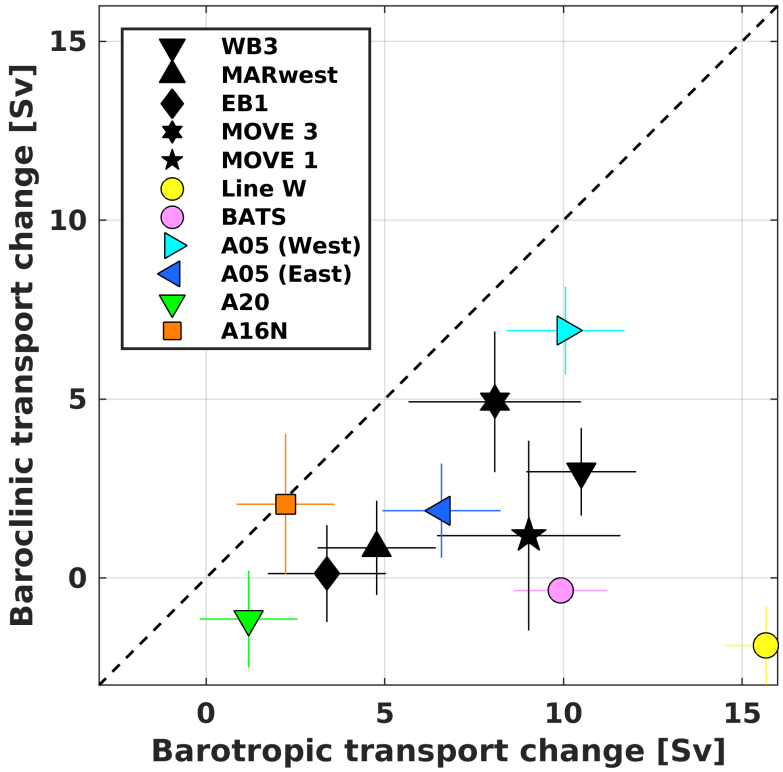

Figure 3.6: Barotropic transport change from GRACE compared to baroclinic transport change from density measurements, integrated between 1000 and 4000 dbar for each site. Periods used for the averaging are the same as in Figure 3.2, but are scaled to represent the change over an 8-year period, rather than a decade, to be consistent with transport changes discussed in the following section. Uncertainties are based on the 3.5 mm/decade RMSD for GRACE, and uncertainties of density measurements as defined in section 3.2.4.

2002-2009 and 2010-2017 periods, we calculate at each latitude the zonally integrated change for two regions: Between the western boundary and the location of the maximum ocean mass trend from Figure 3.1, which marks the center of the anticyclonic circulation anomaly, and between the maximum and the Mid-Atlantic Ridge. We refer to the two regions as the (deep western) boundary current, or DWBC, and interior branch, IB. By construction, the sign of the change for these segements is opposite at each latitude. Due to the coarse resolution of GRACE, the Deep Western Boundary Current cannot be separated from the part of the recirculation gyre with northward mean flow (Figure 3.5b). As a result, changes in the DWBC region may in part reflect

changes in recirculation strength, rather than the strength of the DWBC itself. The circulation change for the two regions is shown in Figure 3.7, along with transport change, calculated as circulation change multiplied by a 3000m layer thickness.

Between 20°N and 45°N, changes for both the DWBC and interior branch are larger than the error derived in section 3.4.1. Changes are largest in the latitude range of 30-40°N, where the recirculation gyre and interior flow are most pronounced (*Lozier*, 1997, 2010), and the barotropic transport change measured by GRACE is the dominant component (Figure 3.6). Between 30°N and 40°N, the circulation change for the interior branch is -4638 ± 473 m^2 s^{-1}, and the associated transport change is -13.9 ± 3.7 Sv, indicative of strengthened southward advection of NADW. For the DWBC, the circulation change is 3561 ± 473 m^2 s^{-1}, corresponding to a change in the transport of 10.7 ± 3.7 Sv. The 10.7 Sv change for the DWBC is comparable to the DWBC trend observed by current meter moorings near Line W, where transport decreased from -26.4 Sv to -19.1 Sv between 2004 and 2014 (*Toole et al.*, 2017). The concurrent increase in southward flow in the interior of -13.9 Sv in the present study suggests that the weaker DWBC reported by *Toole et al.* (2017) is not necessarily associated with an overall weakening of southward NADW transport, but rather represents an increased importance of the interior pathway relative to the DWBC. The net transport from GRACE even suggests an overall strengthening of NADW transport (black line), although it is not statistically significant at -3.2 ± 3.7 Sv. In a Lagrangian model study of NADW pathways, *Bower et al.* (2009) showed that most NADW water parcels are found in the interior as opposed to the DWBC between 42°N and 30°N, and suggested that the interior branch may be the main pathway for NADW in this latitude range. The strengthening of the interior branch by -13.9 Sv in the present study, more than half the mean strength of the DWBC, suggests that pathways in the interior have become even more important since (*Bower et al.*, 2009)'s study.

The NADW transport and circulation changes shown in Figures 3.5 and 3.7 add to the growing evidence that interior pathways play a significant role in the spreading of NADW

from its formation region (*Getzlaff et al.*, 2006; *Bower et al.*, 2009; *Lozier*, 2010; *Bower et al.*, 2019). While those previous studies focused mostly on the mean state, our results show that the importance of these different branches can also change substantially over time, highlighting the need for an improved understanding of the underlying dynamics.

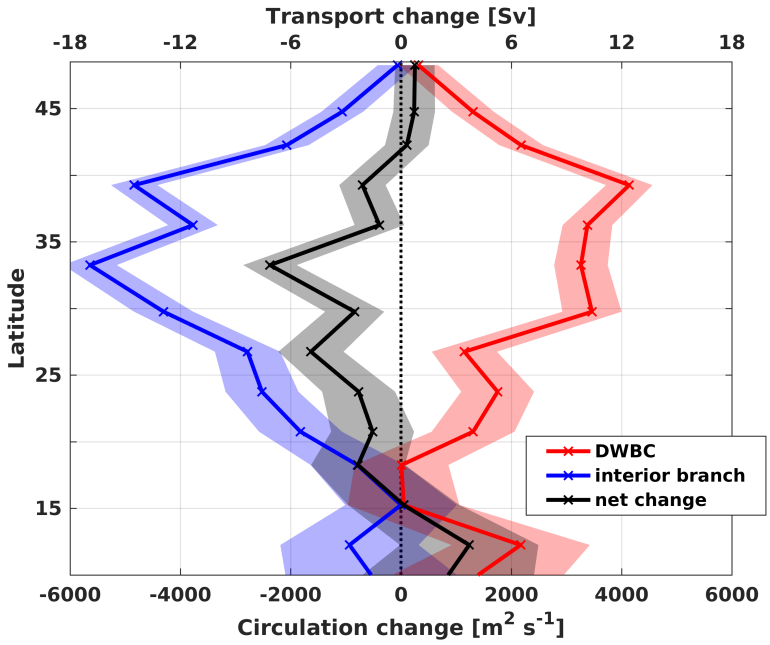

Figure 3.7: 2010/04/01-2017/03/31 minus 2002/04/01-2009/03/31 circulation change from GRACE, calculated for two regions (see text for definitions). Red: DWBC. Blue: interior branch. Black: Sum of the two. Shading represents uncertainty in the circulation change, which increases towards the equator as f becomes smaller. Numbers on the top of the x-axis show the equivalent change in transport over the NADW layer with an assumed thickness of 3000 m. Transport changes are calculated from GRACE only, resulting in additional uncertainty due to neglecting changes in velocity shear, estimated as 3.4 Sv (see section 3.4.1).

3.4.3 Possible causes of variability

The changes dicussed above may represent either a longer-term shift towards increased NADW flow in the interior, or part of a cycle of natural variability on multi-decadal time scales. In this section, we summarize several modes of multi-decadal variability in the Atlantic Ocean and discuss how the strengthened interior branch observed by GRACE could be related to each of

them.

The Deep Western Boundary Current, Gulf Stream, and interior pathways are linked dynamically through their interactions at the crossover points such as the Grand Banks near 42°N (*Bower et al.*, 2009; *Gary et al.*, 2011) and Cape Hatteras near 35°N, where deep eddies entrain water from the DWBC into the recirculation gyres (*Spall*, 1996a). Due to this interaction with the surface circulation, *Lozier* (2010) proposed that the strength of the interior branch could be affected by atmospheric forcing. The major mode of interannual to multi-decadal atmospheric variability over the Atlantic Ocean is the North Atlantic Oscillation, or NAO. The positive phase of the NAO is associated with an increase in atmospherically driven variability in the ocean, such as a stronger Gulf Stream and North Atlantic Current (*Curry and McCartney*, 2001). During the 2010-2017 period, the NAO was predominantly in its positive phase. Increased surface circulation in the subtropical gyre (*Thompson et al.*, 2018) and reduced renewal of Eighteen Degree Water in the surface layer of the recirculation gyre (*Billheimer and Talley*, 2013, 2016) have both been linked to this persistent positive phase of the NAO. The increase in interior flow reported here could likewise be related to the prolonged period of positive NAO, with changes in surface forcing communicated to the deep ocean at the crossover points as proposed by (*Lozier*, 2010). In addition to the decadal change discussed throughout this study, the strength of the interior branch measured by GRACE also varies over an annual cycle, with a peak-to-peak amplitude of 7 Sv from April to October (Figure 3.8), and an opposing seasonal cycle for the DWBC. This seasonal dependence of the transport supports a connection to surface processes, although the forcing controlling seasonal and decadal variability may not necessarily be the same.

The circulation of NADW has been linked to the highly variable formation of Labrador Sea Water (LSW), one of the main water masses making up NADW, in the source region (*Yashayaev and Loder*, 2016). Although recent results have called into question the effect of the LSW formation rate on net transport (*Lozier et al.*, 2019), other aspects of the circulation could still be affected. The increase in interior transport shown here coincides with deeper convection starting

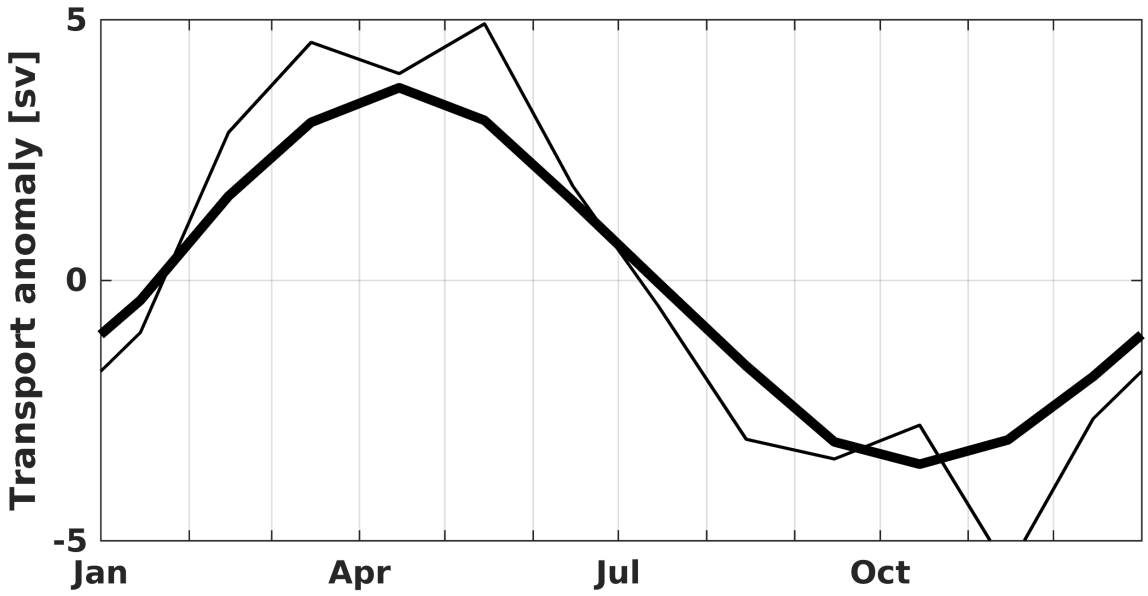

Figure 3.8: Annual cycle of barotropic transport in the interior branch from GRACE data. Thin line shows monthly means, thick line is a 5-point running mean

in 2012, and extending to depths close to the record values of the mid-1990s in 2016 (*Yashayaev and Loder*, 2017), after relatively weak LSW formation in the previous decade. *Yashayaev and Loder* (2016) showed that the export of LSW from the Labrador Sea is larger in years with deeper convection, and such an increase in LSW export after 2012 could be related to the strengthened interior branch observed in the present study. However, LSW formation is also strongly affected by the NAO, so the simultaneous increase in interior flow of NADW and convection depth in the Labrador Sea may simply be a result of the effect of atmospheric forcing on both.

Another possible explanation is internal variability of the recirculation gyre leading to stronger interior transport, as found in an idealized model by *Spall* (1996b). In the model, the feedback between Gulf Stream instabilities, eddies carrying water from the DWBC into the recirculation gyre, and recirculation strength causes oscillations in the system on multi-decadal time scales. *Andres* (2016) reported a decrease in Gulf Stream stability after 2008 and an associated increase in deep eddy activity, and proposed that these changes could be related to

such internal variability. A subsequent increase in interior NADW transport would be consistent with variability in this internal mode, representing a shift from the low energy to the high energy state. In the model, increasing transport in the interior branch is entirely fed by a larger fraction of NADW diverted away from the DWBC with no net transport change, leading to a weakened DWBC as observed by *Toole et al.* (2017). While the observed changes are similar to those proposed for this mode of variability, the oscillations in *Spall* (1996b)'s simple three-layer model affect mostly the upper core of the DWBC. In contrast, the interior transport change reported here is largely barotropic within the NADW layer, affecting both upper and lower North Atlantic Deep Water. More realistic models will be needed to determine whether variability associated with these internal oscillations can also extend to the lower part of NADW.

Regardless of the underlying causes, the observed change in the partitioning between the different pathways has important implications for measuring the AMOC: In tracer studies, for a given amount of net NADW transport, a weakened DWBC with a compensating increase in transport in the interior would increase the mean transit time, and could be erroneously attributed to a weakened overall southward flow of NADW (*Lozier*, 2010). In addition, a major motivation for studying the deep circulation is the spreading of dissolved gases such as carbon dioxide (*Sabine et al.*, 2004), which will be affected by variability in the relative importance of boundary and interior routes (*Rhein et al.*, 2015). If the changes seen here represent a shift towards a strengthened interior branch, the properties of deep water throughout the Atlantic will be profoundly affected. If the changes are related to natural variability on decadal or multidecadal time scales, such as that associated with the mechanisms discussed above, a decrease in the strength of the interior branch would be expected to follow in the near future. Additional measurements over the next decades, such as from the GRACE Follow-On mission, as well as dedicated model studies, will be necessary to better understand the causes for the observed change in the strength of the different NADW pathways.

3.4.4 Net circulation change west of the MAR

Although most of the variability described above is associated with compensating northward and southward flow there is also a *net* change in bottom circulation in the western North Atlantic. Unlike the net transport change, the circulation change in much of the basin is different from zero within the uncertainty defined in section 3.4.1. Everywhere between 18°N and 40°N, the net circulation change is negative, with a mean change in this latitude range of -1000 ± 593 m^2 s^{-1} (Figure 3.7, black line). This means that zonally integrated deep velocities in the western subtropical Atlantic have generally become more southward from the 2002-2009 to the 2010-2017 period.

At 15°N, the net circulation change is close to zero at 48 ± 1011 m^2 s^{-1}, supporting the assumption made in the nearby MOVE array that the flow at the reference level is negligible on long time scales at this latitude (*Send et al.*, 2011). At 27°N, the 8-year bottom circulation change is -1633 ± 591 m^2 s^{-1}, opposite to the trend reported for the RAPID array at 26.5°N, where the constraint of mass conservation yields a northward trend in the reference level flow of about 10^{-4} Sv m^{-1} yr^{-1}, or 1000 m^2 s^{-1} decade^{-1}, from 2004 to 2014 (*Frajka-Williams et al.*, 2016). The deep changes inferred from GRACE remain southward if the analysis is extended across the entire width of the Atlantic to mimic the coverage of the RAPID array. The disagreement between GRACE and RAPID trends has been noted previously and attributed to possible errors in the decadal variability in GRACE data (*Worthington et al.*, 2019). To account for the difference between trends in RAPID and the GRACE JPL RL05.1M product, the error in the decadal trends of the zonal ocean mass gradient would have to be 23.3 mm/decade. In the present study, the GRACE-derived gradient between WB3 and MARwest differs from independent (altimetry & mooring) ocean mass measurements by only 3 mm/decade (Table 3.2). It therefore seems unlikely that GRACE errors alone can be responsible for the disagreement between the deep RAPID and GRACE trends. Some of the difference may be explained by the RAPID compensation term, T_{ext} (*McCarthy et al.*, 2015), not strictly corresponding to a reference level velocity. For

example, a change occurring in regions not sampled by the array, such as the ”bottom triangles” between moorings near the boundaries and Mid-Atlantic Ridge, would also be included in the compensation term. The discrepancy between GRACE and the external transport in RAPID will be explored further in a future study, which uses GRACE along with mooring density data from MOVE and RAPID to resolve the variability of both the barotropic and baroclinic components of NADW transport at 16°N and 26.5°N.

3.5 Summary

In this study, trends in the GRACE JPL RL05.1M product (*Watkins et al.*, 2015) were validated against ocean mass calculated from altimetry and moorings at five sites, showing consistent increases in ocean mass in the subtropical and tropical North Atlantic ocean (Figure 3.2). The mean trends are 17.8 ± 4.0 mm/decade for the altimetry-mooring estimate, and 15.6 ± 1.8 mm/decade from GRACE. The RMS difference between the methods is 3.5 mm/decade, suggesting that the long-term changes seen in GRACE data reflect real changes in the ocean. GRACE trends are also compared against a more uncertain estimate using hydrography instead of mooring data, again showing consistent trends, with an RMSD of 6.1 mm/decade. The GRACE ocean mass trends are further supported by a close resemblance of their spatial pattern to property distributions in the NADW layer. Changes in the deep ocean below 2000 dbar play an important part in the ocean mass budget, especially near the western boundary, showing the importance of resolving the full water column in studies of global sea level. The present study focuses on the North Atlantic, which is the region with the highest number of sustained long-term ocean monitoring efforts that can be used to verify trends in GRACE ocean mass. Deploying thoroughly calibrated moorings in other parts of the world ocean would be beneficial for validating ocean mass and altimetry measurements from future satellite missions on a global scale.

Ocean mass changes between the 2002-2009 and 2010-2017 periods indicate changes in

the circulation of North Atlantic Deep Water in the western North Atlantic (Figure 3.5): Near the Deep Western Boundary Current, the transport changes by 10.7 ± 3.7 Sv between 30°N and 40°, comparable to trends observed by (*Toole et al.*, 2017). This is balanced by a strengthened interior branch of NADW, with southward transport increasing by -13.9 ± 3.7 Sv. The net bottom circulation change between 18°N and 40°N west of the MAR is -1000 ± 593 m^2 s^{-1}, reflecting an overall increase of southward flow at depth, but net transport changes are not significant. At 15°N, the net circulation change is only 48 ± 1011 m^2 s^{-1}, consistent with the assumption made in *Send et al.* (2011) that long-term changes in the near-bottom flow are negligible at this latitude. At 27°N, the circulation change is -1633 ± 591 m^2 s^{-1}, which is of opposing sign compared to the external transport from the nearby RAPID array (*McCarthy et al.*, 2015).

Possible causes for the observed changes in the deep circulation of the Atlantic Ocean include variability in surface atmospheric forcing as part of the North Atlantic Oscillation, variable rates of deep water formation, or internal variability. The decadal changes measured by GRACE imply a major increase in the relative importance of interior flow compared to advection in the DWBC for the southward spreading of NADW between the 2000s and the 2010s. This supports the view that interior pathways play a fundamental role in the equatorward transport of NADW (*Lozier*, 2010), as opposed to the classical picture of a deep circulation dominated by the DWBC (*Stommel and Arons*, 1959). Our results show that the interior branch is not only important for the distribution of NADW in the mean state, but also varies in strength on decadal timescales, highlighting the need for sustained observations of both the boundary and interior regions for fully resolving the variability of the deep circulation.

3.6 Acknowledgments

JK was supported by NASA Headquarters under the NASA Earth and Space Science Fellowship Program (Grant NNX16AO39H). MOVE is presently supported by NOAA OOMD under

award NA15OAR4320071. MOVE was previously supported by the German BMBF. MOVE data are freely available through OceanSITES. Data from the RAPID-WATCH MOC monitoring project are funded by NERC (UK) and are freely available from www.rapid.ac.uk/rapidmoc. GRACE ocean data are available at http://grace.jpl.nasa.gov, supported by the NASA MEaSUREs Program. The Ssalto/Duacs altimeter products were produced and distributed by the Copernicus Marine and Environment Monitoring Service (CMEMS) (http://www.marine.copernicus.eu). Data sources for all data used in this study are listed in Table 3.1. The authors would like to thank Eleanor Frajka-Williams and Felix Landerer for helpful discussions and comments.

Chapter 3, in full, has been submitted for publication of the material as it may appear in Journal of Geophysical Research: Oceans, 2020. Koelling, J.; Send, U.; Lankhorst, M. The dissertation author was the primary investigator and author of this paper.

Chapter 4

Multi-decadal variability of North Atlantic Deep Water transport

4.1 Introduction

In the North Atlantic, the upper branch of the Atlantic Meridional Overturning Circulation (AMOC) advects warm near-surface water along the American coast in the Gulf Stream, which feeds the North Atlantic Current, crossing the Atlantic towards Europe and into the Nordic Seas. Near Greenland, surface waters cool and sink to depth in the Nordic and Labrador Seas, and return southward as North Atlantic Deep Water (NADW) in the cold lower branch of the AMOC. The AMOC is known to play a crucial role in the global climate system, with the northward advection of warm surface waters causing a poleward heat transport, which warms the atmosphere (*Sutton and Hodson*, 2005). In the lower branch, the southward export of North Atlantic Deep Water sets the properties of much of the deep North Atlantic Ocean (*Johnson*, 2008; *van Sebille et al.*, 2011).

Due to the importance of the AMOC for global climate, several observing systems have been put into place in the Atlantic Ocean over the last two decades. As of 2019, six separate

mooring arrays are being maintained between the subpolar North Atlantic and 35°S (*Frajka-Williams et al.*, 2019). The first, and longest-running, of these mooring arrays is the Meridional Overturning Variability Experiment, MOVE (*Kanzow et al.*, 2006; *Send et al.*, 2011), which has been measuring the southward flow of NADW between Guadeloupe and the Mid-Atlantic Ridge (MAR) at 16°N since 2000. At 26°N, the RAPID/MOCHA/WBTS project (hereinafter referred to as RAPID for simplicity) has been in operation since 2004, and is aimed at measuring both the upper and the lower branch of the AMOC. To achieve this, more than 10 moorings are used to cover the entire Atlantic between the Bahamas and the coast of Africa, with a submarine cable measuring transports in the Florida Straits to the west of the array (*McCarthy et al.*, 2015). The positions of both the MOVE and RAPID arrays are shown in Figure 4.1.

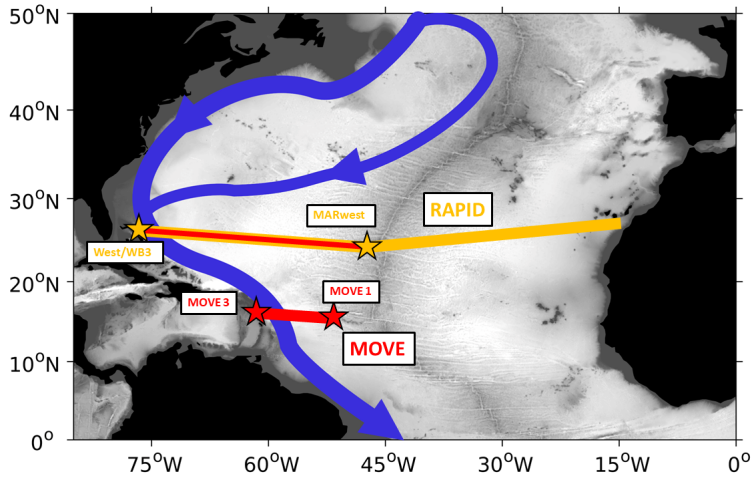

Figure 4.1: Simplified schematic of NADW pathways. The position of MOVE and RAPID arrays are shown as orange and red lines. The red line for RAPID shows the transect used for the transport referenced to GRACE in section 4.4.1. Symbols show locations of moorings mentioned in the text.

The intensifaction of AMOC observations is motivated in large part by results from climate models, which suggested that anthropogenic climate change may lead to a slowdown of this circulation, which in turn would profoundly affect Earth's climate (*Thorpe et al.*, 2001; *Caesar et al.*, 2018). Climate models have also shown that low-frequency variability in the AMOC exists on a host of time scales from 10 years to several decades (*Danabasoglu*, 2008; *Ortega*

et al., 2015; *Wen et al.*, 2016; *Muir and Fedorov*, 2017). If a weakening trend related to climate change is to be detected by the observations, the nature of such multi-decadal variability will need to be better understood in order to separate this natural variability from anthropogenically forced changes. Another reason for the plethora of observing systems is the question of whether or not changes in the AMOC are latitudinally coherent, and if so, what causes this coherence (*Frajka-Williams et al.*, 2019). Early models suggested that measuring the AMOC at one latitude is sufficient to know about its variability, which in part motivated the RAPID array as a means of comprehensively measuring the state of the overturning. More recently, studies primarily based on models have shown that changes are not coherent between the subtropical and subpolar gyres (*Zhang*, 2010; *Buckley and Marshall*, 2016), prompting the deployment of the Overturning in the Subpolar North Atlantic (OSNAP) array (*Lozier et al.*, 2017). In the subtropics and tropics, many model studies suggest that anomalies are communicated through boundary waves (e.g. *Zhang* (2010)), with the time scale of propagation depending on the model configuration (*Marshall and Johnson*, 2013). Other authors have suggested that density anomalies are advected with the Deep Western Boundary Current (*Buckley et al.*, 2012), which is consistent with tracing of water mass properties (*van Sebille et al.*, 2011; *Le Bras et al.*, 2017), and would imply that variability can be out of phase even within the subtropical gyre.

The MOVE and RAPID time series now have overlapping records for almost 15 years, allowing for comparison of signals on interannual to multi-decadal time scales. While early results from both arrays had a similar weakening trend in the southward transport of NADW (*Send et al.*, 2011; *Smeed et al.*, 2014), recent data seem to show a divergence of decadal variability (*Baringer et al.*, 2018). *Frajka-Williams et al.* (2018) suggested that the difference in transport may be related to the methods used for calculating the transport at each array, rather than a real difference between the two latitudes. At MOVE, the principal error that could result from assumptions inherent to the methodology is due to the assumed level of no motion at depth, which was chosen to be at the approximate interface of southward-flowing NADW and northward-flowing Antarctic

Bottom Water, AABW (*Send et al.*, 2011). This assumption can be explicitly tested by using measurements of bottom pressure to calculate the velocity at this level.

In this study, we use bottom pressure data from the GRACE (Gravity Recovery and Climate Experiment) satellite mission (*Tapley et al.*, 2004) to calculate the reference level velocity at MOVE, thus eliminating the need for an assumed level of no motion. This is followed by an analysis of the source of the transport variability observed at MOVE. Finally, we compare the transport at MOVE to that calculated at RAPID, and calculated from RAPID mooring data using the same method as at MOVE. Transports discussed throughout this study are related to southward flow of North Atlantic Deep Water, rather than the northward AMOC in the surface layer, so more negative values correspond to stronger transport.

4.2 Data and Methods

4.2.1 Data

In this study, we use data from the MOVE and RAPID projects, along with satellite data from the GRACE mission (*Tapley et al.*, 2004), to calculate deep water transports. Temperature (T) and salinity (S) at MOVE are measured using about 20 Seabird SBE-37 Microcat instruments throughout the NADW layer, with a spacing of about 200 m between instruments. The data are averaged daily and interpolated onto a pressure grid with 50 dbar spacing as anomalies from the climatological mean between sensors at both mooring sites. The raw and gridded data, and the resulting transports are available at ftp://data.ndbc.noaa.gov/data/oceansites/DATA/. Data from the moorings that are currently in the water, deployed in June 2018, were downloaded acoustically in December 2019, and have therefore not been calibrated yet. The data are shown as dashed lines in the figures to differentiate them from the rest of the dataset.

RAPID transport and gridded T and S data are downloaded from the official website, http://rapid.ac.uk. The instrument setup for each mooring, as well as the processing of T and S

data, is done a similar fashion to MOVE, described in *McCarthy et al.* (2015). The data used in this study for calculating RAPID transports referenced to GRACE (section 4.4.1) are taken from the RAPID *West* and *MARwest* moorings (see Figure 4.1 for location).

In both projects, the individual MicroCAT sensors are attached to a CTD rosette before and after each deployment, and calibrated against the CTD data, resulting in an accuracy of 0.002 for salinity, and 0.002°C for temperature (*Kanzow et al.*, 2008).

For GRACE bottom pressure, the JPL RL06M.1 product is used, and adjusted for errors in the pole tide model following *Wahr et al.* (2015).

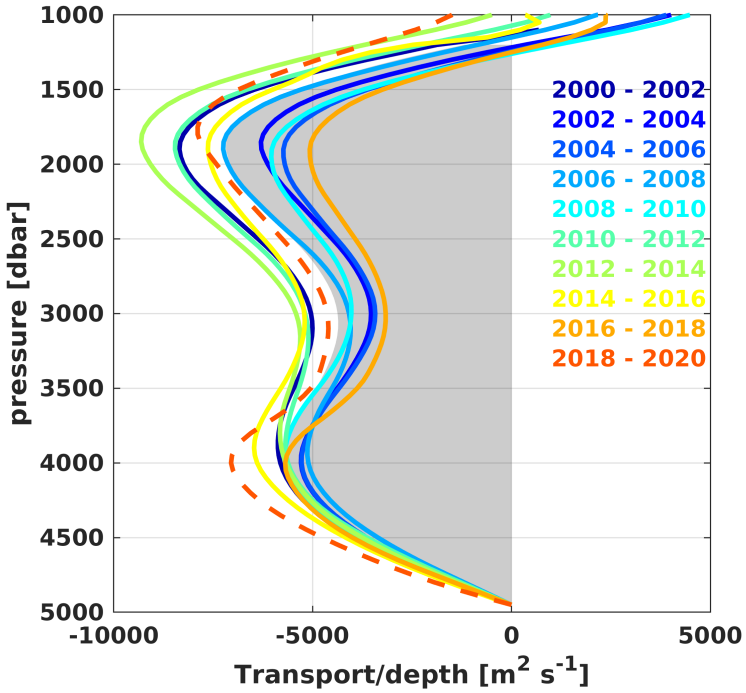

Figure 4.2: Velocity profile along the MOVE section calculated from the thermal wind relation. Colored lines show two-year means, and the shading shows the depth range integrated for the transport calculation.

4.2.2 Methods

The MOVE and RAPID arrays are designed to measure the geostrophic transport, making use of the fact that on time scales exceeding a few days, the zonally integrated meridional flow between two points is related to the zonal pressure and density gradients. In particular, the shear of the meridional velocity is calculated from the thermal wind equation:

$$\frac{\partial v(t)}{\partial z} = \frac{g}{\rho_0 f} \frac{\partial \rho(t)}{\partial x} \tag{4.1}$$

where g is the gravitational acceleration, f is the Coriolis parameter, ρ is density, and ρ_0 is a typical density of sea water. Integrating upward from a so-called reference level z_0 then yields the velocity profile relative to an unknown constant $v(z_0,t)$, known as the reference velocity. The velocity profile is calculated for each time step, integrated in depth, and multiplied by the section width to derive the transport. A common way to separate the transport calculated this way is splitting it into two components: the baroclinic, or internal, transport, calculated from the velocity shear with $v(z_0,t) = 0$, and the barotropic, or external, transport, which is given by $v(z_0,t)$ multiplied by the layer depth and section width. For both arrays, the western mooring used for the thermal wind calculation is at the bottom of the continental slope, with some of the Deep Western Boundary Current flowing over the sloping topography west of it. This additional component of the transport is measured directly by current meters deployed along the slope, referred to as the western boundary wedge (*Kanzow et al.*, 2006).

The mean velocity profile of the internal transport for MOVE is shown in Figure 4.2. Adding the external transport shifts the entire profile to the left or right, thus changing the transport integral. Both projects use equation 4.1 to determine the velocity shear, and similar reference levels of 4950 dbar for MOVE and 4820 dbar for RAPID, corresponding to the deepest common level measured by the moorings for each project. However, they differ in their handling of the reference velocity/external transport. For MOVE, the project location was specifically chosen

because the quasi-rectangular shape of the western basin allows much of the flow to be captured with two end-point moorings, and model studies suggested that the flow in the NADW layer east of the Mid-Atlantic Ridge is weak (*Kanzow et al.*, 2006). For the reference level, an assumption is made that although short-term variability may occur, long-term trends in reference velocity are negligible, so that it does not need to be resolved to capture variability on interannual and longer time scales. This assumption is based on the fact that the reference level is near the depth of the water mass interface between southward flowing NADW above, and northward flowing Antarctic Bottom Water below (*Send et al.*, 2011). For RAPID, the external transport component T_{ext} is implicitly derived by combining the internal and boundary wedge transports with other transport components and invoking a constraint of mass conservation. This approach is possible because the array spans the entire width of the Atlantic, and therefore the vertically integrated net mass transport through the section must balance on time scales exceeding a few days (*Kanzow et al.*, 2007).

In this study, we also use data from GRACE, which measures gravity anomalies that correspond to bottom pressure anomalies over the ocean. As the reference level is close to the sea floor, these can be used to calculate $v(z_0,t)$ for the MOVE section using geostrophy, eliminating the implicit assumption that has to be made for the bottom-referenced case. The RAPID compensation term is applied as a zonally averaged reference level velocity. As a result, transports are only given as a zonal mean and cannot be separated into components east and west of the Mid-Atlantic-Ridge. Using the GRACE data, we can calculate the transport in the same fashion as at MOVE, allowing for a more direct comparison of the two time series.

GRACE data used in this study are takken from the nearest grid point to the respective mooring sites. Differences in the bottom depth are assumed to be negligible, as all moorings are deployed at similar depths of about 5000 m.

In order to make the low-frequency changes that are the focus of this study more easily discernible, all Figures showing time series are plotted as 120-day running means (thin lines) and

3-year running means (thick lines), unless stated otherwise.

4.3 Variability at MOVE

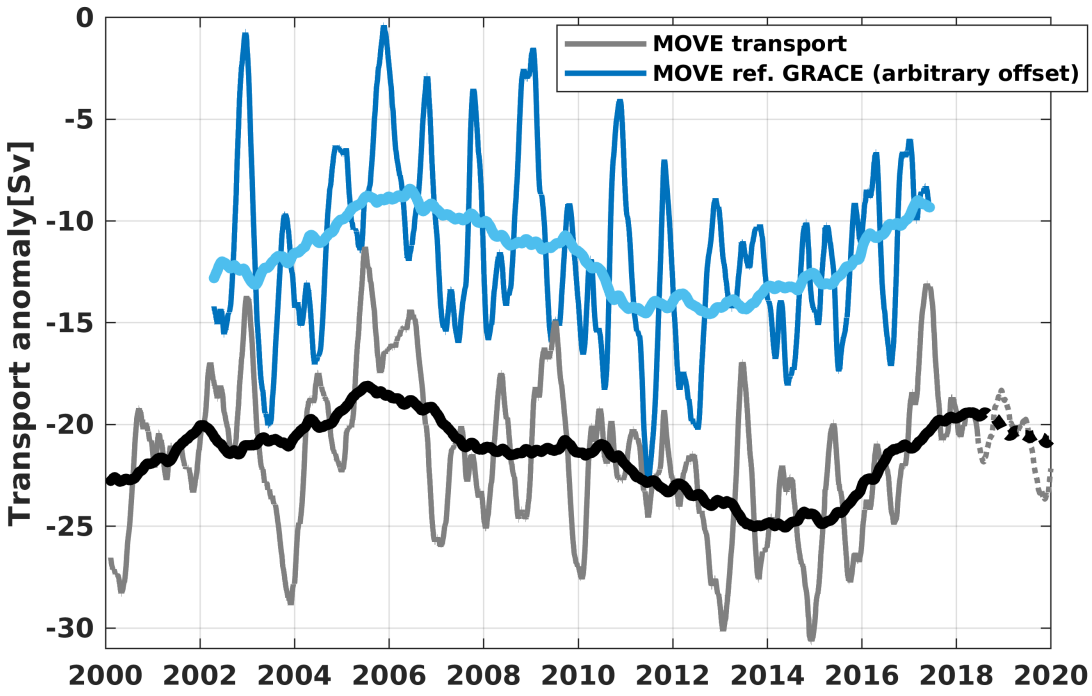

Figure 4.3: NADW transports anomalies from MOVE, filtered with 120-day running mean (thin lines) and 3-year running mean (thick lines). Black/gray lines show the transport calculated using only the mooring data, and blue lines show the transport using GRACE bottom pressure for the external transport. Transport time series calculated using GRACE data are offset by 10 Sv.

4.3.1 Transport

The transport of NADW calculated with the standard method for the MOVE array, using only the internal and boundary wedge transports, is shown as black and gray lines in Figure 4.3. Large transport variability occurs on a range of time scales, with transport changes by up to

15 Sv (1 Sv = 10^6 m^3 s^{-1}) over several months. The low-frequency changes that are the focus of this study are highlighted by the time series filtered with a 3-year running mean. NADW transport is weakening from -25 Sv to -20 Sv between the beginning of the record in 2000 and 2005, strengthening until 2014 to a maximum of about -27 Sv, and weakening again thereafter. The changes are indicative of multidecadal variability with a time scale of about 15-20 years, and a peak-to-peak amplitude of 6.96 Sv, with approximately one full cycle measured by the MOVE moorings. The amplitude of this variability is much larger than the uncertainty of 2.6 Sv for interannual changes in the MOVE transport (*Kanzow et al.*, 2008).

Although the reference level assumption at MOVE was supported by climate models at the program's inception (*Kanzow et al.*, 2006), variability at this depth could still exist and introduce spurious signals into the transport. Opposing variability on the order of just 2 mm s^{-1} for the mean reference velocity through the section would be enough to cancel out the multi-decadal signal seen at MOVE. To test the assumption explicitly, we employ data of Earth's gravity anomalies from GRACE, which over the ocean are equivalent to bottom pressure anomalies. Previous studies had suggested that corrections for geological processes in the data can cause spurious trends in ocean transports that are of the same order as real decadal signals, and they could therefore not be used to study oceanic variability on these time scales (*Landerer et al.*, 2015; *Worthington et al.*, 2019). However, *Koelling et al.* (2020) showed that GRACE trends agreed well with trends calculated from independent ocean mass estimates, including those made using MOVE data, with a root mean square difference (RMSD) of 3.5 mm/decade. We can therefore use GRACE to analyze the change in reference level velocity, using the 3.5 mm/decade RMSD to estimate the transport error (*Koelling et al.* (2020), see previous chapter). Using this together with the 2.6 Sv uncertainty for internal transport at MOVE from *Kanzow et al.* (2008), the uncertainty in decadal variability for the GRACE-referenced time series is 4.37 Sv.

The timeseries of the NADW transport referenced to GRACE is shown along with the regular transport estimate in Figure 4.3, with the curve using GRACE data offset by 10 Sv for

clarity. The GRACE data add variability on subannual time scales so that the transport anomaly relative to the mean is at times opposite to that inferred from the mooring data only. This may be related to westward propagating Rossby waves passing through the section (*Kanzow et al.*, 2008). However, the low-frequency changes that are the focus of this study are almost unchanged by the inclusion of the GRACE data and still exhibit multi-decadal variability, albeit with a slightly shifted phase. The peak-to-peak amplitude of the GRACE referenced time series is slightly reduced to 6.15 Sv, but is still larger than the uncertainty. This supports the assumption made in the MOVE array that the reference level velocity is negligible on long time scales (*Send et al.*, 2011) and confirms the veracity of the low-frequency variability inferred from mooring data alone.

While one cycle is not enough to make any statistically meaningful conclusions about the nature and causes of this variability, increased spectral energy with a comparable period is a feature common to many climate models (*Danabasoglu*, 2008; *Wen et al.*, 2016; *Muir and Fedorov*, 2017). Similarly, variability with periods around 20 years has been reported in proxy and paleo records thought to be linked to AMOC variability (*Frankcombe et al.*, 2010; *Chylek et al.*, 2011; *Vianna and Menezes*, 2013). The few other long-term transport time series that directly measure components of the AMOC have found variability on time scales of around 10 years for the upper-ocean Florida Current (*Meinen et al.*, 2010) and outflow of NADW from the Labrador Sea (*Zantopp et al.*, 2017), and about 20 years for the deep western boundary current in the Irminger Sea (*Sarafanov et al.*, 2009). In a recent study using satellite data, the strength of different pathways of NADW was shown to change from one decade to the next, which may be part of multi-decadal variability (*Koelling et al.*, 2020). The period of strengthened transport in the interior between 30°N and 40°N coincides with the increase in transport through the MOVE section, suggesting a possible connection between the two.

The most obvious comparison for the MOVE time series is the NADW transport in the RAPID array, which will be discussed in more detail in section 4.4. Here, the transport weakened

through the first 8 years, with no statistically significant change after 2012 (*Smeed et al.*, 2014, 2018). This decade-long weakening may also be part of longer-term variability, but more data will need to be collected to see whether transports will increase again in the future.

The prominence of the ∼20-year time scale in models has been linked to internal variability in the ocean (*Sévellec and Fedorov*, 2013; *Muir and Fedorov*, 2017), such as basin-scale thermal Rossby waves (*Te Raa and Dijkstra*, 2002; *Dijkstra et al.*, 2014), as well as to the North Atlantic Oscillation (*Danabasoglu*, 2008; *Wen et al.*, 2016), which is a mode of atmospheric variability on multi-decadal time scales. Regardless of the source of the variability, its multi-decadal time scale and magnitude point toward natural processes rather than changes related to anthropogenic climate change. If, as suggested by climate models, the AMOC weakens under global warming scenarios (*Thorpe et al.*, 2001; *Rahmstorf*, 2002; *Oltmanns et al.*, 2018), the expected effect on NADW transport would be a linear weakening trend, rather than a cyclical signal, and the magnitude would be an order of magnitude smaller (*Smeed et al.*, 2014). Given the strong multi-decadal variability shown here, observations will have to be sustained much longer in order to detect an anthropogenically forced trend.

4.3.2 Water mass changes

The fact that multi-decadal variability remains almost unchanged with the inclusion of the GRACE data implies that it is controlled mostly by changes to the horizontal density gradient, as opposed to the bottom pressure gradient. Much of the variability in the transport can be recovered using just data of density below 3000 dbar: If time-mean values are used above this depth, the phasing of the density-derived component of the transport stays consistent, and the peak-to-peak amplitude of the decadal variability decreases by only 27% (Figure 4.4a). This suggests that changes on these time scales are largely associated with variability below 3000 dbar. In this depth range, the dominant water masses are Denmark Strait Overflow Water (DSOW), and Iceland Scotland Overflow Water (ISOW), which in the western Atlantic is also referred to as Gibbs

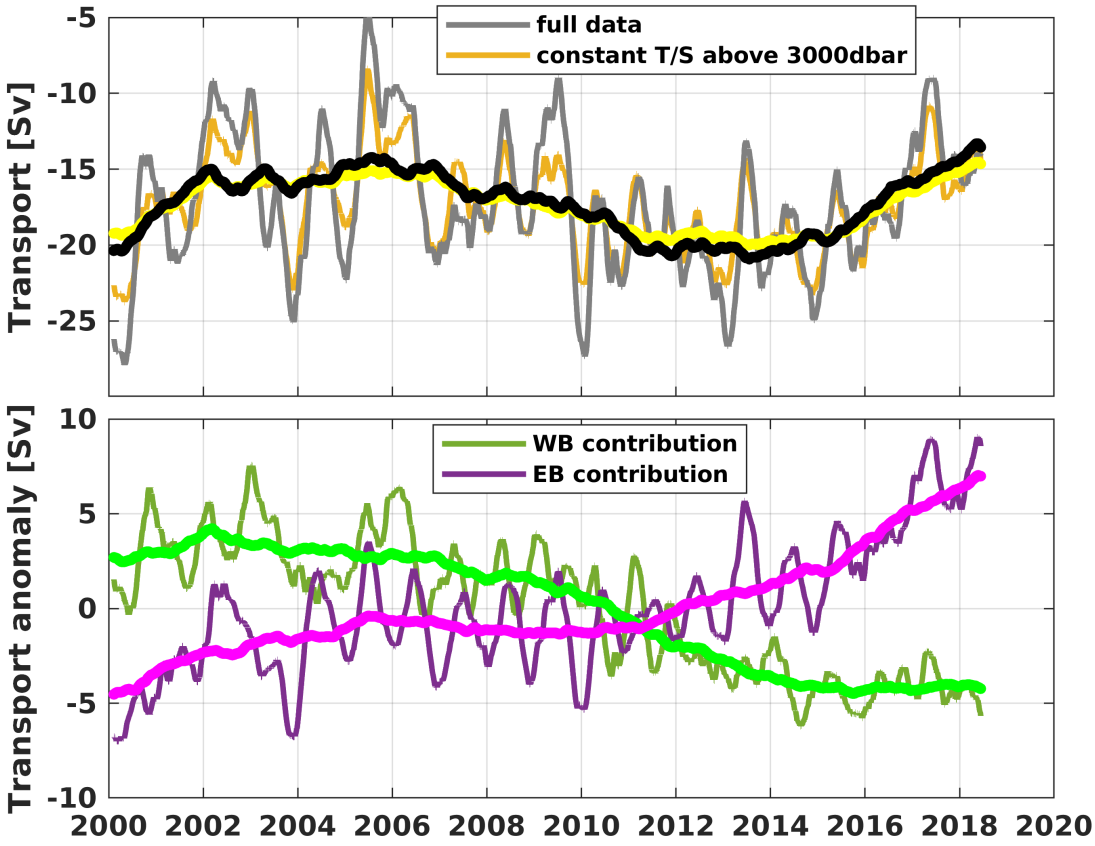

Figure 4.4: **a):** internal transport at MOVE calculatd from the full dataset (black/gray) and from density data below 3000 dbar only, using time-mean values above (yellow)
b): contribution from the western boundary mooring (green), and the eastern boundary/Mid-Atlantic Ridge mooring (purple) to the deep ocean changes in panel a)

Fracture Zone Water (*Send et al.*, 2011), as well as Antarctic Bottom Water (AABW) at the eastern mooring. Note that although the *density* changes with the largest effect on the transport variability occur in the overflow water layers, the resulting *velocity* variability is largest for the Labrador Sea Water layer (see Figure 4.2).

While most of the variability in North Atlantic Deep Water transport is often thought to be associated with the western boundary (*McCarthy et al.*, 2017), both sides contribute to the decadal changes seen here. The relative contribution of density changes at either end of the section is shown in Figure 4.4b. The initial decrease until 2005 appears to be caused by density changes at the eastern end, as discussed in *Send et al.* (2011). In contrast, the period of increasing transport

between 2005 and 2014 is related to a continuous strengthening trend due to density changes at the western boundary since 2005, which levels off again towards the end of the record. This strengthening is partially offset, and eventually reversed, around 2012 as decreasing densities at the eastern end lead to positive (weakening) transport anomalies.

Changes in density at a fixed location can be caused by property changes in the source water mass, lateral movement of water masses, or isopycnal heave (*Purkey and Johnson*, 2013), which is the local movement of density layers in the vertical. Below, we will discuss the source of the changes at each of the mooring sites, MOVE 3 and MOVE 1, with their locations shown in Figure 4.1.

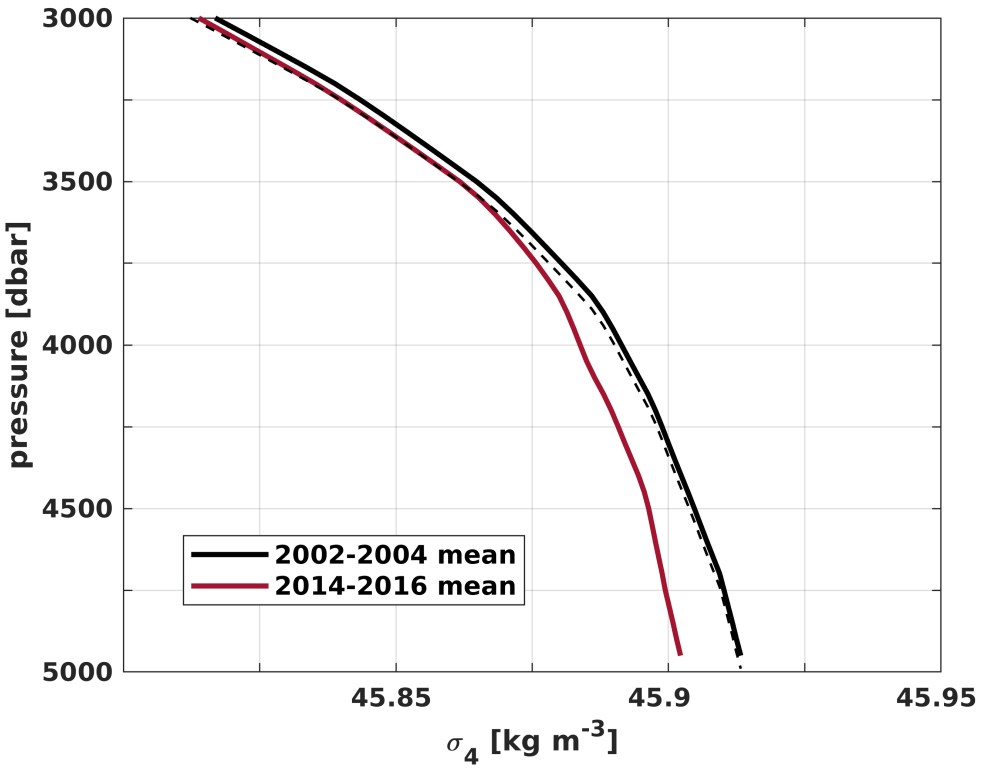

Figure 4.5: Profile of mean σ_4 potential density at the MOVE 3 (western boundary) mooring for the 2002–2004 period (black) and 2014–2016 period (red). The dashed line shows the 2002-2004 profile shifted downwards by 40 dbar.

MOVE 3 (western boundary)

At MOVE 3, a decrease in density throughout the deep ocean is responsible for its contribution to increasing transports. Figure 4.5 shows the mean profile of potential density averaged over two two-year periods at the beginning and end of the strengthening trend. The dashed line shows the change that would occur as a result of isopycnal heave, with the shape of the profile staying the same but moving downward by 40 dbar. While this could explain some of the change above 3800 dbar, the change below appears to be associated more with a overall decrease in density of about 0.011 kg m^{-3}, rather than vertical movement of isopycnals. This is supported by the change of temperature and salinity properties, shown in Figure 4.6. The change at constant depth, shown by the green lines connecting the symbols, is towards lower salinities everywhere in the overflow water layer. Isopycnal heave would result in little change to the initial T/S relation, but change the depths at which these properties are found. If this were the dominant process, the two T/S curves would lie on top of each other, with the lines of constant depth connecting points along this curve. As shown by the daily values, with the exception of a few outliers in the 2014-2016 period, there is almost no overlap in T/S space between the two periods. The properties shifted to an entirely different part of the T/S diagram over the course of 12 years, towards lower salinities and lighter densities. Clearly, this change seen at MOVE 3 is not consistent with variability due to isopycnal heave, and must instead be related to changes in the water masses found at the site.

At the upper end of the curve, the freshening is weaker, and more strongly compensated by opposing temperature changes, so that the T/S change is more along isopycnals, leading to the smaller density changes seen in Figure 4.5. Below 4000 dbar, temperature stays almost constant while freshening is on the order of -0.01 g/kg, leading to larger density changes, evident in the T/S-plot from the almost horizontal green lines that cross isopycnals towards lighter densities. Figure 4.7 shows the salinity at a fixed depth of 4500 dbar, the approximate depth of the core of DSOW, as well as density compared to the change that would result from salinity changes alone

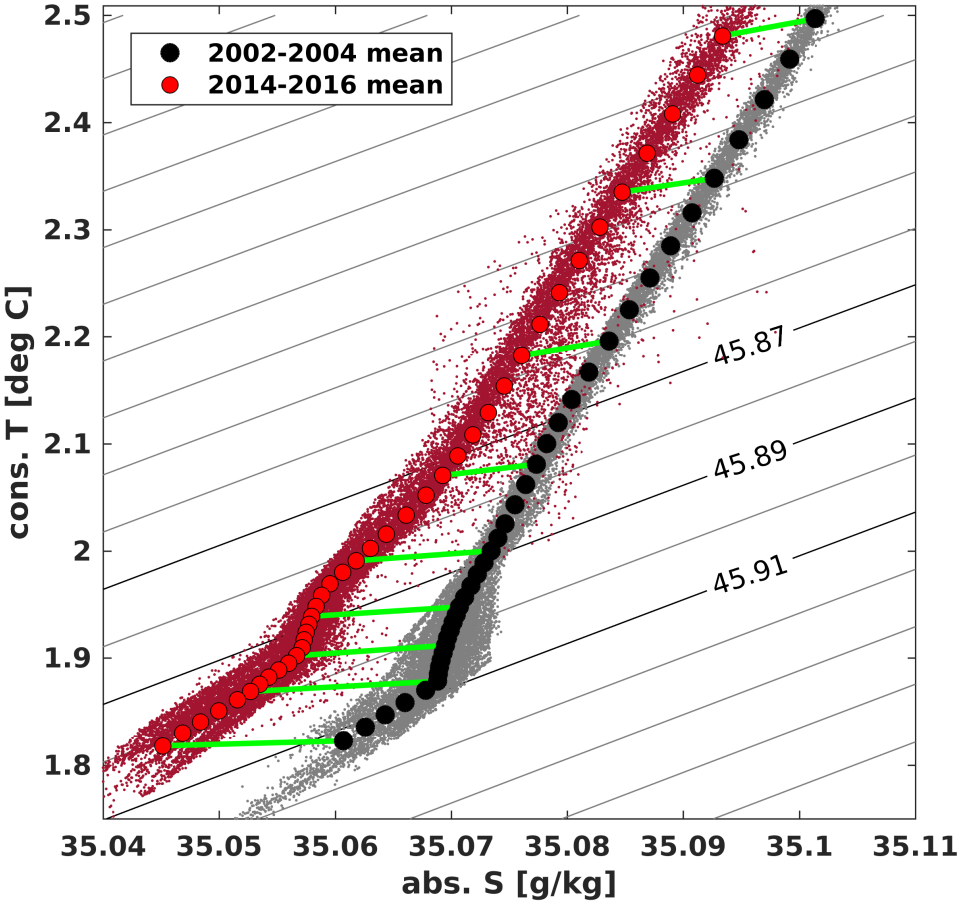

Figure 4.6: Temperature-salinity (T/S) plot for MOVE 3 data below 3000 dbar. Points in the background show daily values in the 2002–2004 (black) and 2014–2016 (red) periods every 50 dbar, and larger symbols show mean values for the two periods. Green lines connect values at the same depths every 250 dbar.

while temperature stays constant. With the exception of the first few years from 2000 to 2004, the long-term change in density can largely be explained by a nearly linear trend in salinity. While a single depth is shown here, the same is true for the entire DSOW layer. The salinity trend at 4500 dbar is -0.01 g/kg per decade, much larger than the measurement error of about 0.003 g/kg (*Kanzow et al.*, 2006; *Koelling et al.*, 2020).

This is comparable to changes in the source region, where a freshening trend of 0.012 g/kg has been observed since the 1960s (*Dickson et al.*, 2002). The magnitude of the trend observed

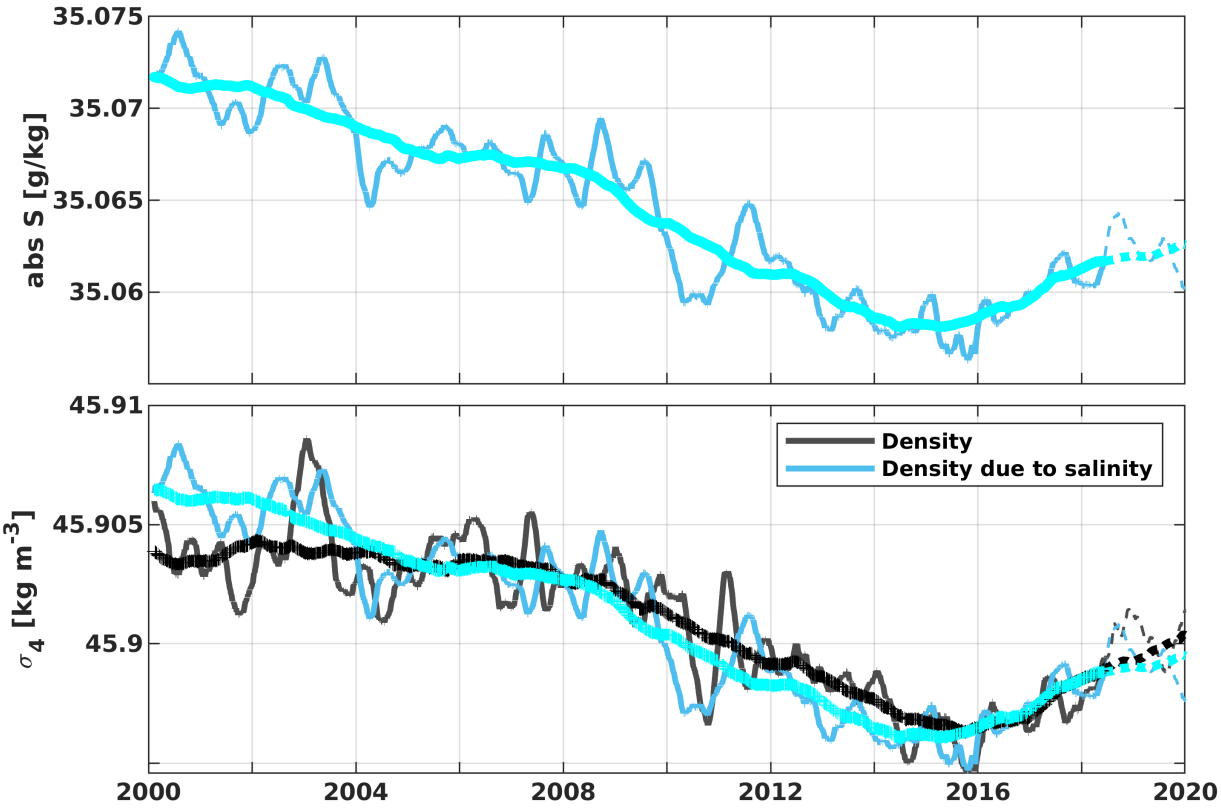

Figure 4.7: Time series of salinity (top) and σ_4 potential density (bottom) at the MOVE 3 (western boundary) mooring at 4500 dbar.

here suggests relatively little dilution of the signal between the Nordic Seas and MOVE 3, despite mixing occurring as the water mass transits the interior (*Lozier*, 2010; *Le Bras et al.*, 2017). Freshening trends in this water mass have also been observed upstream of MOVE at the Abaco line (*van Sebille et al.*, 2011) and Line W (*Le Bras et al.*, 2017). *van Aken and de Jong* (2012) suggested that the DSOW freshening in the Nordic Seas reported by *Dickson et al.* (2002) is in fact part of slow multi-decadal variability, and reported an increase in salinity since the early 2000s. The freshening at MOVE 3 appears to have halted around 2016, with the acoustically downloaded data from the most recent deployment suggesting an increase in salinity in the last 2 years. While more data will be needed to verify whether salinities will continue to increase, this could mark the arrival of the salinity trend reversal observed by *van Aken and de Jong* (2012)

at MOVE. The implied advection time scale from the subpolar North Atlantic would be about 15 years, at the lower end of the range inferred from tracer studies, which is between 15 years (*Rhein et al.*, 2004) and 25 years (*Rhein et al.*, 2015).

MOVE 1 (Mid-Atlantic Ridge)

For the MOVE 1 mooring near the Mid-Atlantic Ridge, the density change, and associated contribution to transport change, occurs in two periods from 2000 to 2005 and after 2011. The density profiles for the beginning and end are shown in Figure 4.8. As for MOVE 3, density decreases throughout the deep ocean. Density changes are largest below 4500 dbar, and between 3500 and 4000 dbar, and the maximum decrease at the lowest instrument is somewhat smaller than for MOVE 3, at about 0.007 kg m^{-3}. The associated T and S changes are shown in Figure

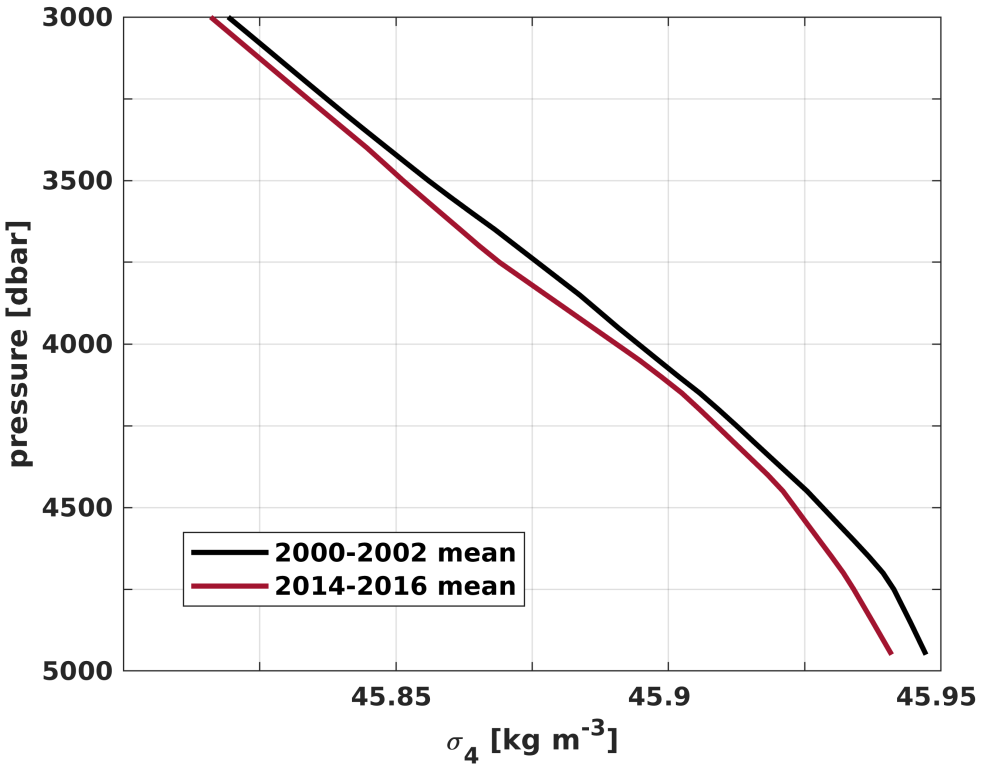

Figure 4.8: Profile of mean σ_4 potential density at the MOVE 1 (Mid-Atlantic Ridge) mooring for the 2000–2002 period (black) and 2014–2016 period (red).

4.9; again, salinity decreases throughout the deep ocean, but the freshening is weaker than at MOVE 3. Changes here mainly occur in two layers: For the overflow water masses, centered around 3750 dbar, and Antarctic Bottom Water below 4500 dbar. Current meters deployed as part of the Guiana Abyssal Gyre Experiment (GAGE) show that the mean flow at these depths is northward (*Kanzow*, 2004). For the overflow water, this represents a northward recirculation of NADW along the Mid-Atlantic Ridge after the DWBC reaches the equator (*Friedrichs et al.*, 1994; *Herrford et al.*, 2017). Thus, changes in the overflow layer may be related to those at the western boundary, and arrive at the MAR at 16°N several years later, with the signal being modified and weakened due to dilution. Based on (*Rhein et al.*, 2015), the time scale for signals to propagate from MOVE 3 to MOVE 1 via this route would be about 5-10 years. The change below 4500 dbar is associated with the upper edge of the colder, denser AABW below. This water mass enters the western North Atlantic through a narrow channel just north of the equator, and flows northward at the base of the MAR (*Herrford et al.*, 2017). For AABW, salinities have also been decreasing in the source region in recent decades (*Purkey and Johnson*, 2013), but this signal would not be expected to have reached the MOVE section yet. The salinity changes may be caused by earlier variability in AABW properties, or could be related to the changes in NADW, as the two water masses mix along the northward spreading path of AABW.

4.3.3 Comparison to theory, models, and other observations

The predominant view of meridional communication of AMOC variability, based on both idealized and realistic models, implicates Kelvin or Rossby waves along the basin's boundaries in the propagation of AMOC anomalies. *Kawase* (1987) and *Deshayes and Frankignoul* (2005) suggested buoyancy forcing in the North Atlantic would lead to rapid adjustment throughout the basin, as buoyancy anomalies travel along the boundary as Kelvin waves. *Biastoch et al.* (2008) suggested that changes could also be forced by variability in Agulhas leakage in the South Atlantic, and travel northward into the North Atlantic as boundary waves. *Zhang* (2010)

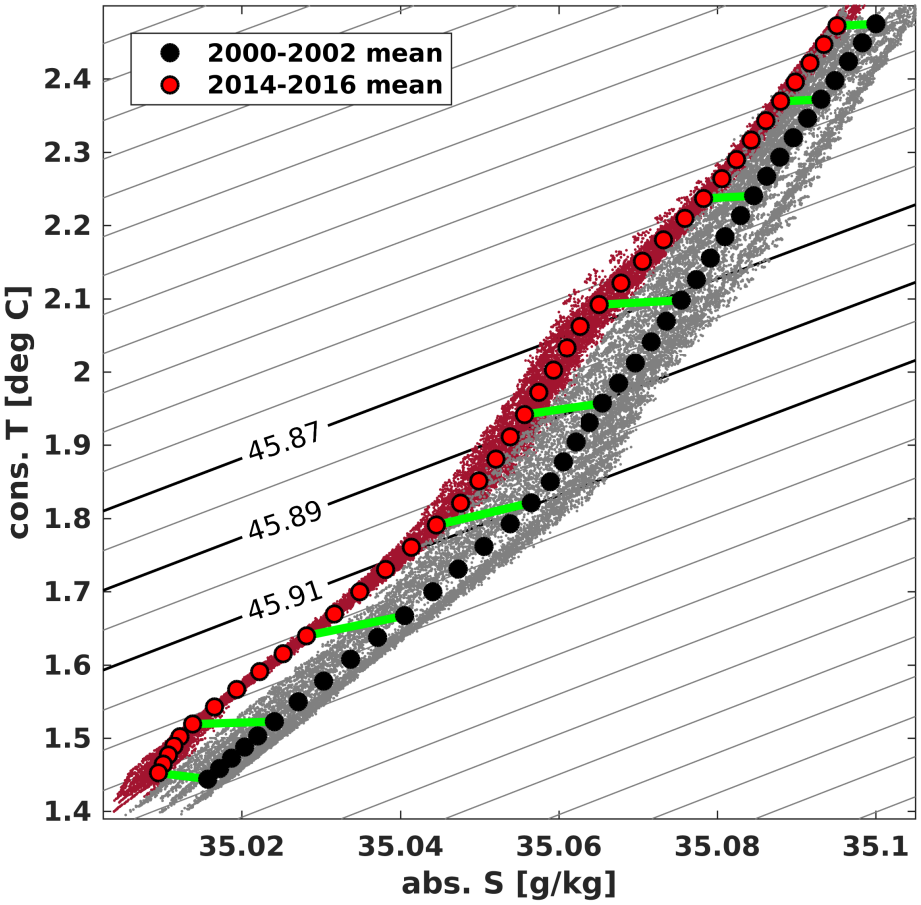

Figure 4.9: Temperature-salinity (T/S) plot for MOVE 1 data below 3000 dbar. Points in the background show daily values in the 2000–2002 (black) and 2014–2016 (red) periods every 50 dbar, and larger symbols show mean values for the two periods. Green lines connect values at the same depths every 250 dbar.

found that adjustment to signals in the North Atlantic differs by region, with signals traveling at advective time scales in the subpolar gyre but propagating as Kelvin waves south of 34°N. The propagation time from the subpolar North Atlantic to the equator is typically on the order of months but can be several years in some models. *Marshall and Johnson* (2013) showed that this model dependency is related to the model parameters such as grid size. The few observational AMOC studies that have reported coherent signals to date have found propagation consistent with a wave-like signal propagation along the western boundary. *Elipot et al.* (2013) analyzed

bottom pressure data along the western boundary to find signals propagating at speeds between 1 m s^{-1} and 128 m s^{-1}, consistent with coastally trapped waves. *Frajka-Williams et al.* (2018) compared properties at the western boundary at MOVE and RAPID, and found high correlations between signals throughout the NADW layer at lags between 0 and 7 months, with RAPID leading. However, both of these studies focused on signals on shorter time scales, rather than the decadal variability that is the focus of this section.

Other model studies have found that meridional propagation of AMOC changes is related to advective processes, instead of waves. *Buckley et al.* (2012) suggested that decadal AMOC variability in their model is communicated southward along the western boundary in the subtropical gyre at an advective speed of about 2 cm s^{-1} in the Deep Western Boundary Current. Similarly, *Marotzke and Klinger* (2000) and *Han et al.* (2013) found that density anomalies that are formed in the North Atlantic can be exported by the DWBC. This mode of propagation is consistent with traditional hydrographic studies of North Atlantic Deep Water, which have relied on tracking signals in temperature, salinity (*Molinari et al.*, 1998; *van Sebille et al.*, 2011; *Le Bras et al.*, 2017), and chlorofluorocarbons (CFCs) (*Rhein et al.*, 2004; *LeBel et al.*, 2008; *Smith et al.*, 2016). A recent study used CFC measurements collected throughout the North Atlantic over the last decades to calculate spreading velocities along the path of NADW as it follows the Deep Western Boundary Current (*Rhein et al.*, 2015). They found that spreading velocities north of the equator were generally on the order of about $1-2$ cm s^{-1}.

If density anomalies were propagated along the western boundary by waves, the adjustment would occur through the vertical movement of isopycnals at each latitude (*Marshall and Johnson*, 2013). The T/S diagram in Figure 4.6 shows that this cannot explain the changes observed at MOVE 3: The properties at each depth move towards fresher values with almost constant temperature, and there is no evidence of isopycnal heave. The water mass changes observed therefore cannot be explained by the propagation of boundary waves, and must be caused by processes affecting the water mass properties upstream. This could be due to lateral

movement of water mass changing the water mass found at the mooring site, changing mixing rates with surrounding waters along the spreading path of the water mass, or variability in the source region. To investigate the first possibility, we compare the mean T/S properties from the two periods at MOVE 3 to climatological CTD data. The climatological data are taken from the World Ocean Atlas (*Levitus et al.*, 2013) in the western Atlantic Ocean between the equator and 50°N (Figure 4.10). While the initial curve lies within the cloud of properties found in the climatology, the 2014-2016 data are outside the T/S range of historical shipboard CTD data. This means that no water mass exists outside the source region in the western Atlantic Ocean that could explain the observed freshening by increased mixing with DSOW, or by replacing DSOW at the mooring site. The observed freshening could also be explained by instrument drift, but the careful calibration of the sensors (see methods section) ensures that this drift is minimized. The trend is further supported by shipboard CTD data taken at the beginning of the freshening trend, and several years after the end, shown as yellow lines in Figure 4.10.

Consequently, the only remaining explanation for the changes observed at MOVE 3 is the multi-decadal freshening trend in the source region (*Dickson et al.*, 2002; *van Aken and de Jong*, 2012). Our results suggest that these changes in salinity of the overflow waters cause a decrease in density (Figures 4.5, 4.7). This density trend in turn causes much of the variability in transport observed at MOVE, and particularly the strengthening between 2005 and 2015 (Figure 4.4b). The multi-decadal variability seen in Figure 4.3 is also controlled by changes at the eastern end of the section, at MOVE 1. These appear to also be related to water mass changes, although the source of the variability is less clear than at MOVE 3. The changes may in part be due to the same freshening of the overflows arriving with a time delay of several years, and somewhat smaller magnitude. Like for MOVE 3, the changes cannot be explained by variability related to waves (Figure 4.9). As noted in section 4.3.2, *van Aken and de Jong* (2012) reported a reversal of the multi-decade freshening trend in the Nordic Seas in the early 2000's, which appears to have arrived at MOVE in recent years. Deep salinities at MOVE 3 would thus be expected to keep

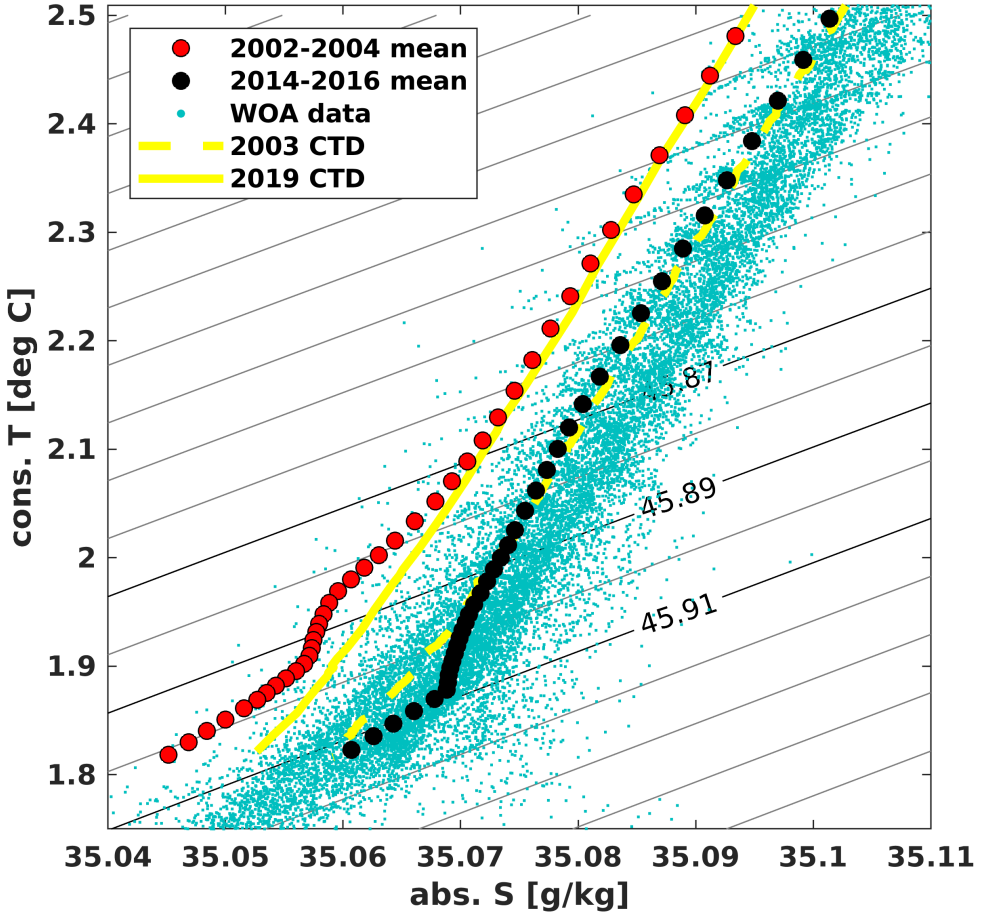

Figure 4.10: MOVE 3 mean T/S for the 2002-2004 (black) and 2014-2016 (red) periods, compared to climatological CTD data taken from the World Ocean Atlas (*Levitus et al.*, 2013) below 3000 m between North America and the Mid-Atlantic Ridge between the equator and 50°N (light blue dots). The data used are from the WOA2013 edition, which primarily uses data collected before 2010. Yellow lines show shipboard CTD profiles taken close to the mooring in 2003 and 2019.

increasing for the next decade. By itself, this change would lead to a decrease in the transport, but if density changes do propagate to the Mid-Atlantic Ridge as expected from idealized pathways (*Herrford et al.*, 2017), they would have an opposite effect on transport upon their arrival at the eastern mooring.

While AMOC variability is often linked to deep convection activity in the Labrador Sea (*Yashayaev and Loder*, 2016; *Jackson et al.*, 2016), representation of the overflow in models

has been shown to be crucial for both the mean state and variability of the AMOC, including on multi-decadal time scales (*Köhl and Stammer*, 2008; *Danabasoglu et al.*, 2010; *Zhang et al.*, 2011; *Lohmann et al.*, 2014). The cascading of dense waters over the sill in the Denmark Strait occurs over spatial scales that are too fine to be resolved by present day models, so that they must rely on parameterizations to represent the process. While some progress has been made in this area (*Legg et al.*, 2009; *Danabasoglu et al.*, 2010; *Wang et al.*, 2015), a recent review of AMOC theory noted that the impact of the overflows on its variability has not been explained in theoretical models yet (*Johnson et al.*, 2019). These shortcomings in representing the overflows may explain why advective propagation of signals such as those observed in the present study is not commonly found in models.

Observations of the subpolar North Atlantic have intensified recently with the inception of the OSNAP program (*Lozier et al.*, 2017). First results from the program suggest that variability in the Nordic Seas, rather than the Labrador Sea, is important for controlling AMOC variability (*Lozier et al.*, 2019; *Chafik and Rossby*, 2019). The results in the present study are consistent with this view, and provide evidence that density changes affect the southward transport of NADW far from the source region in the Nordic Seas.

4.4 MOVE and RAPID

Like MOVE, the RAPID/MOCHA/WBTS program at 26°N is designed to measure variability in the AMOC, doing so primarily with the use of density moorings (*McCarthy et al.*, 2015). However, the more extensive array that spans the entire basin, along with a mass conservation constraint, allows for estimation of both the upper and lower branch of the AMOC. In this section, we analyze only the lower branch comprised of southward NADW flow, comparing it with the NADW transport at MOVE.

The transport from the RAPID array is shown in Figure 4.11, along with the MOVE

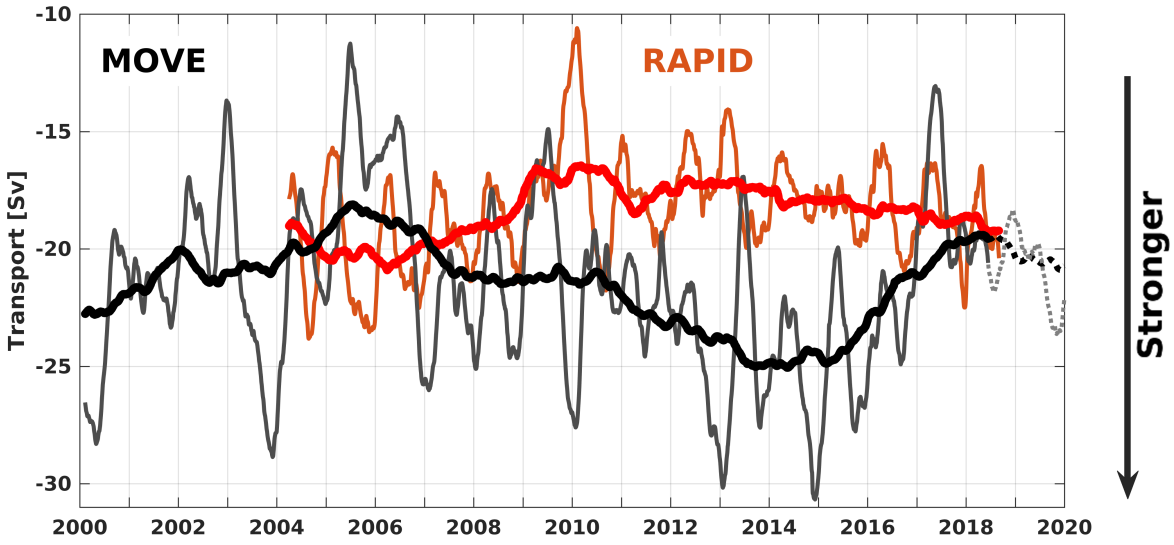

Figure 4.11: NADW transports from RAPID and MOVE calculated with the standard method for each project, filtered with 120-day running mean (thin lines) and 3-year running mean (thick lines). The MOVE time series is the same as shown in figure 4.3, and RAPID data are taken from *Smeed et al.* (2019). More negative values correspond to stronger transport.

transport. Transports at RAPID decreased until about 2010, with no statistically significant change after, leading *Smeed et al.* (2018) to conclude that the North Atlantic had entered a "state of reduced overturning". Thus, the sense of the transport change in the decade 2005-2015 is opposite to that at MOVE: RAPID transports weaken by about 3 Sv, while those at MOVE increase by 7 Sv. *Frajka-Williams et al.* (2018) suggested that the differences in transport are likely related to the different methods used for calculating them, as coherent signals would be expected from a wave-like propagation as proposed by *Zhang* (2010). However, based on the results from the previous section, periods of opposing low-frequency variability seem plausible. Signals related to advection of density anomalies from the source region, such as those observed at MOVE 3, would be expected to take several years to propagate from 26°N to 16°N. Indeed, property changes found at the western boundary at RAPID are comparable, and precede those at MOVE by a few years, with a similar shift of the T/S-profile towards fresher salinities (Figure 4.12). The RAPID project has several moorings at the western boundary, and time series of the two that are

available in the gridded dataset are shown here. The WB3 mooring is the westernmost full-depth mooring in the array, some 25 km from the boundary. Data from the West mooring are closer to the boundary, but come from different locations in different years (*McCarthy et al.*, 2015). Based on these two salinity time series, the propagation time scale to MOVE would be about 2-5 years, which is comparable to results from tracer studies (*Rhein et al.*, 2004).

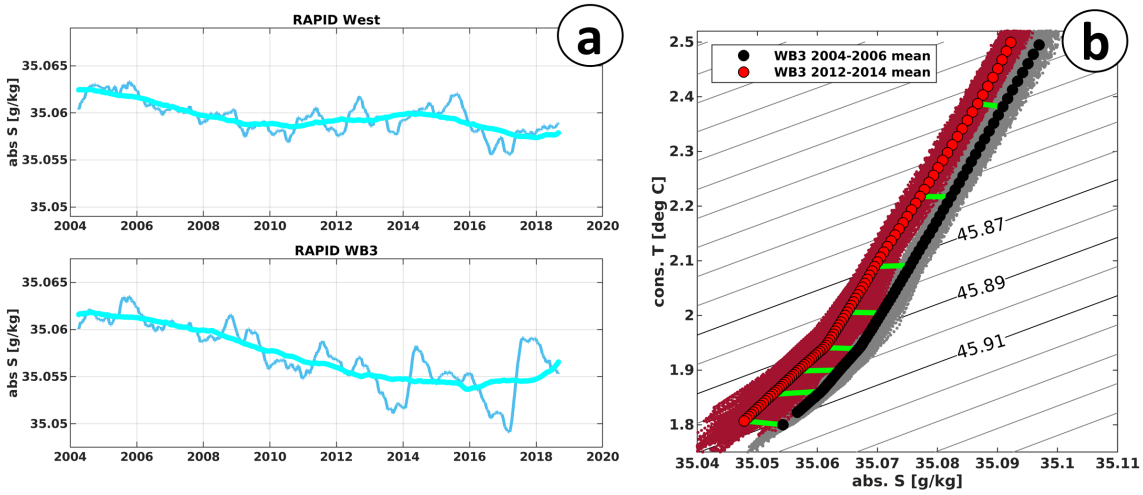

Figure 4.12: **a)** Salinity at 4500 dbar at the RAPID West and WB3 moorings. Vertical scale is stretched to be consistent with Figure 4.7. **b)** Same as Figure 4.6, but for RAPID WB3 data in 20 dbar bins for the 2004–2006 and 2012–2014 periods

Despite the similar property changes, the transport time series do not match the propagation time scale inferred from salinity changes. The minimum transport at MOVE precedes that observed at RAPID, suggesting that the phasing of the transport variability cannot be explained by a southward propagation of signals. Moreover, the transport divergence of the flow into and out of the box bounded by the two arrays that is implied by the transport difference would require a storage change of NADW, i.e. a change in its layer thickness (*Toole et al.*, 2017; *Yang*, 2015). The peak volume anomaly resulting from the transport divergence would be equivalent to a change in layer thickness of about 350m if distributed evenly over the entire western Atlantic. No signal of such magnitude can be found in hydrographic data, suggesting that storage changes are unlikely to explain the apparent transport divergence between the two sections. Consequently,

the differences between the two arrays are unlikely to be caused by a real divergence of the flow. The following sections will explore the possibility that the opposing variability of transports at MOVE and RAPID may be related to the methods used to determine the external transport, as suggested by *Frajka-Williams et al.* (2018).

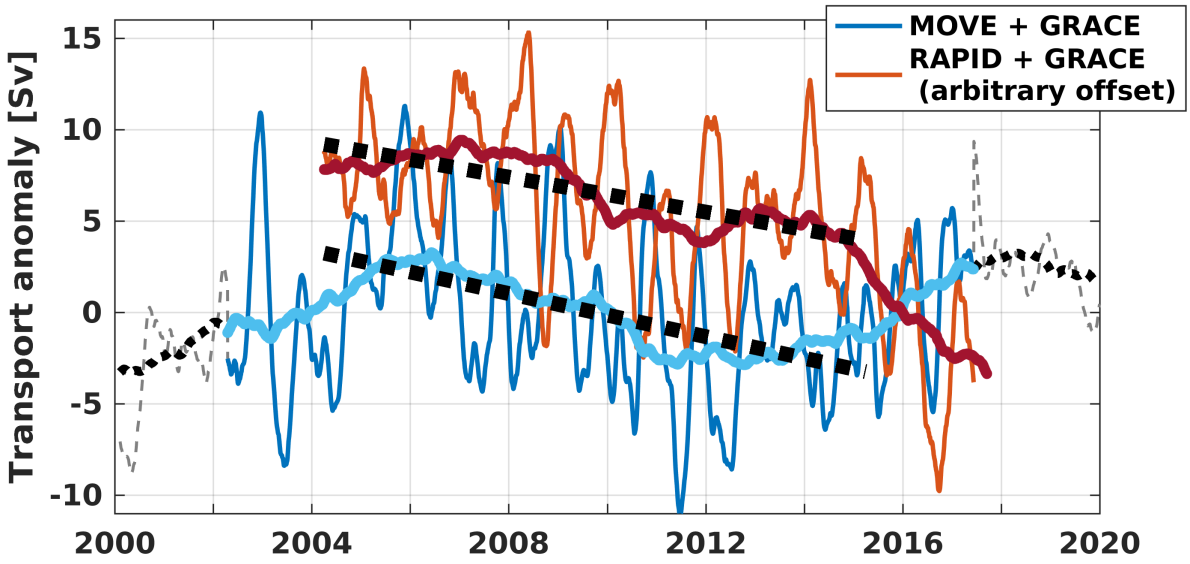

Figure 4.13: Western basin NADW transport anomalies from 16°N (MOVE, blue) and 26°N (RAPID, red), referenced to velocities from GRACE bottom pressure. RAPID time series is offset by 5 Sv for clarity. The MOVE time series is continued using the transports calculated without GRACE from Figure 4.3, shown as dashed lines. Negative anomalies correspond to stronger transport.

4.4.1 Transports referenced to GRACE

In order to more directly compare the two datasets, we derive NADW transports for both MOVE and RAPID using a method consistent with MOVE: the velocity shear is calculated for a section betweeen the western boundary mooring and the mooring located on the western flank of the Mid-Atlantic Ridge (see Figure 4.1 for the location). This reference level velocity calculated from GRACE data is then added to the vertically varying velocity profile, and the profile is integrated horizontally and vertically to provide a time series of absolute geostrophic transport

variability.

The time series of transports calculated in this fashion for MOVE and RAPID are shown in Figure 4.13, with the MOVE time series corresponding to the MOVE + GRACE estimate from Figure 4.3. Also shown is the linear trend over the period when the two time series from Figure 4.11 have opposing variability, 2004-2015. For the MOVE section at 16°N, the inclusion of GRACE does not substantially change the low-frequency variability, as was shown in section 4.3.1, with the trend decreasing from -0.91 ± 0.14 Sv/yr to -0.71 ± 0.59 Sv/yr. In contrast, the trend calculated for the western half of the RAPID section at 26°N with this method is -0.50 ± 0.38 Sv/yr compared to $+0.30 \pm 0.14$ Sv/yr for the full RAPID estimate, i.e. the trend is stronger and of the opposite sign. Thus, calculating the transport at the two arrays in the same fashion by combining data from the moorings and GRACE results in comparable trends at the two latitudes, which show a strengthening of southward NADW transport, in agreement with the trend from the regular MOVE calculation.

Figure 4.14 shows the vertical profile of the trend in transport per unit depth through the two sections, equivalent to the velocity profile multiplied by section width. For RAPID, the deep velocity trend from GRACE plays a larger part in the transport variability than at MOVE. Also shown in Figure 4.14 is the transport trend from the regular RAPID calculation as used by *McCarthy et al.* (2015) and *Smeed et al.* (2018), and also used in Figure 4.11. Unlike the two estimates calculated using GRACE data, the transport trend for RAPID using the mass conservation constraint is positive throughout most of the NADW layer, and values are largest near the reference level. Differences with the GRACE-referenced estimate could be explained by changes occuring in the eastern Atlantic, as the full RAPID section spans the entire width of the basin from Florida to Morocco. However, calculating the changes east of the Mid-Atlantic Ridge referenced to GRACE suggests that changes are much too small to reverse the trend (not shown).

The difference between the RAPID time series in Figures 4.11 and 4.13 largely comes from the reference velocity, which is derived from GRACE for Figure 4.13, but comes from a

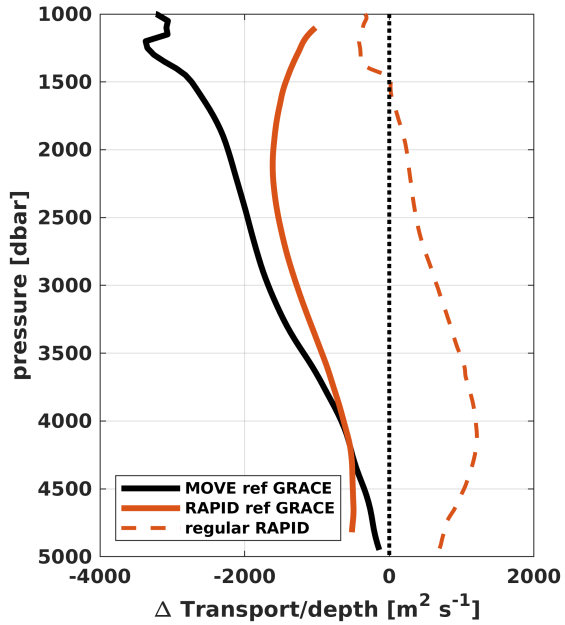

Figure 4.14: Vertical structure of decadal trend in transport, 2011-2015 mean minus 2004-2008 mean. Solid lines show transports referenced to GRACE as in Figure 4.13, and the dashed line shows the regular RAPID transport calculated with the mass conservation constraint, and plotted in Figure 4.11.

mass conservation constraint for the RAPID calculation. This is consistent with *Frajka-Williams et al.* (2018)'s findings that the different handling of the reference level is likely responsible for the differences between MOVE and RAPID. *Worthington et al.* (2019) compared the external transport from RAPID to that inferred from GRACE and found good agreement on time scales less than 10 years, but noted the large differences in the decadal trend, which they attributed to errors in the GRACE data. The most likely error source for transports inferred from GRACE is the relatively coarse resolution ($\sim$ 300 km), which could result in some of the variability being missed if bottom pressure anomalies are concentrated near the western boundary, as the spatial averaging would smooth the signal. If the ocean mass trends immediately adjacent to the western boundary at 26°N were about 17 mm less than the trend measured by GRACE near the boundary, the resulting external transport would reverse the sign of the trend in Figure 4.13, making it consistent with the regular RAPID estimate. However, as shown in *Koelling et al.*

(2020) (previous chapter), the trend in GRACE agrees well with that calculated using independent measurements. This includes data from the westernmost full-depth RAPID mooring *WB3*, which is only 25 km from the continental shelf (*McCarthy et al.*, 2015), where the trends agreed to within 3.4 mm/decade. Similarly, trends for the MOVE 3 mooring at the western boundary agreed to within 1 mm/decade with GRACE, much less than the change of about 10 mm/decade that would be required for the transport change to match the RAPID time series from Figure 4.11. For variability of transports referenced to GRACE at both 16°N and 26°N to agree with RAPID, there would have to be a bias of 10–20 mm/decade in the GRACE trend at the locations of both boundary moorings, which seems unlikely given the good agreement with altimetry-steric height measurements (*Koelling et al.*, 2020). Furthermore, analysis of bottom pressure recorders at 26°N showed a high correlation between the GRACE grid point closest to the western boundary and *in situ* bottom pressure measurements on shorter time scales (*Worthington et al.*, 2019).

While the spatial smoothing of GRACE could lead to errors near the boundary, comparison to these independent measurements suggests that it nonetheless captures most of the variability in the external transport. Consequently, there is no evidence that the opposite trend for the GRACE-referenced transport and the regular RAPID calculation can be attributed to errors in GRACE.

4.4.2 RAPID compensation term

The external transports from GRACE and RAPID are not straightforward to compare, as the GRACE reference velocity only applies to the deep reference level between the western boundary and the Mid-Atlantic Ridge. On the other hand, for the RAPID calculation, temperature and salinity data from moorings that are separated horizontally are stitched together in the vertical. The velocity shear is then calculated relative to 4820 dbar from these concatenated profiles, and a hyspometric[1] compensation term is applied at the 4820 dbar reference level to close the mass

[1] *hypsometric* in this case refers to a quantity that varies based on the width of the basin at each depth

budget (*McCarthy et al.*, 2015). In reality, the stitching of the mooring results in eleven different implicit reference levels where the velocity is unknown, shown schematically in Figure 4.15. Due to the different depths of these levels, there will be a depth dependence to the true compensation term, which is not considered in the RAPID calculation. There are also areas that are not covered by the section, so-called bottom triangles, at the western and eastern boundaries, and over the Mid-Atlantic Ridge, which likewise are implicitly included in the compensation term. The method has been validated previously against models (*Baehr et al.*, 2009), and the array itself is based on a design study using model data (*Hirschi et al.*, 2003), but the models used initially did not have sufficient resolution to realistically simulate the mooring setup. Despite all the assumptions made in the RAPID calculation, the transport variability seems to be captured well by the method: *Sinha et al.* (2018) used a higher-resolution model to systematically analyze the biases resulting from the different reference levels and unsampled regions, as well as ageostrophic terms, and found that while there are biases in the mean structure, the variability is well represented by the method.

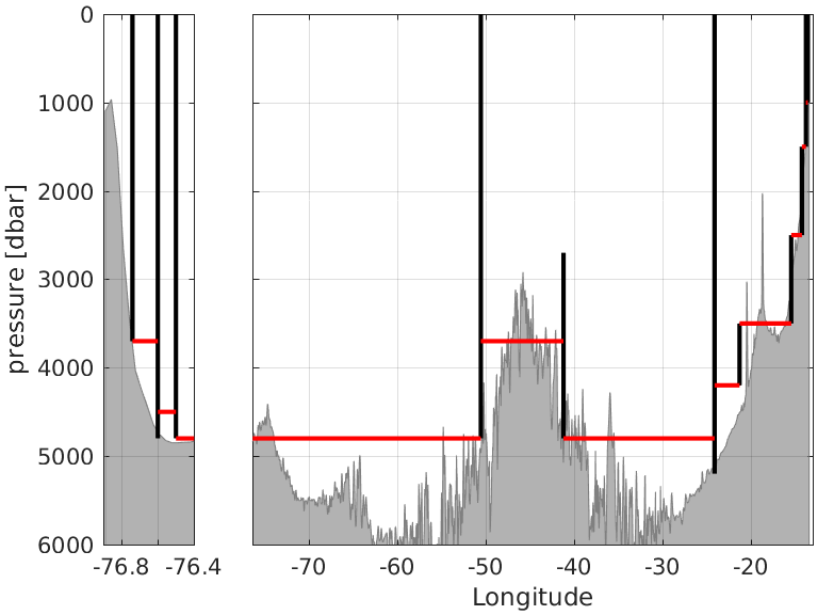

Figure 4.15: RAPID moorings (black), and reference levels implicitly used in the calculation (red). Gray shading shows topography.

Trends calculated for RAPID using the mass conservation constraint are also supported by several independent measurements: At 41°N, the AMOC has been calculated using Argo data (*Willis*, 2010), with long-term trends that are similar to RAPID (*Baringer et al.*, 2018). The weakening of the AMOC observed by RAPID is also consistent with observations of long-term changes in air-sea heat exchange (*Bryden et al.*, 2020), and of spatial fingerprints of surface temperature variability which resemble those found in model studies (*Smeed et al.*, 2018). While all of these studies focus on changes to the surface branch of the AMOC and related effects on climate, the southward flow of NADW is highly anti-correlated with the 0-1000m transport (*McCarthy et al.*, 2015), so variability in the lower branch would be expected to be similar.

4.4.3 Reconstructing RAPID transport using a shallow reference level

The vertical structure of transport changes in the RAPID calculation has a zero crossing at about 1750 dbar (Figure 4.14, dashed line), suggesting that variability at this depth may be less important. We therefore evaluate the use of this depth as a reference level at 26°N, using thermal wind (equation 4.1) to calculate velocity shear relative to 1750 dbar for the full transbasin section. Two-year means for the transport calculated this way are shown in the right panel of Figure 4.16, compared to changes from the regular RAPID calculation in the left panel.

The transport changes are generally consistent, with less variability in the Labrador Sea Water layer, and the spread being larger towards the bottom, indicative of larger low-frequency variability in the overflow waters (*Frajka-Williams et al.*, 2016). This is different from the situation at MOVE, where the transport is most affected by density changes in the overflows (section 4.3.2), but the resulting *velocity* changes are largest for Labrador Sea Water (Figure 4.2). Figure 4.17 shows the time series of transport in the NADW layer at 26°N calculated with thermal wind relative to 1750 dbar, compared to the regular RAPID transport. While the subannual variability does not match, the longer-term changes that are of interest in this study appear to be well-represented. The 1750 dbar depth is where the maximum velocity associated

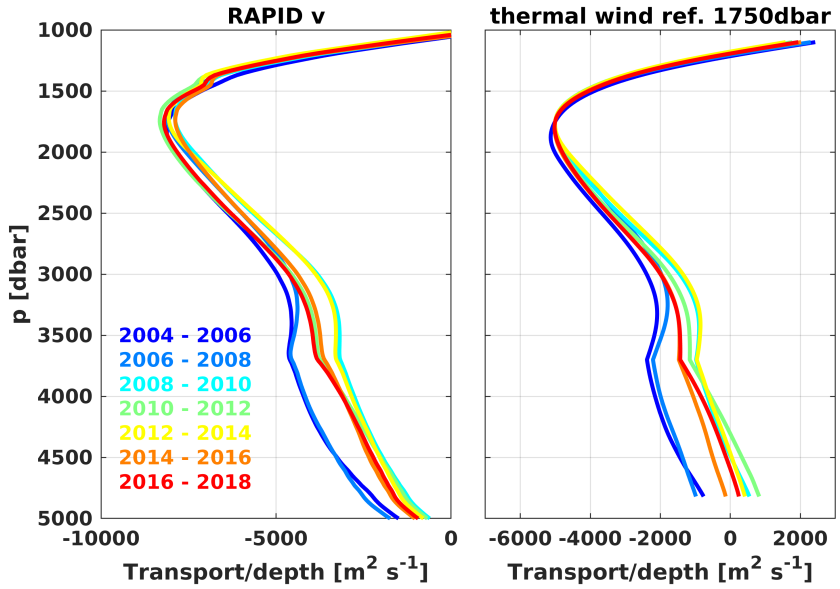

Figure 4.16: 2-year mean profiles of transport through the RAPID section. **Left:** RAPID calculation. **Right:** Thermal wind from RAPID moorings for the entire section relative to 1750 dbar, with time-mean values at 4820 dbar subtracted.

with the Labrador Sea Water layer occurs, so that referencing to this depth suppresses almost all variability in this layer. Therefore, the good agreement with the regular RAPID time series would imply that transport variability of LSW is not important for variability of NADW transport on decadal time scales. In other words, it implies that in the normal RAPID calculation, the mass conservation constraint cancels out the transport variability in the LSW layer. If the transport at MOVE is calculated the same way, a weakening of NADW can also be observed initially which is comparable to that at RAPID, and followed by a stronger increase. Again, transport changes are broadly consistent between the two arrays when using a comparable method.

4.4.4 MOVE & RAPID: Discussion

Overall, the different handling of the reference level seems to be responsible for the differences in low-frequency variability between MOVE and RAPID transports calculated with the standard method for each array (Figure 4.11). A similar conclusion was drawn by *Frajka-*

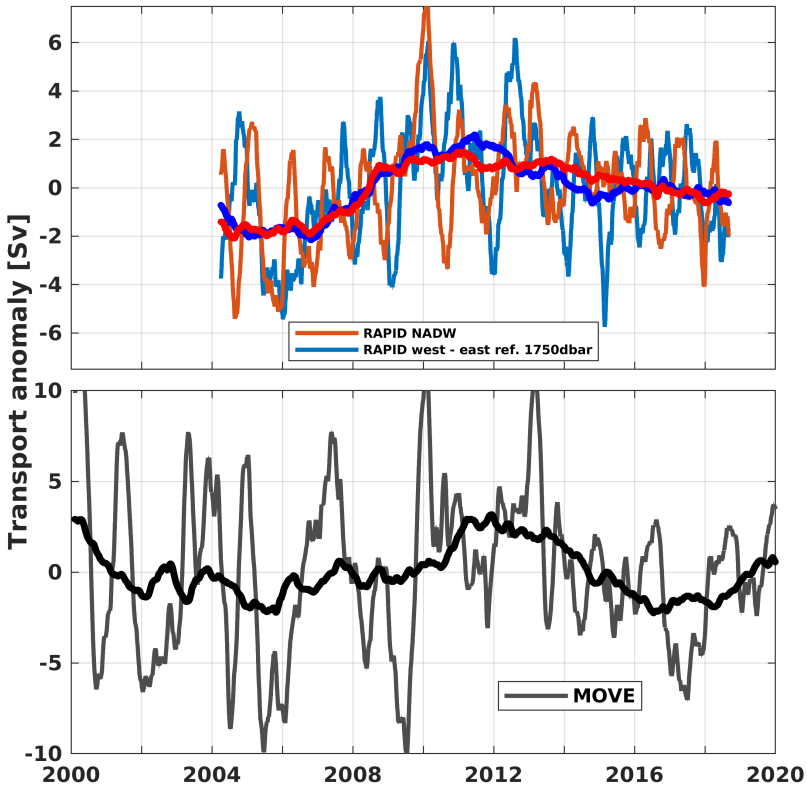

Figure 4.17: **Top panel:** Transport through the RAPID section from the normal RAPID calculation (red lines), and from thermal wind relative to 1750 dbar (blue). **Bottom panel:** Transport through the MOVE section relative to 1850 dbar (depth of LSW maximum at MOVE). In both panels, more negative values mean stronger transport.

Williams et al. (2018), but was based mostly on a comparison of the two western boundary moorings. Here, we have extended the analysis to derive NADW transport time series that give comparable results at the two latitudes: Transports calculated at 16°N and 26°N from density measurements referenced to GRACE agree with the regular MOVE estimate, showing a strengthening of NADW transport between 2005 and 2014. If the transport at 26°N is calculated from thermal wind relative to 1750 dbar, transport variability is similar to the full RAPID estimate using the mass conservation constraint, and the transport calculated in the same fashion at MOVE is broadly consistent.

Looking at the transport differences between MOVE and RAPID in the context of the

deep ocean property and density changes discussed in section 4.3.2, they can be interpreted as resulting from different assumptions about how those density changes affect ocean mass. For the MOVE calculation, the decreasing density at the western boundary leads to an increase in transport, as variability in the reference velocity is neglected. Thus, the change in density is assumed to have no effect on ocean mass, implying a stretching of the overflow water layer in response to the density changes. For RAPID, the property changes at the western boundary are similar (Figure 4.12), but the external transport inferred from the compensation term leads to a decrease in the reference level velocity. This could be explained by the density changes acting over a layer of constant thickness, which would result in a decrease in ocean mass at the western boundary. Figure 4.18 shows schematically how density changes in the deep ocean can be interpreted as either an increasing transport with the maximum change in the LSW layer, or a decrease with the largest change in the overflow waters, with explanations given in the caption. Note that, since property changes seem to originate in the Nordic Seas (section 4.3.2), the two cases shown in the schematic refer to changes occurring there and subsequently propagating to the two mooring sites.

Case 1 is comparable to the changes for MOVE, with southward velocities increasing from the bottom, and maximum trends in the LSW layer. This is supported by measurements from GRACE, which were validated against independent data in *Koelling et al.* (2020), and show no evidence of an ocean mass decrease at the western boundary that would be associated with the density changes in case 2. In fact *Koelling et al.* (2020) showed that ocean mass in the Atlantic Ocean seems to increase the most where the time-mean DSOW layer is thickest, opposite to what would be expected from a decrease in ocean mass associated with density changes in case 2.

Conversely, case 2 is consistent with the weakening NADW transport peaking in the overflow water layer as inferred from the RAPID calculation with the mass conservation constraint. This is also similar to changes observed for the boundary current at the exit of the Labrador Sea at 53°N, where *Zantopp et al.* (2017) found that decadal variability is most pronounced

in the overflow waters, and smaller in the LSW layer. Moreover, an increase in southward NADW transport at RAPID as suggested by the GRACE-referenced time series in Figure 4.13 and case 1 would violate the mass conservation principle, as northward flow in the upper AMOC is weakening (*McCarthy et al.*, 2015). This weakening of the upper limb is consistent with observed large-scale patterns in the ocean (*Smeed et al.*, 2018; *Bryden et al.*, 2020), and has been reproduced successfully in ocean reanalyses (*Jackson et al.*, 2016) and climate models (*Msadek et al.*, 2013; *Xu et al.*, 2014; *Blaker et al.*, 2015).

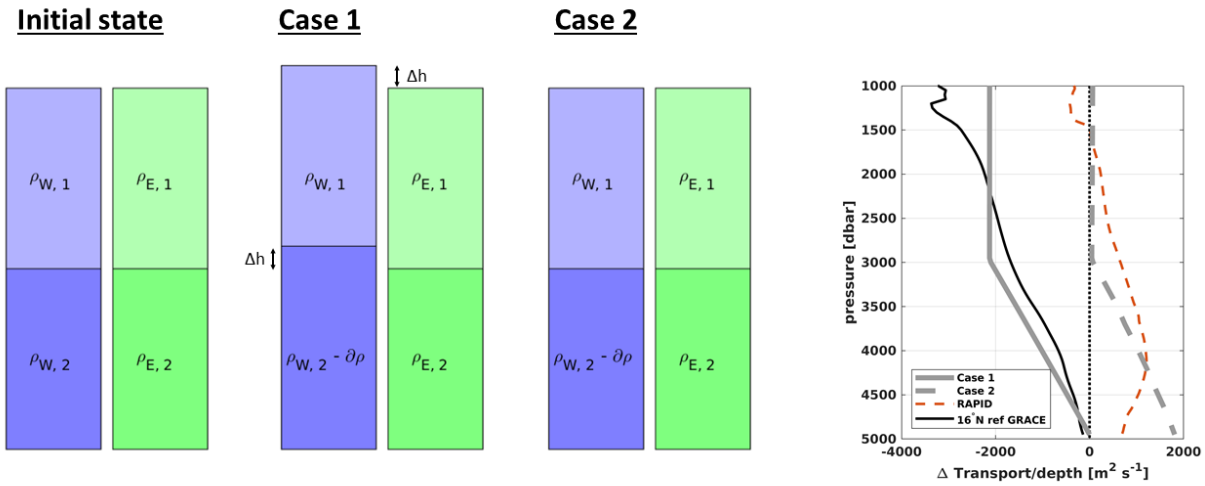

Figure 4.18: Idealized schematic of two different explanations for how water mass changes at the western boundary affect transport, assuming constant properties at the eastern end of the section and in the upper layer. The two layers represent the upper (LSW) and lower (overflow waters) NADW layers. The transport profiles in the right panel compare these idealized changes with the actual trend for the MOVE and RAPID arrays.
Case 1: Density of overflow waters decreases, but there is no change in ocean mass. Thus, the density change must be compensated by an expansion of the layer by Δh, on the order of a few cm. This pushes up the overlying Labrador Sea Water, leading to a tilt in the upper interface, and a constant negative (strengthening) velocity anomaly in the LSW layer, which decreases to zero throughout the overflow water layer.
Case 2: Density of overflow waters decreases, with a constant layer thickness. The mass of the water column, and hence bottom pressure, decreases, resulting in a northward anomaly in the overflow water layer that increases towards the bottom.

Given the high-latitude source of the density changes, it is unlikely that the effect on transport would follow case 1 for MOVE and case 2 for RAPID, but it is not clear from the data

and other available measurements which one is the more plausible scenario. More work will be needed to fully demystify the differences between the MOVE and RAPID time series, and understand them in the context of AMOC coherence across latitudes. These questions would be most easily addressed in a model, but the deep ocean property changes that appear to drive the transport variability at MOVE are not generally represented in present-day ocean models. As a result, any ocean mass change that may be associated with the decreasing density would also not be found in these models, making it difficult to draw meaningful conclusions on the two observing methods. A dedicated model study comparing the two arrays will likely be needed to explain the differences, and should include realistic variability in the Nordic Seas.

4.5 Summary

In this study, we have analyzed the transport of North Atlantic Deep Water through a section between Guadeloupe and the Mid-Atlantic Ridge at 16°N. In the regular MOVE calculation, the transport is calculated from the velocity shear inferred from density data, together with direct measurements from current meters over the western boundary slope, ignoring the external transport component (see section 4.2.2). The resulting transport time series exhibits multi-decadal variability with a time scale of 15-20 years and peak-to-peak amplitude of 7 Sv. Including the external transport component, calculated from GRACE satellite data, does not substantially change this low-frequency variability (Figure 4.3), suggesting that changes are largely driven by the density gradient. Analysis of the density changes shows that they cannot be explained by propagation of waves, as is often suggested by theoretical studies and numerical models. Instead, most of the decrease in density responsible for the transport variability appears to be driven by salinity changes in the overflow water masses formed in the Nordic Seas. This suggests that variability in density in the Nordic Seas, which is ultimately controlled by surface forcing in the subpolar North Atlantic, is crucial for setting the southward export of NADW,

affecting the transport far from the source region.

In section 4.4, we compared the transport through the MOVE transect to that measured as part of the RAPID array at 26°N. The transport calculated from the two standard methods for the different observing systems shows a large transport divergence, which would require an increase in NADW layer thickness that is not supported by observations. The variability in transport calculated from the same method as at MOVE, using GRACE to infer the external transport, is comparable to the MOVE estimate over much of the common period. Conversely, the RAPID trend can be recovered at 26°N, and to a lesser extent at 16°N, by calculating transport relative to a reference level at 1750 dbar, in the core of the Labrador Sea Water layer. The difference therefore appears to be an artefact related to how the external transport is calculated, which can be thought of as different assumptions about how water mass changes affect bottom pressure (Figure 4.18). However, more work is necessary to determine which of the methods is more representative of the actual transport.

4.6 Acknowledgments

JK was supported by NASA Headquarters under the NASA Earth and Space Science Fellowship Program (Grant NNX16AO39H). MOVE is presently supported by NOAA OOMD under award NA15OAR4320071. MOVE was previously supported by the German BMBF. MOVE data are freely available through OceanSITES. Data from the RAPID-WATCH MOC monitoring project are funded by NERC (UK) and are freely available from www.rapid.ac.uk/rapidmoc. GRACE ocean data are available at http://grace.jpl.nasa.gov, supported by the NASA MEaSUREs Program.

Chapter 4, in part, is being prepared for submission for publication of the material. Koelling, J.; Send, U.; Lankhorst, M. The dissertation author was the primary investigator and author of this material.

Summary and Outlook

Over the course of this dissertation, I have studied several aspects of the formation, export, and circulation of North Atlantic Deep Water. As with any problem worth studying, the results of this work, while providing some new insight, also raise a number of questions that would be interesting to address in future projects.

Chapter 1 shows that there is substantial oxygen uptake during wintertime convection in the Labrador Sea, associated with injection of air bubbles. A more recent study builds on these results to look at both oxygen and carbon uptake over a full annual cycle, and showed that there is much larger uptake of oxygen, as well as Atmospheric Potential Oxygen (APO), than would be predicted from most climate models (*Atamanchuk et al.*, 2020). Our results show that the uptake appears to be higher during the 2014/15 winter, which featured strong convection (*Yashayaev and Loder*, 2016), compared to earlier results from a year with less convective activity. However, data from more than just a few years will be needed to ascertain that this connection is robust, so a logical next step would be to maintain observations of oxygen content and uptake for an extended period of time. Additionally, the connection between convection and oxygen uptake may not necessarily be just a causal relationship, with deeper convection being directly responsible for stronger gas exchange: Both processes are driven in part by atmospheric forcing, with more extreme winds leading to stronger ocean heat loss and oxygen uptake. While it has been shown that surface saturation varies in concert with convection depth (*Wolf et al.*, 2018), which would drive increased uptake, more targeted process studies will be needed to disambiguate

the contribution of these different processes to gas exchange.

Another aspect of the work from Chapter 1 that warrants closer attention is the exchange of properties between the interior of the Labrador Sea and the boundary current. The study used a relatively crude estimate using mean properties from both regions, and arrived at an estimate of the lateral exchange of oxygen, $F_{\mathrm{lat}}(O_2)$, of -2.9 ± 1.5 mol m^{-2}, for 5 months in winter. A comparable rate of lateral exchange was also found by *Wolf et al.* (2018), using a similar approach based on mean water mass properties. Chapter 2 builds on these simple estimates, using time-varying properties and exchange rate α to estimate F_{lat} for oxygen, as well as carbon and nitrate. Unlike the previous chapter, this work focused on the upper ocean and the summer months, which is the time period most relevant for carbon sequestration associated with biological production. The results showed that the lateral exchange is an important part of the budget for carbon and nitrate. This is particularly true for the depth range just below the mixed layer, where respiration rates are underestimated by up to 50% when ignoring the contribution of F_{lat}. This work is part of an effort to resolve these budgets during the productive season in order to determine Net Community Production (NCP), which is lead by D. Atamanchuk at Dalhousie University, and I will continue contributing to this project during my postdoctoral research. A limitation of the current data set is that due to the sparse sampling, the estimates of F_{lat} use data from different years. In addition, the boundary current data used are from different locations, and in the case of carbon, we rely on a salinity-based estimate below the mixed layer. This could be improved on in the future if contemporaneous measurements from both regions become available, and data from the full water column would help to extend the analysis through a full annual cycle including the convective season.

In Chapter 3, I used ocean mass data from the GRACE satellite mission to study circulation changes in the Atlantic Ocean. The first part of this chapter deals with the validation of decadal trends in the data, which had previously been assumed to be unreliable (*Landerer et al.*, 2015; *Worthington et al.*, 2019). Comparison of the GRACE trend with ocean mass changes estimated

from altimetry and density measurements from a number of mooring and hydrography sites in the North Atlantic shows good agreement, supporting the trend in GRACE. The data were then used to calculate changes in the geostrophic circulation of the deep ocean. The inferred changes show a large-scale counterclockwise circulation anomaly, with strengthening of the interior branch of NADW by about 10 Sv, which is balanced by weaker flow near the western boundary. As noted in section 3.4.3, the increase could be part of decadal-multidecadal variability, but longer sustained measurements, such as the GRACE follow-on mission, will be necessary to evaluate whether this is the case. Another interesting aspect to investigate further in the future is the seasonal cycle of the two branches of NADW, as shown in Figure 3.8. Unlike the decadal changes, this part of the system could be validated and studied in more detail with a number of well-placed *in situ* bottom pressure recorders. The validation of the decadal trends in this work focused on the North Atlantic, motivated both by my personal interest in the region, and the paucity of sustained, high-accuracy mooring deployments elsewhere in the ocean. Future satellite missions aimed at measuring ocean mass and sea surface height could benefit from a more global network of long-term deep ocean mooring observations for better ground truthing; some efforts towards this are already underway in preparation for the SWOT satellite mission.

Finally, Chapter 4 discusses the multidecadal variability of NADW transport through a section at 16°N in the MOVE array. The 20-year time series of transport resolves about one full cycle of this low-frequency variability, comparable to time scales found in climate models. The variability seems to be driven by density changes in the Denmark Strait Overflow Water layer associated with a freshening of the water mass. This suggests that low-frequency variability in transport is controlled by density changes in the source region, which are propagated along the spreading path of NADW on advective time scales. Comparison of the MOVE transport with data from the RAPID array at 26°N suggests a large transport divergence between the two latitudes. However, this appears to be an artefeact related to how transports are calculated in the two projects: If transports at both latitudes are calculated for the western Atlantic, using

GRACE data to infer the reference level velocity, trends are consistent, and agree with the regular MOVE estimate. Conversely, referencing to an assumed level of no motion at about 1800 dbar results in transport variability comparable to that at RAPID. The available observations offer no satisfying explanation for this discrepancy, and the divergence between the two arrays implied by the time series in Figure 4.11 is difficult to reconcile with the basic laws of physics. Current generation climate models do not reproduce the density changes responsible for the MOVE transport variability, making them unsuitable for evaluating these differences. A model specifically forced with realistic high-latitude density variability could be useful in evaluating possible causes for the difference in transport variability measured at MOVE and RAPID. Another aspect that is worth investigating further is the dominant role of deep density changes associated with a freshening of the source water mass in controlling multidecadal transport variability at MOVE. This mechanism differs from the prevailing theory of variability in the Atlantic Meridional Overturning Circulation, which implicates boundary waves in propagating anomalies from the source region. However, some models do exhibit advective propagation of transport changes, and it would be instructive to re-evaluate these in the context of the observed transport variability.

Bibliography

Aagaard, K., J. H. Swift, and E. C. Carmack (1985), Thermohaline circulation in the Arctic Mediterranean Seas, *Journal of Geophysical Research: Oceans*, *90*(C3), 4833–4846, doi: 10.1029/JC090iC03p04833.

Ablain, M., A. Cazenave, G. Larnicol, M. Balmaseda, P. Cipollini, Y. Faugère, M. J. Fernandes, O. Henry, J. A. Johannessen, P. Knudsen, O. Andersen, J. Legeais, B. Meyssignac, N. Picot, M. Roca, S. Rudenko, M. G. Scharffenberg, D. Stammer, G. Timms, and J. Benveniste (2015), Improved sea level record over the satellite altimetry era (1993-2010) from the Climate Change Initiative project, *Ocean Science*, *11*(1), 67–82, doi: 10.5194/os-11-67-2015.

Andres, M. (2016), On the recent destabilization of the Gulf Stream path downstream of Cape Hatteras, *Geophysical Research Letters*, *43*(18), 9836–9842, doi: 10.1002/2016GL069966.

Atamanchuk, D., J. Koelling, U. Send, and D. Wallace (2020), Rapid transfer of oxygen to the deep ocean mediated by bubbles, *Nature Geoscience*, pp. 1–6.

Atlas, R., R. N. Hoffman, J. Ardizzone, S. M. Leidner, J. C. Jusem, D. K. Smith, and D. Gombos (2011), A cross-calibrated, multiplatform ocean surface wind velocity product for meteorological and oceanographic applications, *Bulletin of the American Meteorological Society*, *92*, 157–174, doi: 10.1175/2010BAMS2946.1.

Avsic, T., J. Karstensen, U. Send, and J. Fischer (2006), Interannual variability of newly formed Labrador Sea Water from 1994 to 2005, *Geophysical Research Letters*, *33*, doi: 10.1029/2006GL026913.

Baehr, J., S. Cunningham, H. Haak, P. Heimbach, T. Kanzow, and J. Marotzke (2009), Observed and simulated daily variability of the meridional overturning circulation at 26.5N in the Atlantic, *Ocean Science*, *5*, 575–589.

Baringer, M. O., J. Willis, D. A. Smeed, B. Moat, S. Dong, W. R. Hobbs, R. D., W. E. Johns, G. Gonil, M. Lankhorst, and U. Send (2018), Meridional overturning and oceanic heat transport circulation observations in the North Atlantic Ocean, in *State of the Climate in 2017*, vol. 99, pp. S91–S94, doi: 10.1175/2018BAMSStateoftheClimate.1.

Benson, B. B., and D. Krause (1984), The concentration and isotopic fractionation of oxygen dissolved in freshwater and seawater in equilibrium with the atmosphere, *Limnology and Oceanography*, *29*, 620–632, doi: 10.4319/lo.1984.29.3.0620.

Biastoch, A., C. W. Böning, and J. Lutjeharms (2008), Agulhas leakage dynamics affects decadal variability in Atlantic overturning circulation, *Nature*, *456*(7221), 489–492.

Billheimer, S., and L. D. Talley (2013), Near cessation of Eighteen Degree Water renewal in the western North Atlantic in the warm winter of 2011–2012, *Journal of Geophysical Research: Oceans*, *118*(12), 6838–6853.

Billheimer, S., and L. D. Talley (2016), Extraordinarily weak Eighteen Degree Water production concurs with strongly positive North Atlantic Oscillation in late winter 2014/15, in *State of the Climate in 2015*, vol. 97, pp. S78–S79, doi: 10.1175/2016BAMSStateoftheClimate.1.

Bittig, H. C., B. Fiedler, T. Steinhoff, and A. Körtzinger (2012), A novel electrochemical calibration setup for oxygen sensors and its use for the stability assessment of Aanderaa optodes, *Limnology and Oceanography: Methods*, *10*, 921–933, doi: 10.4319/lom.2012.10.921.

Bittig, H. C., B. Fiedler, R. Scholz, G. Krahmann, and A. Körtzinger (2014), Time response of oxygen optodes on profiling platforms and its dependence on flow speed and temperature, *Limnology and Oceanography: Methods*, *12*, 617–636, doi: 10.4319/lom.2014.12.617.

Blaker, A. T., J. J.-M. Hirschi, G. McCarthy, B. Sinha, S. Taws, R. Marsh, A. Coward, and B. de Cuevas (2015), Historical analogues of the recent extreme minima observed in the Atlantic meridional overturning circulation at 26 N, *Climate dynamics*, *44*(1-2), 457–473.

Bower, A., S. Lozier, A. Biastoch, K. Drouin, N. Foukal, H. Furey, M. Lankhorst, S. Rühs, and S. Zou (2019), Lagrangian Views of the Pathways of the Atlantic Meridional Overturning Circulation, *Journal of Geophysical Research: Oceans*, *0*(ja), doi: 10.1029/2019JC015014.

Bower, A. S., M. S. Lozier, S. F. Gary, and C. W. Böning (2009), Interior pathways of the North Atlantic meridional overturning circulation, *Nature*, *459*(7244), 243, doi: 10.1038/nature07979.

Bryden, H. L., B. A. King, G. D. McCarthy, and E. L. McDonagh (2014), Impact of a 30% reduction in Atlantic meridional overturning during 2009-2010, *Ocean Science*, *10*(4), 683–691, doi: 10.5194/os-10-683-2014.

Bryden, H. L., W. E. Johns, B. A. King, G. McCarthy, E. L. McDonagh, B. I. Moat, and D. A. Smeed (2020), Reduction in Ocean Heat Transport at 26°N since 2008 Cools the Eastern Subpolar Gyre of the North Atlantic Ocean, *Journal of Climate*, *33*(5), 1677–1689, doi: 10.1175/JCLI-D-19-0323.1.

Buckley, M. W., and J. Marshall (2016), Observations, inferences, and mechanisms of the Atlantic Meridional Overturning Circulation: A review, *Reviews of Geophysics*, *54*(1), 5–63, doi: 10.1002/2015RG000493.

Buckley, M. W., D. Ferreira, J.-M. Campin, J. Marshall, and R. Tulloch (2012), On the relationship between decadal buoyancy anomalies and variability of the Atlantic meridional overturning circulation, *Journal of Climate*, *25*(23), 8009–8030.

Caesar, L., S. Rahmstorf, A. Robinson, G. Feulner, and V. Saba (2018), Observed fingerprint of a weakening Atlantic Ocean overturning circulation, *Nature*, *556*(7700), 191–196.

Carlson, J. (2002), Development of an Optimised Dissolved Oxygen Sensor for Oceanographic Profiling, *International Ocean Systems*, *6*, 20–21.

Cazenave, A., K. Dominh, S. Guinehut, E. Berthier, W. Llovel, G. Ramillien, M. Ablain, and G. Larnicol (2008), Sea level budget over 2003-2008: A reevaluation from GRACE space gravimetry, satellite altimetry and Argo, *Global and Planetary Change*, *65*(1-2), 83–88, doi: 10.1016/j.gloplacha.2008.10.004.

Chafik, L., and T. Rossby (2019), Volume, Heat, and Freshwater Divergences in the Subpolar North Atlantic Suggest the Nordic Seas as Key to the State of the Meridional Overturning Circulation, *Geophysical Research Letters*, *46*(9), 4799–4808, doi: 10.1029/2019GL082110.

Chambers, D. P., A. Cazenave, N. Champollion, H. Dieng, W. Llovel, R. Forsberg, K. von Schuckmann, and Y. Wada (2017), Evaluation of the Global Mean Sea Level Budget between 1993 and 2014, in *Integrative Study of the Mean Sea Level and Its Components*, vol. 38, pp. 315–333, Springer, doi: 10.1007/s10712-016-9381-3.

Chelton, D. B., J. C. Ries, B. J. Haines, and P. S. Callahan (2001), Chapter 1 Satellite Altimetry, *International Geophysics*, *69*, 1–ii, doi: 10.1016/S0074-6142(01)80146-7.

Chylek, P., C. K. Folland, H. A. Dijkstra, G. Lesins, and M. K. Dubey (2011), Ice-core data evidence for a prominent near 20 year time-scale of the Atlantic Multidecadal Oscillation, *Geophysical Research Letters*, *38*(13).

Clark, P. U., N. G. Pisias, T. F. Stocker, and A. J. Weaver (2002), The role of the thermohaline circulation in abrupt climate change, *Nature*, *415*(6874), 863–869.

Clarke, R. A., and A. R. Coote (1988), The Formation of Labrador Sea Water. Part III: The Evolution of Oxygen and Nutrient Concentration, *Journal of Physical Oceanography*, *18*, 469–480, doi: 10.1175/1520-0485(1988)018¡0469:TFOLSW¿2.0.CO;2.

Clarke, R. A., and J.-C. Gascard (1983), The Formation of Labrador Sea Water. Part I: Large-Scale Processes, *Journal of Physical Oceanography*, *13*, 1764–1778, doi: 10.1175/1520-0485(1983)013¡1764:TFOLSW¿2.0.CO;2.

Curry, R. G., and M. S. McCartney (2001), Ocean gyre circulation changes associated with the North Atlantic Oscillation, *Journal of Physical Oceanography*, *31*(12), 3374–3400, doi: 10.1175/1520-0485(2001)031¡3374:OGCCAW¿2.0.CO;2.

Curry, R. G., M. S. McCartney, and T. M. Joyce (1998), Oceanic transport of subpolar climate signals to mid-depth subtropical waters, *Nature*, *391*, 575–577, doi: 10.1038/35356.

Danabasoglu, G. (2008), On Multidecadal Variability of the Atlantic Meridional Overturning Circulation in the Community Climate System Model Version 3, *Journal of Climate*, *21*(21), 5524–5544, doi: 10.1175/2008JCLI2019.1.

Danabasoglu, G., W. G. Large, and B. P. Briegleb (2010), Climate impacts of parameterized Nordic Sea overflows, *Journal of Geophysical Research: Oceans*, *115*(C11), doi: 10.1029/2010JC006243.

D'Asaro, E. A., and C. McNeil (2013), Calibration and Stability of Oxygen Sensors on Autonomous Floats, *Journal of Atmospheric and Oceanic Technology*, *30*, 1896–1906, doi: 10.1175/JTECH-D-12-00222.1.

de Jong, M., A. Bower, and H. Furey (2014), Two Years of Observations of Warm-Core Anticyclones in the Labrador Sea and Their Seasonal Cycle in Heat and Salt Stratification, *J. Phys. Oceanography*, *44*, doi: 10.1175/JPO-D-13-070.1.

de Jong, M. F., A. S. Bower, and H. H. Furey (2016), Seasonal and Interannual Variations of Irminger Ring Formation and Boundary-Interior Heat Exchange in FLAME, *Journal of Physical Oceanography*, *46*, doi: 10.1175/JPO-D-15-0124.1.

Dee, D. P., S. M. Uppala, A. J. Simmons, P. Berrisford, P. Poli, S. Kobayashi, U. Andrae, M. A. Balmaseda, G. Balsamo, P. Bauer, P. Bechtold, A. C. M. Beljaars, L. van de Berg, J. Bidlot, N. Bormann, C. Delsol, R. Dragani, M. Fuentes, A. J. Geer, L. Haimberger, S. B. Healy, H. Hersbach, E. V. Hólm, L. Isaksen, P. Kållberg, M. Köhler, M. Matricardi, A. P. McNally, B. M. Monge-Sanz, J.-J. Morcrette, B.-K. Park, C. Peubey, P. de Rosnay, C. Tavolato, J.-N. Thépaut, and F. Vitart (2011), The ERA-Interim reanalysis: configuration and performance of the data assimilation system, *Quarterly Journal of the Royal Meteorological Society*, *137*, 553–597, doi: 10.1002/qj.828.

Deshayes, J., and C. Frankignoul (2005), Spectral Characteristics of the Response of the Meridional Overturning Circulation to Deep-Water Formation, *Journal of Physical Oceanography*, *35*(10), 1813–1825, doi: 10.1175/JPO2793.1.

Dickson, B., I. Yashayaev, J. Meincke, B. Turrell, S. Dye, and J. Holfort (2002), Rapid freshening of the deep North Atlantic Ocean over the past four decades, *Nature*, *416*(6883), 832–837.

Dijkstra, H. A., J. A. Saenz, and A. McC. Hogg (2014), Energetics of multidecadal Atlantic Ocean variability, *Journal of Climate*, *27*(20), 7874–7889.

Dufresne, J.-L., M.-A. Foujols, S. Denvil, O. Caubel, A.and Marti, O. Aumont, Y. Balkanski, S. Bekki, H. Bellenger, R. Benshila, S. Bony, L. Bopp, P. Braconnot, P. Brockmann, P. Cadule, F. Cheruy, F. Codron, A. Cozic, D. Cugnet, N. de Noblet, J.-P. Duvel, C. Ethé, L. Fairhead, T. Fichefet, S. Flavoni, P. Friedlingstein, J.-Y. Grandpeix, L. Guez, E. Guilyardi, D. Hauglustaine, F. Hourdin, A. Idelkadi, J. Ghattas, S. Joussaume, M. Kageyama, G. Krinner, S. Labetoulle, A. Lahellec, M.-P. Lefebvre, F. Lefevre, C. Levy, Z. X. Li, J. Lloyd, F. Lott, G. Madec, M. Mancip, M. Marchand, S. Masson, Y. Meurdesoif, J. Mignot, I. Musat, S. Parouty, J. Polcher, C. Rio, M. Schulz, D. Swingedouw, S. Szopa, C. Talandier, P. Terray, N. Viovy, and N. Vuichard (2013), Climate change projections using the IPSL-CM5 Earth System Model: from CMIP3 to CMIP5, *Climate Dynamics*, *40*, 2123–2165, doi: 10.1007/s00382-012-1636-1.

Dunne, J. P., J. G. John, E. Shevliakova, R. J. Stouffer, J. P. Krasting, S. L. Malyshev, P. C. D. Milly, L. T. Sentman, A. J. Adcroft, W. Cooke, K. A. Dunne, S. M. Griffies, R. W. Hallberg, M. J. Harrison, H. Levy, A. T. Wittenberg, P. J. Phillips, and N. Zadeh (2013), GFDL's ESM2 Global Coupled Climate-Carbon Earth System Models. Part II: Carbon System Formulation and Baseline Simulation Characteristics, *Journal of Climate*, *26*, 2247–2267, doi: 10.1175/JCLI-D-12-00150.1.

Eden, C., and C. Böning (2002), Sources of Eddy Kinetic Energy in the Labrador Sea, *J. Phys. Oceanography*, *32*, doi: 10.1175/1520-0485(2002)032¡3346:SOEKEI¿2.0.CO;2.

Elipot, S., C. Hughes, S. Olhede, and J. Toole (2013), Coherence of Western Boundary Pressure at the RAPID WAVE Array: Boundary Wave Adjustments or Deep Western Boundary Current Advection?, *Journal of Physical Oceanography*, *43*(4), 744–765, doi: 10.1175/JPO-D-12-067.1.

Emerson, S., and S. Bushinsky (2016), The role of bubbles during air-sea gas exchange, *Journal of Geophysical Research: Oceans*, *121*, 4360–4376, doi: 10.1002/2016JC011744.

Frajka-Williams, E., and P. B. Rhines (2010), Physical controls and interannual variability of the Labrador Sea spring phytoplankton bloom in distinct regions, *Deep Sea Research Part I: Oceanographic Research Papers*, *57*, 541 – 552, doi: 10.1016/j.dsr.2010.01.003.

Frajka-Williams, E., C. S. Meinen, W. E. Johns, D. A. Smeed, A. Duchez, A. J. Lawrence, D. A. Cuthbertson, G. D. McCarthy, H. L. Bryden, M. O. Baringer, et al. (2016), Compensation between meridional flow components of the Atlantic MOC at 26°N, *Ocean Science*, *12*(2), 481–493, doi: 10.5194/os-12-481-2016.

Frajka-Williams, E., M. Lankhorst, J. Koelling, and U. Send (2018), Coherent circulation changes in the deep north atlantic from 16°N and 26°N transport arrays, *Journal of Geophysical Research: Oceans*, *123*(5), 3427–3443, doi: 10.1029/2018JC013949.

Frajka-Williams, E., I. J. Ansorge, J. Baehr, H. L. Bryden, M. P. Chidichimo, S. A. Cunningham, G. Danabasoglu, S. Dong, K. A. Donohue, S. Elipot, P. Heimbach, N. P. Holliday, R. Hummels, L. C. Jackson, J. Karstensen, M. Lankhorst, I. A. Le Bras, M. S. Lozier, E. L. McDonagh, C. S. Meinen, H. Mercier, B. I. Moat, R. C. Perez, C. G. Piecuch, M. Rhein, M. A. Srokosz, K. E. Trenberth, S. Bacon, G. Forget, G. Goni, D. Kieke, J. Koelling, T. Lamont, G. D. McCarthy, C. Mertens, U. Send, D. A. Smeed, S. Speich, M. van den Berg, D. Volkov, and C. Wilson (2019), Atlantic Meridional Overturning Circulation: Observed Transport and Variability, *Frontiers in Marine Science*, *6*, 260, doi: 10.3389/fmars.2019.00260.

Frankcombe, L. M., A. Von Der Heydt, and H. A. Dijkstra (2010), North Atlantic multidecadal climate variability: an investigation of dominant time scales and processes, *Journal of climate*, *23*(13), 3626–3638.

Friedrichs, M. A. M., M. S. McCartney, and M. M. Hall (1994), Hemispheric asymmetry of deep water transport modes in the western Atlantic, *Journal of Geophysical Research: Oceans*, *99*(C12), 25,165–25,179, doi: 10.1029/94JC02087.

Garcia, H. E., and L. I. Gordon (1992), Oxygen solubility in seawater: Better fitting equations, *Limnology and Oceanography*, *37*, 1307–1312, doi: 10.4319/lo.1992.37.6.1307.

Gary, S. F., M. Susan Lozier, C. W. Böning, and A. Biastoch (2011), Deciphering the pathways for the deep limb of the Meridional Overturning Circulation, *Deep Sea Research Part II: Topical Studies in Oceanography*, *58*(17-18), 1781–1797, doi: 10.1016/J.DSR2.2010.10.059.

Getzlaff, K., C. W. Böning, and J. Dengg (2006), Lagrangian perspectives of deep water export from the subpolar North Atlantic, *Geophysical Research Letters*, *33*(21), doi: 10.1029/2006GL026470.

Gruber, N., S. Doney, S. Emerson, D. Gilbert, T. Kobayashi, A. Körtzinger, G. C. Johnson, K. S. Johnson, S. C. Riser, and O. Ulloa (2010), Adding oxygen to Argo: Developing a global in-situ observatory for ocean deoxygenation and biogeochemistry, *Proceedings of OceanObs*, *9*, doi: 10.5270/OceanObs09.cwp.39.

Guo, J. Y., X. J. Duan, and C. K. Shum (2010), Non-isotropic Gaussian smoothing and leakage reduction for determining mass changes over land and ocean using GRACE data, *Geophysical Journal International*, *181*(1), 290–302, doi: 10.1111/j.1365-246X.2010.04534.x.

Han, M., I. Kamenkovich, T. Radko, and W. E. Johns (2013), Relationship between AirSea Density Flux and Isopycnal Meridional Overturning Circulation in a Warming Climate, *Journal of Climate*, *26*(8), 2683–2699, doi: 10.1175/JCLI-D-11-00682.1.

Harrison, W. G., and W. K. W. Li (2007), Phytoplankton growth and regulation in the Labrador Sea: light and nutrient limitation, *Journal of Northwest Atlantic Fisheries Science*, *39*, 71–82.

Harrison, W. G., K. Y. Børsheim, W. K. W. Li, G. L. Maillet, P. Pepin, E. Sakshaug, M. D. Skogen, and P. A. Yeats (2013), Phytoplankton production and growth regulation in the Subarctic North Atlantic: A comparative study of the Labrador Sea-Labrador/Newfoundland shelves and Barents/Norwegian/Greenland seas and shelves, *Progress in Oceanography*, *114*, 26 – 45, doi: 10.1016/j.pocean.2013.05.003.

Hátún, H., C. Eriksen, and P. Rhines (2007), Buoyant Eddies Entering the Labrador Sea Observed with Gliders and Altimetry, *J. Phys. Oceanography*, *37*, doi: 10.1175/2007JPO3567.1.

Herrford, J., P. Brandt, and W. Zenk (2017), Property changes of deep and bottom waters in the Western Tropical Atlantic, *Deep Sea Research Part I: Oceanographic Research Papers*, *124*, 103 – 125, doi: https://doi.org/10.1016/j.dsr.2017.04.007.

Hirschi, J., J. Baehr, J. Marotzke, J. Stark, S. Cunningham, and J.-O. Beismann (2003), A monitoring design for the Atlantic meridional overturning circulation, *Geophysical Research Letters*, *30*(7), doi: 10.1029/2002GL016776.

Houston, M. H., and J. M. Paros (1998), High accuracy pressure instrumentation for underwater applications, in *UT 1998 - Proceedings of the 1998 International Symposium on Underwater Technology*, pp. 307–311, IEEE, doi: 10.1109/UT.1998.670113.

Hurrell, J. W., Y. Kushnir, G. Ottersen, and M. Visbeck (2013), An Overview of the North Atlantic Oscillation, in *The North Atlantic Oscillation: Climatic Significance and Environmental Impact*, pp. 1–35, American Geophysical Union, doi: 10.1029/134GM01.

Ilyina, T., K. D. Six, J. Segschneider, E. Maier-Reimer, H. Li, and I. Núñez-Riboni (2013), Global ocean biogeochemistry model HAMOCC: Model architecture and performance as component of the MPI-Earth system model in different CMIP5 experimental realizations, *Journal of Advances in Modeling Earth Systems*, *5*, 287–315, doi: 10.1029/2012MS000178.

IOCCP-ICPO (2010), The GO-SHIP Repeat Hydrography Manual: A Collection of Expert Reports and Guidelines. IOCCP Report Number 14, ICPO Publication Series Number 134., *IOCCP Rep*, *14*.

Ito, T., M. J. Follows, and E. A. Boyle (2004), Is AOU a good measure of respiration in the oceans?, *Geophysical Research Letters*, *31*, doi: 10.1029/2004GL020900.

Ivchenko, V. O., S. D. Danilov, D. V. Sidorenko, J. Schröter, M. Wenzel, and D. L. Aleynik (2007), Comparing the steric height in the Northern Atlantic with satellite altimetry, *Ocean Science*, *3*(4), 485–490, doi: 10.5194/os-3-485-2007.

Jackson, L. C., K. A. Peterson, C. D. Roberts, and R. A. Wood (2016), Recent slowing of Atlantic overturning circulation as a recovery from earlier strengthening, *Nature Geoscience*, *9*(7), 518–522, doi: 10.1038/ngeo2715.

Johns, W. E., M. O. Baringer, L. M. Beal, S. A. Cunningham, T. Kanzow, H. L. Bryden, J. J. M. Hirschi, J. Marotzke, C. S. Meinen, B. Shaw, and R. Curry (2011), Continuous, Array-Based Estimates of Atlantic Ocean Heat Transport at 26.5°N, *Journal of Climate*, *24*(10), 2429–2449, doi: 10.1175/2010JCLI3997.1.

Johnson, G. C. (2008), Quantifying Antarctic Bottom Water and North Atlantic Deep Water volumes, *Journal of Geophysical Research: Oceans*, *113*(C5), doi: 10.1029/2007JC004477.

Johnson, G. C., J. M. Lyman, and S. G. Purkey (2015), Informing deep argo array design using argo and full-depth hydrographic section data, *Journal of Atmospheric and Oceanic Technology*, *32*(11), 2187–2198, doi: 10.1175/JTECH-D-15-0139.1.

Johnson, H. L., P. Cessi, D. P. Marshall, F. Schloesser, and M. A. Spall (2019), Recent Contributions of Theory to Our Understanding of the Atlantic Meridional Overturning Circulation, *Journal of Geophysical Research: Oceans*, *124*(8), 5376–5399, doi: 10.1029/2019JC015330.

Kalnay, E., M. Kanamitsu, R. Kistler, W. Collins, D. Deaven, L. Gandin, M. Iredell, S. Saha, G. White, J. Woollen, Y. Zhu, A. Leetmaa, R. Reynolds, M. Chelliah, W. Ebisuzaki, W. Higgins, J. Janowiak, K. C. Mo, C. Ropelewski, J. Wang, R. Jenne, and D. Joseph (1996), The NCEP/NCAR 40-Year Reanalysis Project, *Bulletin of the American Meteorological Society*, *77*, 437–471, doi: 10.1175/1520-0477(1996)077¡0437:TNYRP¿2.0.CO;2.

Kanzow, T. (2004), Monitoring the integrated deep meridional flow in the tropical North Atlantic, Ph.D. thesis, Christian-Albrechts-Universität zu Kiel.

Kanzow, T., U. Send, W. Zenk, A. D. Chave, and M. Rhein (2006), Monitoring the integrated deep meridional flow in the tropical North Atlantic: Long-term performance of a geostrophic array, *Deep-Sea Research Part I: Oceanographic Research Papers*, *53*(3), 528–546, doi: 10.1016/j.dsr.2005.12.007.

Kanzow, T., S. A. Cunningham, D. Rayner, J. J.-M. Hirschi, W. E. Johns, M. O. Baringer, H. L. Bryden, L. M. Beal, C. S. Meinen, and J. Marotzke (2007), Observed Flow Compensation Associated with the MOC at 26.5°N in the Atlantic, *Science*, *317*(5840), 938–941, doi: 10.1126/science.1141293.

Kanzow, T., U. Send, and M. McCartney (2008), On the variability of the deep meridional transports in the tropical North Atlantic, *Deep Sea Research Part I: Oceanographic Research Papers*, *55*(12), 1601 – 1623, doi: https://doi.org/10.1016/j.dsr.2008.07.011.

Kawase, M. (1987), Establishment of Deep Ocean Circulation Driven by Deep-Water Production, *Journal of Physical Oceanography*, *17*(12), 2294–2317, doi: 10.1175/1520-0485(1987)017¡2294:EODOCD¿2.0.CO;2.

Keeling, R. F. (1993), On the role of large bubbles in air-sea gas exchange and supersaturation in the ocean, *Journal of Marine Research*, *51*, 237–271, doi: doi:10.1357/0022240933223800".

Keeling, R. F., A. Körtzinger, and N. Gruber (2010), Ocean Deoxygenation in a Warming World, *Annual Review of Marine Science*, *2*, 199–229, doi: 10.1146/annurev.marine.010908.163855.

Kihm, C., and A. Körtzinger (2010), Air-sea gas transfer velocity for oxygen derived from float data, *Journal of Geophysical Research: Oceans*, *115*, doi: 10.1029/2009JC006077.

Koelling, J., D. W. R. Wallace, U. Send, and J. Karstensen (2017), Intense oceanic uptake of oxygen during 20142015 winter convection in the Labrador Sea, *Geophysical Research Letters*, *44*(15), 7855–7864, doi: 10.1002/2017GL073933.

Koelling, J., U. Send, and M. Lankhorst (2020), Decadal strengthening of interior flow of North Atlantic Deep Water observed by GRACE satellites, *submitted to Journal of Geophysical Research: Oceans*.

Köhl, A., and D. Stammer (2008), Variability of the Meridional Overturning in the North Atlantic from the 50-Year GECCO State Estimation, *Journal of Physical Oceanography*, *38*, doi: 10.1175/2008JPO3775.1.

Körtzinger, A., J. I. Hedges, and P. D. Quay (2001), Redfield ratios revisited: Removing the biasing effect of anthropogenic CO2, *Limnology and Oceanography*, *46*, 964–970, doi: 10.4319/lo.2001.46.4.0964.

Körtzinger, A., J. Schimanski, U. Send, and D. W. R. Wallace (2004), The Ocean Takes a Deep Breath, *Science*, *306*, 1337–1337, doi: 10.1126/science.1102557.

Körtzinger, A., U. Send, D. W. R. Wallace, J. Karstensen, and M. DeGrandpre (2008), Seasonal cycle of O2 and pCO2 in the central Labrador Sea: Atmospheric, biological, and physical implications, *Global Biogeochemical Cycles*, *22*, doi: 10.1029/2007GB003029.

Landerer, F. W., D. N. Wiese, K. Bentel, C. Boening, and M. M. Watkins (2015), North Atlantic meridional overturning circulation variations from GRACE ocean bottom pressure anomalies, *Geophysical Research Letters*, *42*(19), 8114–8121, doi: 10.1002/2015GL065730.

Lazier, J. (1973), The renewal of Labrador sea water, *Deep Sea Research and Oceanographic Abstracts*, *20*, 341 – 353, doi: 10.1016/0011-7471(73)90058-2.

Le Bras, I. A., I. Yashayaev, and J. M. Toole (2017), Tracking Labrador Sea Water property signals along the Deep Western Boundary Current, *Journal of Geophysical Research: Oceans*, *122*(7), 5348–5366, doi: 10.1002/2017JC012921.

LeBel, D. A., W. M. Smethie, M. Rhein, D. Kieke, R. A. Fine, J. L. Bullister, D.-H. Min, W. Roether, R. F. Weiss, C. Andri, D. Smythe-Wright, and E. P. Jones (2008), The formation rate of North Atlantic Deep Water and Eighteen Degree Water calculated from CFC-11 inventories observed during WOCE, *Deep Sea Research Part I: Oceanographic Research Papers*, *55*(8), 891 – 910, doi: https://doi.org/10.1016/j.dsr.2008.03.009.

Legg, S., B. Briegleb, Y. Chang, E. P. Chassignet, G. Danabasoglu, T. Ezer, A. L. Gordon, S. Griffies, R. Hallberg, L. Jackson, W. Large, T. M. zgkmen, H. Peters, J. Price, U. Riemenschneider, W. Wu, X. Xu, and J. Yang (2009), Improving Oceanic Overflow Representation in Climate Models: The Gravity Current Entrainment Climate Process Team, *Bulletin of the American Meteorological Society*, *90*(5), 657–670, doi: 10.1175/2008BAMS2667.1.

Leith, C. E. (1973), The Standard Error of Time-Average Estimates of Climatic Means, *Journal of Applied Meteorology*, *12*(6), 1066–1069, doi: 10.1175/1520-0450(1973)012¡1066:tseota¿2.0.co;2.

Leuliette, E. W., and L. Miller (2009), Closing the sea level rise budget with altimetry, Argo, and Grace, *Geophysical Research Letters*, *36*(4), L04,608, doi: 10.1029/2008GL036010.

Levitus, S., J. I. Antonov, O. K. Baranova, T. P. Boyer, C. L. Coleman, H. E. Garcia, A. I. Grodsky, D. R. Johnson, R. A. Locarnini, A. V. Mishonov, J. R. Reagan, C. L. Sazama, D. Seidov, I. Smolyar, E. S. Yarosh, and M. M. Zweng (2013), The World Ocean Database, *Data Science Journal*, *12*, WDS229–WDS234, doi: 10.2481/dsj.WDS-041.

Lewis, E., D. Wallace, and L. Allison (1998), Program developed for CO_2 system calculations, doi: 10.2172/639712.

Li, M., J. Liu, Z. Wang, H. Wang, Z. Zhang, L. Zhang, and Q. Yang (2013), Assessment of sea surface wind from NWP reanalyses and satellites in the Southern Ocean, *Journal of Atmospheric and Oceanic Technology*, *30*, 1842–1853, doi: 10.1175/JTECH-D-12-00240.1.

Liang, J.-H., C. Deutsch, J. C. McWilliams, B. Baschek, P. P. Sullivan, and D. Chiba (2013), Parameterizing bubble-mediated air-sea gas exchange and its effect on ocean ventilation, *Global Biogeochemical Cycles*, *27*, 894–905, doi: 10.1002/gbc.20080.

Lilly, J., P. Rhines, F. Schott, K. Lavender, J. Lazier, U. Send, and E. D'Asaro (2003), Observations of the Labrador Sea eddy field, *Progress in Oceanography*, *59*, doi: 10.1016/j.pocean.2003.08.013.

Liss, P. S., and L. Merlivat (1986), Air-Sea Gas Exchange Rates: Introduction and Synthesis, in *The Role of Air-Sea Exchange in Geochemical Cycling*, edited by P. Buat-Ménard, pp. 113–127, Springer Netherlands, Dordrecht, doi: 10.1007/978-94-009-4738-2_5.

Lohmann, K., J. H. Jungclaus, D. Matei, J. Mignot, M. Menary, H. R. Langehaug, J. Ba, Y. Gao, O. H. Otterå, W. Park, and S. Lorenz (2014), The role of subpolar deep water formation and Nordic Seas overflows in simulated multidecadal variability of the Atlantic meridional overturning circulation, *Ocean Science*, *10*, doi: 10.5194/os-10-227-2014.

Lozier, M. S. (1997), Evidence for Large-Scale Eddy-Driven Gyres in the North Atlantic, *Science*, *277*(5324), 361–364, doi: 10.1126/science.277.5324.361.

Lozier, M. S. (2010), Deconstructing the conveyor belt, *Science*, *328*(5985), 1507–1511, doi: 10.1126/science.1189250.

Lozier, M. S., S. F. Gary, and A. S. Bower (2013), Simulated pathways of the overflow waters in the North Atlantic: Subpolar to subtropical export, *Deep Sea Research Part II: Topical Studies in Oceanography*, *85*, 147–153, doi: 10.1016/J.DSR2.2012.07.037.

Lozier, M. S., S. Bacon, A. S. Bower, S. A. Cunningham, M. Femke de Jong, L. de Steur, B. deYoung, J. Fischer, S. F. Gary, B. J. W. Greenan, P. Heimbach, N. P. Holliday, L. Houpert, M. E. Inall, W. E. Johns, H. L. Johnson, J. Karstensen, F. Li, X. Lin, N. Mackay, D. P. Marshall, H. Mercier, P. G. Myers, R. S. Pickart, H. R. Pillar, F. Straneo, V. Thierry, R. A. Weller, R. G. Williams, C. Wilson, J. Yang, J. Zhao, and J. D. Zika (2017), Overturning in the Subpolar North Atlantic Program: A New International Ocean Observing System, *Bulletin of the American Meteorological Society*, *98*(4), 737–752, doi: 10.1175/BAMS-D-16-0057.1.

Lozier, M. S., F. Li, S. Bacon, F. Bahr, A. S. Bower, S. A. Cunningham, M. F. de Jong, L. de Steur, B. deYoung, J. Fischer, S. F. Gary, B. J. W. Greenan, N. P. Holliday, A. Houk, L. Houpert, M. E. Inall, W. E. Johns, H. L. Johnson, C. Johnson, J. Karstensen, G. Koman, I. A. Le Bras, X. Lin, N. Mackay, D. P. Marshall, H. Mercier, M. Oltmanns, R. S. Pickart, A. L. Ramsey, D. Rayner, F. Straneo, V. Thierry, D. J. Torres, R. G. Williams, C. Wilson, J. Yang, I. Yashayaev, and J. Zhao (2019), A sea change in our view of overturning in the subpolar North Atlantic, *Science*, *363*(6426), 516–521, doi: 10.1126/science.aau6592.

Marotzke, J., and B. A. Klinger (2000), The Dynamics of Equatorially Asymmetric Thermohaline Circulations, *Journal of Physical Oceanography*, *30*(5), 955–970, doi: 10.1175/1520-0485(2000)030¡0955:TDOEAT¿2.0.CO;2.

Marshall, D. P., and H. L. Johnson (2013), Propagation of Meridional Circulation Anomalies along Western and Eastern Boundaries, *Journal of Physical Oceanography*, *43*(12), 2699–2717, doi: 10.1175/JPO-D-13-0134.1.

Marshall, J., and F. Schott (1999), Open-ocean convection: Observations, theory, and models, *Rev. Geophys.*, *37*, doi: 10.1029/98RG02739.

Martz, T. R., M. D. DeGrandpre, P. G. Strutton, W. R. McGillis, and W. M. Drennan (2009), Sea surface pCO2 and carbon export during the Labrador Sea spring-summer bloom: An in situ mass balance approach, *Journal of Geophysical Research: Oceans*, *114*, doi: 10.1029/2008JC005060.

Matsumoto, K. (2007), Radiocarbon-based circulation age of the world oceans, *Journal of Geophysical Research: Oceans*, *112*(C9), doi: 10.1029/2007JC004095.

Mazloff, M. R., and C. Boening (2016), Rapid variability of Antarctic Bottom Water transport into the Pacific Ocean inferred from GRACE, *Geophysical Research Letters*, *43*(8), 3822–3829, doi: 10.1002/2016GL068474.

McCarthy, G., D. Smeed, W. Johns, E. Frajka-Williams, B. Moat, D. Rayner, M. Baringer, C. Meinen, J. Collins, and H. Bryden (2015), Measuring the Atlantic Meridional Overturning Circulation at 26°N, *Progress in Oceanography*, *130*, 91–111, doi: 10.1016/J.POCEAN.2014.10.006.

McCarthy, G. D., M. B. Menary, J. V. Mecking, B. I. Moat, W. E. Johns, M. B. Andrews, D. Rayner, and D. A. Smeed (2017), The importance of deep, basinwide measurements in optimized Atlantic Meridional Overturning Circulation observing arrays, *Journal of Geophysical Research: Oceans*, *122*(3), 1808–1826, doi: 10.1002/2016JC012200.

McKinley, G. A., M. J. Follows, and J. Marshall (2000), Interannual variability of the air-sea flux of oxygen in the North Atlantic, *Geophysical Research Letters*, *27*, 2933–2936, doi: 10.1029/2000GL011492.

McKinley, G. A., M. J. Follows, J. M., and S.-M. Fan (2003), Interannual variability of air-sea O2 fluxes and the determination of CO2 sinks using atmospheric O2/N2, *Geophysical Research Letters*, *30*, doi: 10.1029/2002GL016044.

Meinen, C. S., M. O. Baringer, and R. F. Garcia (2010), Florida Current transport variability: An analysis of annual and longer-period signals, *Deep Sea Research Part I: Oceanographic Research Papers*, *57*(7), 835 – 846, doi: 10.1016/j.dsr.2010.04.001.

Mesinger, F., G. DiMego, E. Kalnay, K. Mitchell, P. C. Shafran, W. Ebisuzaki, D. Jović, J. Woollen, E. Rogers, E. H. Berbery, M. B. Ek, Y. Fan, R. Grumbine, W. Higgins, H. Li, Y. Lin, G. Manikin, D. Parrish, and W. Shi (2006), North American Regional Reanalysis, *Bulletin of the American Meteorological Society*, *87*(3), 343–360, doi: 10.1175/BAMS-87-3-343.

Molinari, R. L., R. A. Fine, W. D. Wilson, R. G. Curry, J. Abell, and M. S. McCartney (1998), The arrival of recently formed Labrador sea water in the Deep Western Boundary Current at 26.5°N, *Geophysical Research Letters*, *25*(13), 2249–2252, doi: 10.1029/98GL01853.

Moore, G. W. K., R. S. Pickart, and I. A. Renfrew (2008), Buoy observations from the windiest location in the world ocean, Cape Farewell, Greenland, *Geophysical Research Letters*, *35*(18), doi: 10.1029/2008GL034845.

Msadek, R., W. E. Johns, S. G. Yeager, G. Danabasoglu, T. L. Delworth, and A. Rosati (2013), The Atlantic Meridional Heat Transport at 26.5N and Its Relationship with the MOC in the RAPID Array and the GFDL and NCAR Coupled Models, *Journal of Climate*, *26*(12), 4335–4356, doi: 10.1175/JCLI-D-12-00081.1.

Muir, L. C., and A. V. Fedorov (2017), Evidence of the AMOC interdecadal mode related to westward propagation of temperature anomalies in CMIP5 models, *Climate Dynamics*, *48*(5-6), 1517–1535, doi: 10.1007/s00382-016-3157-9.

Nightingale, P. D., G. Malin, C. S. Law, A. J. Watson, P. S. Liss, M. I. Liddicoat, J. Boutin, and R. C. Upstill-Goddard (2000), In situ evaluation of air-sea gas exchange parameterizations using novel conservative and volatile tracers, *Global Biogeochemical Cycles*, *14*, 373–387, doi: 10.1029/1999GB900091.

Olsen, A., K. R. Brown, M. Chierici, T. Johannessen, and C. Neill (2008), Sea-surface CO_2 fugacity in the subpolar North Atlantic, *Biogeosciences*, *5*(2), 535–547, doi: 10.5194/bg-5-535-2008.

Oltmanns, M., J. Karstensen, and J. Fischer (2018), Increased risk of a shutdown of ocean convection posed by warm North Atlantic summers, *Nature Climate Change*, *8*(4), 300–304.

Ortega, P., J. Mignot, D. Swingedouw, F. Svellec, and E. Guilyardi (2015), Reconciling two alternative mechanisms behind bi-decadal variability in the North Atlantic, *Progress in Oceanography*, *137*, 237 – 249, doi: https://doi.org/10.1016/j.pocean.2015.06.009.

Peltier, W. (2009), Closure of the budget of global sea level rise over the GRACE era: the importance and magnitudes of the required corrections for global glacial isostatic adjustment, *Quaternary Science Reviews*, *28*(17), 1658 – 1674, doi: 10.1016/j.quascirev.2009.04.004.

Plant, J. N., K. S. Johnson, C. M. Sakamoto, H. W. Jannasch, L. J. Coletti, S. C. Riser, and D. D. Swift (2016), Net community production at Ocean Station Papa observed with nitrate and oxygen sensors on profiling floats, *Global Biogeochemical Cycles*, *30*, 859–879, doi: 10.1002/2015GB005349.

Purkey, S. G., and G. C. Johnson (2013), Antarctic bottom water warming and freshening: Contributions to sea level rise, ocean freshwater budgets, and global heat gain, *Journal of Climate*, *26*(16), 6105–6122, doi: 10.1175/JCLI-D-12-00834.1.

Purkey, S. G., G. C. Johnson, and D. P. Chambers (2014), Relative contributions of ocean mass and deep steric changes to sea level rise between 1993 and 2013, *Journal of Geophysical Research: Oceans*, *119*(11), 7509–7522, doi: 10.1002/2014JC010180.

Rahmstorf, S. (2002), Ocean circulation and climate during the past 120,000 years, *Nature*, *419*(6903), 207–214.

Redfield, A. C. (1934), On the proportions of organic derivatives in sea water and their relation to the composition of plankton, *James Johnstone memorial volume*, pp. 176–192.

Renfrew, I. A., G. N. Petersen, D. A. J. Sproson, G. W. K. Moore, H. Adiwidjaja, S. Zhang, and R. North (2009), A comparison of aircraft-based surface-layer observations over Denmark Strait and the Irminger Sea with meteorological analyses and QuikSCAT winds, *Quarterly Journal of the Royal Meteorological Society*, *135*(645), 2046–2066, doi: 10.1002/qj.444.

Rhein, M., M. Walter, C. Mertens, R. Steinfeldt, and D. Kieke (2004), The circulation of North Atlantic Deep Water at 16°N, 20002003, *Geophysical Research Letters*, *31*(14), doi: 10.1029/2004GL019993.

Rhein, M., D. Kieke, and R. Steinfeldt (2015), Advection of North Atlantic Deep Water from the Labrador Sea to the southern hemisphere, *Journal of Geophysical Research: Oceans*, *120*(4), 2471–2487, doi: 10.1002/2014JC010605.

Rhein, M., R. Steinfeldt, D. Kieke, I. Stendardo, and I. Yashayaev (2017), Ventilation variability of Labrador Sea Water and its impact on oxygen and anthropogenic carbon: a review, *Philosophical Transactions of the Royal Society A: Mathematical, Physical and Engineering Sciences*, *375*(2102), 20160,321, doi: 10.1098/rsta.2016.0321.

Sabine, C. L., R. A. Feely, N. Gruber, R. M. Key, K. Lee, J. L. Bullister, R. Wanninkhof, C. Wong, D. W. Wallace, B. Tilbrook, et al. (2004), The oceanic sink for anthropogenic CO2, *science*, *305*(5682), 367–371.

Sarafanov, A., A. Falina, H. Mercier, P. Lherminier, and A. Sokov (2009), Recent changes in the GreenlandScotland overflow-derived water transport inferred from hydrographic observations in the southern Irminger Sea, *Geophysical Research Letters*, *36*(13), doi: 10.1029/2009GL038385.

Save, H., S. Bettadpur, and B. D. Tapley (2016), High-resolution CSR GRACE RL05 mascons, *Journal of Geophysical Research: Solid Earth*, *121*(10), 7547–7569, doi: 10.1002/2016JB013007.

Schmidt, S., and U. Send (2007), Origin and Composition of Seasonal Labrador Sea Freshwater, *Journal of Physical Oceanography*, *37*(6), 1445–1454, doi: 10.1175/JPO3065.1.

Schmidtko, S., L. Stramma, and M. Visbeck (2017), Decline in global oceanic oxygen content during the past five decades, *Nature*, *542*(7641), 335–339, doi: 10.1038/nature21399.

Schmitz, W. J., and M. S. McCartney (1993), On the North Atlantic Circulation, *Reviews of Geophysics*, *31*(1), 29–49, doi: 10.1029/92RG02583.

Schulze Chretien, L. M., and E. Frajka-Williams (2018), Wind-driven transport of fresh shelf water into the upper 30m of the Labrador Sea, *Ocean Science*, *14*(5), 1247–1264.

Send, U., and J. Marshall (1995), Integral Effects of Deep Convection, *J. Phys. Oceanography*, *25*, doi: 10.1175/1520-0485(1995)025¡0855:IEODC¿2.0.CO;2.

Send, U., M. Lankhorst, and T. Kanzow (2011), Observation of decadal change in the Atlantic meridional overturning circulation using 10 years of continuous transport data, *Geophysical Research Letters*, *38*(24), doi: 10.1029/2011GL049801.

Send, U., G. Fowler, G. Siddall, B. Beanlands, M. Pittman, C. Waldmann, J. Karstensen, and R. Lampitt (2013), SeaCycler: A Moored Open-Ocean Profiling System for the Upper Ocean in Extended Self-Contained Deployments, *Journal of Atmospheric and Oceanic Technology*, *30*, 1555–1565, doi: 10.1175/JTECH-D-11-00168.1.

Sévellec, F., and A. V. Fedorov (2013), The Leading, Interdecadal Eigenmode of the Atlantic Meridional Overturning Circulation in a Realistic Ocean Model, *Journal of Climate*, *26*(7), 2160–2183, doi: 10.1175/JCLI-D-11-00023.1.

Sinha, B., D. Smeed, G. McCarthy, B. Moat, S. Josey, J.-M. Hirschi, E. Frajka-Williams, A. Blaker, D. Rayner, and G. Madec (2018), The accuracy of estimates of the overturning circulation from basin-wide mooring arrays, *Progress in Oceanography*, *160*, 101 – 123, doi: 10.1016/j.pocean.2017.12.001.

Smeed, D., B. Moat, D. Rayner, W. Johns, M. Baringer, D. Volkov, and E. Frajka-Williams (2019), Atlantic meridional overturning circulation observed by the RAPID-MOCHA-WBTS (RAPID-Meridional overturning circulation and heatflux array-Western boundary time series) array at 26N from 2004 to 2018, *British Oceanographic Data Centre - Natural Environment Research Council, UK*.

Smeed, D. A., G. D. McCarthy, S. A. Cunningham, E. Frajka-Williams, D. Rayner, W. E. Johns, C. S. Meinen, M. O. Baringer, B. I. Moat, A. Duchez, and H. L. Bryden (2014), Observed decline of the Atlantic meridional overturning circulation 2004-2012, *Ocean Science*, *10*(1), 29–38, doi: 10.5194/os-10-29-2014.

Smeed, D. A., S. A. Josey, C. Beaulieu, W. E. Johns, B. I. Moat, E. Frajka-Williams, D. Rayner, C. S. Meinen, M. O. Baringer, H. L. Bryden, and G. D. McCarthy (2018), The North Atlantic Ocean Is in a State of Reduced Overturning, *Geophysical Research Letters*, *45*(3), 1527–1533, doi: 10.1002/2017GL076350.

Smith, G. C., F. Roy, P. Mann, F. Dupont, B. Brasnett, J.-F. Lemieux, S. Laroche, and S. Bélair (2014), A new atmospheric dataset for forcing ice-ocean models: Evaluation of reforecasts using the Canadian global deterministic prediction system, *Quarterly Journal of the Royal Meteorological Society*, *140*, 881–894, doi: 10.1002/qj.2194.

Smith, J. N., W. M. Smethie, I. Yashayev, R. Curry, and K. Azetsu-Scott (2016), Time series measurements of transient tracers and tracer-derived transport in the Deep Western Boundary Current between the Labrador Sea and the subtropical Atlantic Ocean at Line W, *Journal of Geophysical Research: Oceans*, *121*(11), 8115–8138, doi: 10.1002/2016JC011759.

Smith, W. H. F., and D. T. Sandwell (1997), Global Sea Floor Topography from Satellite Altimetry and Ship Depth Soundings, *Science*, *277*(5334), 1956–1962, doi: 10.1126/science.277.5334.1956.

Spall, M. A. (1996a), Dynamics of the Gulf Stream/Deep Western Boundary Current Crossover. Part I: Entrainment and Recirculation, *Journal of Physical Oceanography*, *26*(10), 2152–2168, doi: 10.1175/1520-0485(1996)026¡2152:DOTGSW¿2.0.CO;2.

Spall, M. A. (1996b), Dynamics of the Gulf Stream/Deep Western Boundary Current Crossover. Part II: Low-Frequency Internal Oscillations, *Journal of Physical Oceanography*, *26*(10), 2169–2182, doi: 10.1175/1520-0485(1996)026¡2169:DOTGSW¿2.0.CO;2.

Srokosz, M. A., and H. L. Bryden (2015), Observing the Atlantic Meridional Overturning Circulation yields a decade of inevitable surprises, *Science*, *348*(6241), 1255,575–1255,575, doi: 10.1126/science.1255575.

Stanley, R. H. R., W. J. Jenkins, D. E. Lott, and S. C. Doney (2009), Noble gas constraints on air-sea gas exchange and bubble fluxes, *Journal of Geophysical Research: Oceans*, *114*, doi: 10.1029/2009JC005396.

Steinfeldt, R., M. Rhein, J. L. Bullister, and T. Tanhua (2009), Inventory changes in anthropogenic carbon from 19972003 in the Atlantic Ocean between 20°S and 65°N, *Global Biogeochemical Cycles*, *23*(3), doi: 10.1029/2008GB003311.

Stendardo, I., and N. Gruber (2012), Oxygen trends over five decades in the North Atlantic, *Journal of Geophysical Research: Oceans*, *117*, doi: 10.1029/2012JC007909.

Stommel, H., and A. B. Arons (1959), On the abyssal circulation of the world ocean-I. Stationary planetary flow patterns on a sphere, *Deep Sea Research (1953)*, *6*(C), 140–154, doi: 10.1016/0146-6313(59)90065-6.

Straneo, F. (2006), On the Connection between Dense Water Formation, Overturning, and Poleward Heat Transport in a Convective Basin, *J. Phys. Oceanography*, *36*, doi: 10.1175/JPO2932.1.

Sutton, R. T., and D. L. R. Hodson (2005), Atlantic Ocean Forcing of North American and European Summer Climate, *309*(5731), 115–118, doi: 10.1126/science.1109496.

Sweeney, C., E. Gloor, A. R. Jacobson, R. M. Key, G. McKinley, J. L. Sarmiento, and R. Wanninkhof (2007), Constraining global air-sea gas exchange for CO2 with recent bomb 14C measurements, *Global Biogeochemical Cycles*, *21*, doi: 10.1029/2006GB002784.

Takahashi, T., S. C. Sutherland, W. R., C. Sweeney, R. A. Feely, D. W. Chipman, B. Hales, G. Friederich, F. Chavez, C. Sabine, A. Watson, B. D. C. E., U. Schuster, N. Metzl, H. Yoshikawa-Inoue, M. Ishii, T. Midorikawa, Y. Nojiri, A. Körtzinger, T. Steinhoff, M. Hoppema, J. Olafsson, T. S. Arnarson, B. Tilbrook, T. Johannessen, A. Olsen, R. Bellerby, C. S. Wong, B. Delille, N. Bates, and H. J. de Baar (2009), Climatological mean and decadal change in surface ocean pCO2, and net sea-air CO2 flux over the global oceans, *Deep Sea Research Part II: Topical Studies in Oceanography*, *56*, 554 – 577, doi: 10.1016/j.dsr2.2008.12.009.

Takeshita, Y., T. R. Martz, K. S. Johnson, J. N. Plant, D. Gilbert, S. C. Riser, C. Neill, and B. Tilbrook (2013), A climatology-based quality control procedure for profiling float oxygen data, *Journal of Geophysical Research: Oceans*, *118*, 5640–5650, doi: 10.1002/jgrc.20399.

Talley, L., and M. McCartney (1982), Distribution and Circulation of Labrador Sea Water, *J. Phys. Oceanography*, *1*, doi: 10.1175/1520-0485(1982)012¡1189:DACOLS¿2.0.CO;2.

Talley, L. D., G. L. Pickard, W. J. Emery, and J. H. Swift (2011), Dynamical Processes for Descriptive Ocean Circulation, *Descriptive Physical Oceanography*, pp. 187–221, doi: 10.1016/b978-0-7506-4552-2.10007-1.

Tamsitt, V., H. F. Drake, A. K. Morrison, L. D. Talley, C. O. Dufour, A. R. Gray, S. M. Griffies, M. R. Mazloff, J. L. Sarmiento, J. Wang, et al. (2017), Spiraling pathways of global deep waters to the surface of the Southern Ocean, *Nature communications*, *8*(1), 1–10.

Tapley, B. D., S. Bettadpur, M. Watkins, and C. Reigber (2004), The gravity recovery and climate experiment: Mission overview and early results, *Geophysical Research Letters*, *31*(9), n/a–n/a, doi: 10.1029/2004GL019920.

Taylor, K. E., R. J. Stouffer, and G. A. Meehl (2012), An Overview of CMIP5 and the experiment design, *Bulletin of the American Meteorological Society*, *93*, 485–498, doi: 10.1175/BAMS-D-11-00094.1.

Te Raa, L. A., and H. A. Dijkstra (2002), Instability of the thermohaline ocean circulation on interdecadal timescales, *Journal of Physical Oceanography*, *32*(1), 138–160.

Tengberg, A., J. Hovdenes, H. J. Andersson, O. Brocandel, R. Diaz, D. Hebert, T. Arnerich, C. Huber, A. Körtzinger, A. Khripounoff, F. Rey, C. Rönning, J. Schimanski, S. Sommer, and A. Stangelmayer (2006), Evaluation of a lifetime-based optode to measure oxygen in aquatic systems, *Limnology and Oceanography: Methods*, *4*, 7–17, doi: 10.4319/lom.2006.4.7.

Thompson, P. R., M. A. Merrifield, E. Leuliette, W. Sweet, D. P. Chambers, B. D. Hamlington, S. Jevrejeva, J. J. Marra, G. T. Mitchum, R. S. Nerem, and M. J. Widlansky (2018), Sea

level variability and change, in *State of the Climate in 2017*, vol. 99, pp. S84–S86, doi: 10.1175/2018BAMSStateoftheClimate.1.

Thorpe, R. B., J. M. Gregory, T. C. Johns, R. A. Wood, and J. F. B. Mitchell (2001), Mechanisms Determining the Atlantic Thermohaline Circulation Response to Greenhouse Gas Forcing in a Non-Flux-Adjusted Coupled Climate Model, *Journal of Climate*, *14*(14), 3102–3116, doi: 10.1175/1520-0442(2001)014¡3102:MDTATC¿2.0.CO;2.

Thorpe, S. A. (1982), On the Clouds of Bubbles Formed by Breaking Wind-Waves in Deep Water, and their Role in Air-Sea Gas Transfer, *Philosophical Transactions of the Royal Society of London A: Mathematical, Physical and Engineering Sciences*, *304*, 155–210, doi: 10.1098/rsta.1982.0011.

Tjiputra, J. F., K. Assmann, M. Bentsen, I. Bethke, O. H. Otterå, C. Sturm, and C. Heinze (2010), Bergen Earth system model (BCM-C): model description and regional climate-carbon cycle feedbacks assessment, *Geoscientific Model Development*, *3*, 123–141, doi: 10.5194/gmd-3-123-2010.

Toole, J. M., M. Andres, I. A. Le Bras, T. M. Joyce, and M. S. McCartney (2017), Moored observations of the Deep Western Boundary Current in the NW Atlantic: 2004-2014, *Journal of Geophysical Research: Oceans*, *122*(9), 7488–7505, doi: 10.1002/2017jc012984.

Uchida, H., T. Kawano, I. Kaneko, and M. Fukasawa (2008), In Situ Calibration of Optode-Based Oxygen Sensors, *Journal of Atmospheric and Oceanic Technology*, *25*, 2271–2281, doi: 10.1175/2008JTECHO549.1.

Vagle, S., C. McNeil, and N. Steiner (2010), Upper ocean bubble measurements from the NE Pacific and estimates of their role in air-sea gas transfer of the weakly soluble gases nitrogen and oxygen, *Journal of Geophysical Research: Oceans*, *115*, doi: 10.1029/2009JC005990.

van Aken, H. M., and M. F. de Jong (2012), Hydrographic variability of Denmark Strait Overflow Water near Cape Farewell with multi-decadal to weekly time scales, *Deep Sea Research Part I: Oceanographic Research Papers*, *66*, 41 – 50, doi: https://doi.org/10.1016/j.dsr.2012.04.004.

Van Heuven, S., D. Pierrot, J. Rae, E. Lewis, and D. Wallace (2011), MATLAB program developed for CO2 system calculations, *ORNL/CDIAC-105b. Carbon Dioxide Information Analysis Center, Oak Ridge National Laboratory, US Department of Energy, Oak Ridge, Tennessee*, *530*.

van Sebille, E., M. O. Baringer, W. E. Johns, C. S. Meinen, L. M. Beal, M. F. de Jong, and H. M. van Aken (2011), Propagation pathways of classical Labrador Sea water from its source region to 26N, *Journal of Geophysical Research: Oceans*, *116*(C12), doi: 10.1029/2011JC007171.

Vianna, M. L., and V. V. Menezes (2013), Bidecadal sea level modes in the North and South Atlantic Oceans, *Geophysical Research Letters*, *40*(22), 5926–5931.

Wahr, J., R. S. Nerem, and S. V. Bettadpur (2015), The pole tide and its effect on GRACE time-variable gravity measurements: Implications for estimates of surface mass variations, *Journal of Geophysical Research: Solid Earth*, *120*(6), 4597–4615, doi: 10.1002/2015JB011986.

Wallace, D. W. R., and C. D. Wirick (1992), Large air-sea gas fluxes associated with breaking waves, *Nature*, *356*, 694–696, doi: 10.1038/356694a0.

Wang, H., S. A. Legg, and R. W. Hallberg (2015), Representations of the Nordic Seas overflows and their large scale climate impact in coupled models, *Ocean Modelling*, *86*, 76 – 92, doi: 10.1016/j.ocemod.2014.12.005.

Wanninkhof, R. (1992), Relationship between wind speed and gas exchange over the ocean, *Journal of Geophysical Research: Oceans*, *97*, 7373–7382, doi: 10.1029/92JC00188.

Wanninkhof, R. (2014), Relationship between wind speed and gas exchange over the ocean revisited, *Limnology and Oceanography: Methods*, *12*, 351–362, doi: 10.4319/lom.2014.12.351.

Wanninkhof, R., and W. R. McGillis (1999), A cubic relationship between air-sea CO2 exchange and wind speed, *Geophysical Research Letters*, *26*, 1889–1892, doi: 10.1029/1999GL900363.

Wanninkhof, R., W. E. Asher, D. T. Ho, C. Sweeney, and W. R. McGillis (2009), Advances in Quantifying Air-Sea Gas Exchange and Environmental Forcing, *Annual Review of Marine Science*, *1*, 213–244, doi: 10.1146/annurev.marine.010908.163742.

Watkins, M. M., D. N. Wiese, D.-N. Yuan, C. Boening, and F. W. Landerer (2015), Improved methods for observing Earth's time variable mass distribution with GRACE using spherical cap mascons, *Journal of Geophysical Research: Solid Earth*, *120*(4), 2648–2671, doi: 10.1002/2014JB011547.

Watts, D. R., and H. Kontoyiannis (1990), Deep-Ocean Bottom Pressure Measurement: Drift Removal and Performance, *Journal of Atmospheric and Oceanic Technology*, *7*(2), 296–306, doi: 10.1175/1520-0426(1990)007¡0296:dobpmd¿2.0.co;2.

Weaver, A. J., M. Eby, E. C. Wiebe, C. M. Bitz, P. B. Duffy, T. L. Ewen, A. F. Fanning, M. M. Holland, A. MacFadyen, H. D. Matthews, K. J. Meissner, O. Saenko, A. Schmittner, H. Wang, and M. Yoshimori (2001), The UVic earth system climate model: Model description, climatology, and applications to past, present and future climates, *Atmosphere-Ocean*, *39*, 361–428, doi: 10.1080/07055900.2001.9649686.

Wen, N., C. Frankignoul, and G. Gastineau (2016), Active AMOC–NAO coupling in the IPSL-CM5A-MR climate model, *Climate dynamics*, *47*(7-8), 2105–2119.

Williams, J., C. W. Hughes, and M. E. Tamisiea (2015), Detecting trends in bottom pressure measured using a tall mooring and altimetry, *Journal of Geophysical Research C: Oceans*, *120*(7), 5216–5232, doi: 10.1002/2015JC010955.

Willis, J. K. (2010), Can in situ floats and satellite altimeters detect long-term changes in Atlantic Ocean overturning?, *Geophysical Research Letters*, *37*(6), doi: 10.1029/2010GL042372.

Wolf, M. K., R. C. Hamme, D. Gilbert, I. Yashayaev, and V. Thierry (2018), Oxygen Saturation Surrounding Deep Water Formation Events in the Labrador Sea From Argo-O2 Data, *Global Biogeochemical Cycles*, *32*(4), 635–653, doi: 10.1002/2017GB005829.

Woolf, D. K. (1997), Bubbles and their role in gas exchange, in *The Sea Surface and Global Change:*, edited by P. S. Liss and R. A. Duce, pp. 173–206, Cambridge University Press, Cambridge, doi: 10.1017/CBO9780511525025.007.

Woolf, D. K., and S. A. Thorpe (1991), Bubbles and the air-sea exchange of gases in near-saturation conditions, *Journal of Marine Research*, *49*, 435–466, doi: doi:10.1357/002224091784995765.

Worthington, E. L., E. Frajka-Williams, and G. D. McCarthy (2019), Estimating the Deep Overturning Transport Variability at 26N Using Bottom Pressure Recorders, *Journal of Geophysical Research: Oceans*, *124*(1), 335–348, doi: 10.1029/2018JC014221.

Xu, X., E. P. Chassignet, W. E. Johns, W. J. Schmitz Jr, and E. J. Metzger (2014), Intraseasonal to interannual variability of the Atlantic meridional overturning circulation from eddy-resolving simulations and observations, *Journal of Geophysical Research: Oceans*, *119*(8), 5140–5159, doi: 10.1002/2014JC009994.

Xu, X., P. B. Rhines, E. P. Chassignet, and W. J. Schmitz (2015), Spreading of Denmark Strait Overflow Water in the Western Subpolar North Atlantic: Insights from Eddy-Resolving Simulations with a Passive Tracer, *Journal of Physical Oceanography*, *45*(12), 2913–2932, doi: 10.1175/jpo-d-14-0179.1.

Yang, J. (2015), Local and remote wind stress forcing of the seasonal variability of the Atlantic Meridional Overturning Circulation (AMOC) transport at 26.5°N, *Journal of Geophysical Research: Oceans*, *120*(4), 2488–2503, doi: 10.1002/2014JC010317.

Yashayaev, I. (2007), Hydrographic changes in the Labrador Sea, 1960-2005, *Progress in Oceanography*, *75*, doi: 10.1016/j.pocean.2007.04.015.

Yashayaev, I., and J. Loder (2009), Enhanced production of Labrador Sea Water in 2008, *Geophys. Res. Letters*, *36*, doi: 10.1029/2008GL036162.

Yashayaev, I., and J. W. Loder (2016), Recurrent replenishment of Labrador Sea Water and associated decadal-scale variability, *Journal of Geophysical Research: Oceans*, *121*(11), 8095–8114, doi: 10.1002/2016JC012046.

Yashayaev, I., and J. W. Loder (2017), Further intensification of deep convection in the Labrador Sea in 2016, *Geophysical Research Letters*, *44*(3), 1429–1438, doi: 10.1002/2016GL071668.

Zantopp, R., J. Fischer, M. Visbeck, and J. Karstensen (2017), From interannual to decadal: 17 years of boundary current transports at the exit of the Labrador Sea, *Journal of Geophysical Research: Oceans*, *122*(3), 1724–1748, doi: 10.1002/2016JC012271.

Zhang, R. (2010), Latitudinal dependence of Atlantic meridional overturning circulation (AMOC) variations, *Geophysical Research Letters*, *37*(16), doi: 10.1029/2010GL044474.

Zhang, R., T. L. Delworth, A. Rosati, W. G. Anderson, K. W. Dixon, H.-C. Lee, and F. Zeng (2011), Sensitivity of the North Atlantic Ocean Circulation to an abrupt change in the Nordic Sea overflow in a high resolution global coupled climate model, *Journal of Geophysical Research: Oceans*, *116*(C12), doi: 10.1029/2011JC007240.